1-1-2019

Design and Analysis of High-Frequency Quartz Crystal Microbalance Sensor Array with Concentric Electrodes and Dual Inverted Mesa Structure for Multiple Gas Detection

Aashish Joseph
University of Windsor

Follow this and additional works at: https://scholar.uwindsor.ca/etd

Design and Analysis of High-Frequency Quartz Crystal Microbalance Sensor Array with Concentric Electrodes and Dual Inverted Mesa Structure for Multiple Gas Detection

by

Aashish Joseph

A Thesis

Submitted to the Faculty of Graduate Studies

through the Department of Electrical and Computer Engineering

in Partial Fulfillment of the Requirements for

the Degree of Master of Applied Science

at the University of Windsor

Windsor, Ontario, Canada

Design and Analysis of High-Frequency Quartz Crystal Microbalance Sensor Array with Concentric Electrodes and Dual Inverted Mesa Structure for Multiple Gas Detection

by

Aashish Joseph

APPROVED BY:

_____

N. V. Engelen

Department of Civil and Environmental Engineering

_____

B. Shahrrava

Department of Electrical and Computer Engineering

_____

A. Emadi, Advisor

Department of Electrical and Computer Engineering

November 29, 2019

DECLARATION OF CO-AUTHORSHIP / PREVIOUS PUBLICATIONS

I hereby declare that this thesis incorporates material that is result of joint research, as follows:

Chapter 2 of the thesis includes a paper published in MDPI Journal of Sensors. This paper was co-authored with Haleh Nazemi, Dr. Jaewoo Park and Dr. Arezoo Emadi. Chapter 6 of the thesis includes a paper presented in IEEE Sensors 2019 Conference. This paper was co-authored with Dr. Arezoo Emadi. In all cases, only primary contributions of the author towards these publications are included in this thesis. The contribution of co-authors was primarily through the provision of assistance in manuscript preparation and refinement of ideas.

I am aware of the University of Windsor Senate Policy on Authorship and I certify that I have properly acknowledged the contribution of other researchers to my thesis, and have obtained written permission from each of the co-authors to include the above materials in my thesis.

I certify that, with the above qualification, this thesis, and the research to which it refers, is the product of my own work.

This thesis includes two original papers that have been previously published/submitted for publication in peer reviewed IEEE International conference and MDPI Journal of sensors, as follows:

Thesis Chapter	Publication title/full citation	Publication Status
Chapter 2	H. Nazemi, **A. Joseph**, J. Park, and A. Emadi, "Advanced Micro- and Nano-Gas Sensor Technology: A Review," Journal of Sensors, vol. 19, 1285, March 2019.	*Published*

Chapter 6	**A. Joseph** and A. Emadi, "Design and Optimization of a Multichannel Quartz Crystal Microbalance Sensor Array for Multiple Target Gas Detection," IEEE Sensors Conference, Montreal, Canada, October 2019.	*Published*

I certify that I have obtained a written permission from the copyright owners to include the above published materials in my thesis. I certify that the above material describes work completed during my registration as a graduate student at the University of Windsor.

I declare that, to the best of my knowledge, my thesis does not infringe upon anyone's copyright nor violate any proprietary rights and that any ideas, techniques, quotations, or any other material from the work of other people included in my thesis, published or otherwise, are fully acknowledged in accordance with the standard referencing practices. Furthermore, to the extent that I have included copyrighted material that surpasses the bounds of fair dealing within the meaning of the Canada Copyright Act, I certify that I have obtained a written permission from the copyright owners to include such materials in my thesis.

I declare that this is a true copy of my thesis, including any final revisions, as approved by my thesis committee and the Graduate Studies office, and that this thesis has not been submitted for a higher degree to any other University or Institution.

ABSTRACT

Lung Cancer is one of the most deadly diseases which claim millions of lives all around the world every year. One of the major reasons that make the treatment process of lung cancer hard is that the patients are diagnosed only during the later stages. Lung cancer patients exhales volatile organic compounds in their breath in low concentration even during the early stages of the disease. There are many gas sensors available to detect these volatiles. However, there are certain disadvantages which make most of the conventional gas sensors unsuitable for early detection. Quartz crystal microbalance (QCM) is one of the promising candidates for volatile organic compounds detection. This thesis describes the design and analysis of the high-frequency quartz crystal microbalance sensor array with a novel concentric electrode and dual inverted mesa structure. Conventional QCM sensors are limited with circular electrodes and single channel design which limits the sensing ability. The proposed QCM sensor array has advantages of a uniform displacement profile with the concentric electrodes and multiple channels on a high frequency monolithic quartz substrate without interference with the dual inverted mesa design. This high frequency multiple channels make the multiple gas detection feasible. Therefore, in this thesis the critical design parameters of this proposed design are analyzed and optimized through a comprehensive finite element analysis in COMSOL Multiphysics and analytical modelling. In addition, the interference between multiple QCM channels has been further eliminated. Furthermore, the fabrication procedure for the proposed high frequency QCM gas sensor array has been proposed and analyzed.

DEDICATION

I dedicate this thesis to all the families who've lost their loved ones to Cancer.

ACKNOWLEDGEMENTS

I would to like to take this opportunity to thank my supervisor Dr. Arezoo Emadi, for her guidance, encouragement and support throughout my thesis work. I am deeply grateful for her valuable time, lectures, weekly meetings and the technical support during my research. Dr. Arezoo Emadi, has always been my source of inspiration for leadership, dedication, perfection and hard work during the research. It is an honour to work under her supervision.

I am very grateful to the thesis committee members, Dr. Behnam Shahrrava and Dr. Niel Van Engelen, for their invaluable support, guidance and providing their precious time and efforts in reviewing my thesis and providing valuable suggestions.

Special thanks to all the e-Minds lab team members who have shared their knowledge and supported me during this research.

Last but not least, a heartfelt thanks to my lovely parents, family and friends who have supported me with their unconditional love in this wonderful journey.

TABLE OF CONTENTS

LIST OF TABLES

LIST OF FIGURES

xviii

LIST OF ABBREVIATIONS/SYMBOLS

Abbreviation	Explanation
VOC	Volatile Organic Compounds
IDE	Interdigitated Electrode
MOS	Metal Oxide Semiconductor
CNT	Carbon Nanotube
QCM	Quartz Crystal Microbalance
SAW	Surface Acoustic Wave
TSM	Thickness Shear Mode
c2c	Centre to Centre Distance
VT	Vibrating Layer Thickness
NVT	Non Vibrating Layer Thickness
RQ	Radius of Quartz
RE	Radius of Electrode
RW	Ring Width
RD	Dot Radius

CHAPTER 1

INTRODUCTION

1.1 Motivation

Cancer is considered to be the second leading cause of death in the world, next to heart disease [1]. It is defined as the spontaneous mutation in the single human body cells to undergo multiple cell division which results in the formation of tumor [2]. This mutation might be caused due to the environmental induced long or short term exposure to cancer causing agents or genetic disorders [3]. There are more than hundred types of cancer present which are characterized by the abnormal growth of the cells in the various parts of the human anatomical system. Out of these several types of cancer, lung cancer is one of the most common cancer with the highest number of cases of over 2 million patients, which accounts for about 12.3% of the total cancer cases diagnosed in the year 2018 [4].

Lung cancer accounts for about 1.76 million death in 2018, which is the highest mortality rate in the cancer related death [5]. This can be due to the late diagnosis of lung cancer i.e. stage IV - cancerous cells have reached an abnormal growth and spread across other organs in the human body [6]. According to the world health organization (WHO), lung cancer patients diagnosed at the later stages are extremely hard to treat for the oncologist as the cancerous cells fail to respond to the chemotherapy treatment at later stages [7]. This late diagnosis of lung cancer limits the probability of curing the disease and extending the life expectancy of the patients. If lung cancer is detected at an early stage, there is a higher probability of survival, less expensive treatment and an increased care for the patients can be provided [8].

Early diagnosis of lung cancer is considered to be onerous and complicated as the lung cancer patient at the early stages shows no symptoms or very less symptoms [9]. Conventional medical check-up such as chest X-ray does not recognise the lung cancer at the initial stages while the highly advanced diagnosis techniques such as the computer tomography (CT) [10], magnetic resonance imaging (MRI) [10], positron emission tomography (PET) [10] scans are quite expensive and other medical techniques such as sputum cytology [11] and biopsy are prescribed by the doctors only after the symptoms shown during later stages of lung cancer.

During the early stages, the lung cancer patients exhales traceable amount of volatile organic compounds (VOCs) in their breath in the range of 10 – 200 ppm whereas a person without lung cancer has only 10 - 500 ppb range [12-14]. An alternative diagnostic tool is proposed to effectively detect these small concentrations of VOCs in the breath of the lung cancer patient. These proposed highly sensitive gas sensor arrays, which are comparatively cheaper and faster than the conventional diagnosis methods, can offer a higher probability of curing the lung cancer disease in a wide range scale [15-18]. In short, this volatile - detecting sensor should as affordable as a stethoscope and effective as a CT scan so that even a general family doctor could use this gas sensor to detect early signs of lung cancer in the patients.

1.2 Thesis Contribution

This research focuses on the design and development of quartz crystal microbalance gas sensor array to analyze its critical design parameters and improve the overall mass sensitivity of the device as well as to eliminate the interference between multiple QCM channels with a novel electrode design and an array configuration.

In this thesis, several gas sensors are studied and analyzed for their capability in the volatiles detection with necessary qualities such as the high sensitivity, selectivity, reversibility, multiple target detection, low cost, ease of fabrication and smaller size. From this baseline study, each sensor showcased their own advantages and disadvantages, out of which the quartz crystal microbalance gas sensor is selected due to its simple structure, which makes the fabrication process less complicated and less expensive than the other gas sensors without compromising its performance in terms of sensitivity and selectivity. This sensor also exhibits properties such as ability to detect multiple gas targets in an array form and stability at higher temperature, which makes it a suitable candidate for detecting the volatile organic compounds.

Accordingly, the principle of operation of the quartz crystal microbalance sensor is studied and analyzed to investigate its potential for the necessary qualities. Following this, the mass and frequency change relationship in the sensor are examined which forms the basic working principle of this gas sensor. A comprehensive analytical modelling on the resonant frequency characteristics has shown its major relationship with the thickness of the quartz substrate. Furthermore, analytical modelling has been done on the mass sensitivity of the device by altering the significant parameters such as the radius of electrode which serves as a critical candidate in deciding the mass loading area and understanding the energy trapping effect of the quartz crystal.

Moreover, the standard analytical modelling cannot withstand variations in the electrode size, structure or the material used. Thus, in order to verify the analytical modelled results and to extract the optimised critical design parameters, finite element analysis has been done. The finite element analysis in the COMSOL Multiphysics has

determined the optimal value for the significant design parameters such as the thickness and radius of the quartz and gold electrode and their interlink with the resonant frequency characteristics of the device. Investigation on the electrode structures are carried out through finite element analysis which exposed its relationship between the distribution of the sensitivity and the electrode depending on its structure. Comparison between the classic circular electrodes and the ring electrodes are studied and analyzed to improve the electrode structure.

Furthermore, a novel design of electrode structure called as the concentric electrodes is proposed in order to overcome the uneven mass sensitivity distribution limitations in the standard electrode structures such as the circular and ring electrodes. In this new design, there are two main parameters that are significant for the higher sensitivity such as the width of the rings and the gap between the rings which are altered with the finite element analysis to provide an approximate uniform mass sensitivity distribution. Then, these customized electrodes are designed and placed in an array.

Two types of array have been proposed which are the un-etched and etched monolithic quartz crystal microbalance (QCM) arrays. The un-etched monolithic QCM array has a 5MHz fundamental frequency of operation while the etched monolithic QCM array has a 10MHz and 33MHz fundamental frequency of operation. Array configuration produces frequency interference between the channels. Therefore, in order to eliminate the frequency interferences, the distance between the electrodes are altered and the dual inverted mesa structures are introduced. Finally, in order to fabricate the proposed quartz crystal microbalance sensor array with customized electrodes, possible fabrication

procedures are investigated and a feasible process procedure to fabricate the device is proposed.

1.3 Thesis Outline

In Chapter 2, various types of gas sensors are investigated based on their detecting mechanism. Their advantages and disadvantages are reviewed to eventually find the optimal gas sensor with the necessary qualities.

Chapter 3 is the detailed study of the principle of operation of the quartz crystal microbalance gas sensor and its working mechanism. The frequency and mass change interrelation and the piezoelectric effect are studied.

Following this, comprehensive analytical modelling and finite element analysis has been done in the Chapter 4. The resonant frequency characteristics of the proposed quartz crystal sensors are theoretically analyzed and the mass sensitivity relationship with the size of the electrode are investigated using Sauerbrey's equation followed by the investigation of the critical design parameters of the proposed device such as the radius and thickness of quartz and gold in order to determine their relationship with device overall performance with the finite element analysis.

Chapter 5 presents the study and analysis of the device electrode structures and their relationship with the mass sensitivity of the proposed device along with the comparison between the conventional circular electrode and the ring electrode. A novel design of the electrode structure called as the concentric electrode is proposed. The significant design parameters of the proposed electrode which determine the efficiency of the sensor are investigated and optimised through the finite element analysis. Their advantages comparative to the conventional electrodes are presented.

Chapter 6 presents the monolithic multiple electrode design of the quartz crystal microbalance sensor in an array configuration. Two types of monolithic QCM arrays are proposed in this chapter. In order to eliminate the frequency interference in the array, finite element analyses are conducted and the following simulation results are used to develop an optimal configuration and distance between the electrodes in the array. Furthermore, in order to reduce the size of high frequency QCM array, dual inverted mesa structures are proposed and the critical design parameters are analyzed and optimized.

Chapter 7 presents the fabrication process steps of the proposed sensor. The fabrication steps are aimed to be less complicated as possible compared to the other gas sensors to manufacture the device easily without compromising the performance.

Finally, Chapter 8 summarizes the work done in the thesis along with the significant results obtained through this research. Then potential future works that can improve the overall efficiency such as the addition of suitable sensing layer depending on the application are further provided.

CHAPTER 2

GAS SENSOR TECHNOLOGY

Gas sensing technology has played a major role for several decades in many medical, safety and detecting applications such as food quality detection [19], chemical vapor detection [20], air quality monitoring [21], space exploration applications [22] and electronic noses [23]. Several types of gas sensors are commercially available for detecting volatile organic compounds depending upon the concentration and type of volatiles. These types of gas sensors are categorized based on their detecting mechanism which are further reviewed, investigated, and analyzed in this chapter.

2.1 Introduction

Gas sensors are commonly categorized based on their detecting mechanisms. The functionality of majority of gas sensors depends on the electrical characteristic variation such as the resistance [24] and capacitance [25] or the frequency variation [26] to detect the target gas. These significant measurement variations are caused due to the fact that if a target gas comes into contact with the sensor then a critical parameter undergoes variation in the sensor which can be further mapped to detect the concentration or presence of the target gas [27]. The efficiency of the gas sensor is measured in terms of the sensitivity, selectivity, reversibility, accuracy, range of detection, recovery time and the response time [28-30]. Multiple channels in a gas sensors is useful to detect multiple gas target simultaneously and it is a significant quality in gas sensing because an array of sensors can provide high accuracy in the detection compared to the single channel gas sensors.

The qualities of an ideal gas sensor for sensing multiple volatile gas targets are listed below,

1. Ability to provide high sensitivity towards volatile organic compounds.

2. Possibility for design modification to detect multiple target volatile organic compounds simultaneously.

3. Diverse sensing materials compatibility.

4. Simple design geometry and ease of fabrication.

5. High reversibility and reproducibility.

6. Comparatively robust design.

7. Miniaturized structure and low of cost.

The above qualities have the potential to provide a robust candidate sensor for complex environment gas detection and the sensors that carry such qualities will be investigated in this chapter.

2.2 Sensors Based on Electrical Variations

2.2.1 Chemiresistor Sensor

Chemiresistor sensor operates based on the variation in the resistance of the sensor when the target gas comes into contact with the sensing material. Conventional chemiresistor sensor geometry includes interdigitated electrodes (IDE), and a sensing material that is deposited on the active surface of the sensor embedded on a silicon substrate. The electrical variation occurs when the sensor comes into contact with the target gas, which forms the basic working principle of the sensor as shown in the Figure 2.1 [31]. When the target gas comes into contact with the sensing material, the physical and chemical properties of the sensing material bridging the electrodes undergoes

changes, which as a result increases or decreases the resistance of the sensing material. This change in the resistance are then measured to detect the concentration or presence of the target gas by connecting the two electrodes to an external data processing unit to analyze the physical and chemical changes in the sensing film. The chemiresistor can employ a wide range of sensing material which further determines the properties of the sensor such as the reversibility and lifetime [32].
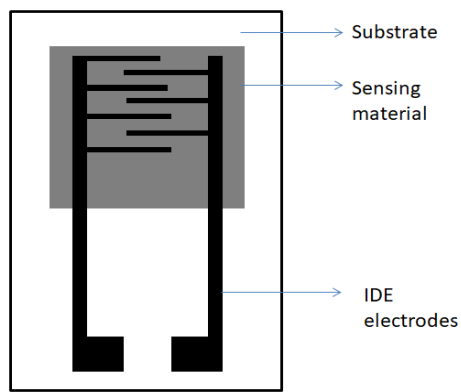
Fig. 2.1: Top view of a chemiresitor sensor showing the sensitive material and interdigitated electrodes (IDE) on a silicon substrate.

Chemiresistor sensors are built with the simplest structural configuration among the gas sensors. The chemiresistor sensors are fabricated with the sensitive material bridging the gap between the two electrodes which is mounted on the silicon substrate. The electrodes are usually made of gold or chromium for their high conductive and inertness property. The sensing material is responsible for the conductance between the electrodes. Owing to their simple geometry, they are highly preferred in the food aroma sensing and industrial applications. They also benefit from the wide range of sensing materials such as conducting and non-conducting polymers, grapheme, nanoparticles and metal oxides [33].

Although possessing wide range of advantages such as the high sensitivity, ease of fabrication, wide ranges of available sensing materials, chemiresistor sensor lacks selectivity and they are highly sensitive towards humidity and temperature present in the environment [34]. Furthermore, they also have low selectivity in the detection of target gases depending on the choice of sensitive materials such as polymers.

2.2.2 Metal Oxide Semiconductor Sensor

Metal oxide semiconductor (MOS) sensors are a different version of the common chemiresistor sensor with a micro heater unit and the metal oxides as their sensing materials. They are preferred for their accuracy rate, long lifetime, short response time and easy integrations in electronic circuits. The working mechanism of the sensor depends on the change of conductance when the reducing or oxidizing gas comes into contact with the sensing material as shown in the Figure 2.2. This interaction changes the physical and chemical properties of the sensing material which forms the basis of this sensor [35]. Each metal oxide sensing materials are sensitive to a particular gas at a suitable temperature. This suitable optimum temperature can be provided by an electrically separated micro heater unit which heats the metal oxides and makes the sensing material reactive to various gas targets as per the requirement. The MOS sensing material can be classified into n-type and p-type materials [36]. Some of the n-type metal oxides are TiO_2, ZnO, SnO_2 and WO_3 and p-type metal oxides are NiO, Mn_3O_4 and Cr_2O_3. The majority charge carriers in the n-type MOS are electrons. The reactivity of n-type MOS with reducing gas increases the conductivity and its reactivity with the oxidizing gas increases the conductivity. Whereas, the majority charge carriers in the p-type MOS are holes. The reactivity of p-type MOS with reducing gas decreases the

conductivity and the its reactivity with the oxidizing gas decreases the conductivity. These changes in the conductivity are measured with an external circuit or signal processing unit which forms the basic working principle of the sensor [37].
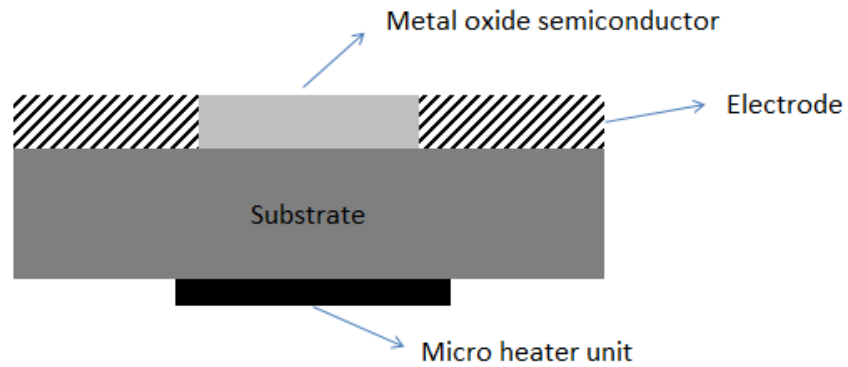
Fig. 2.2: Side view of metal oxide semiconductor sensor with a micro heater unit.

The metal oxide semiconductor gas sensors have a complex geometry due to the integration of the micro heater unit which needs electrical isolation area in the design. The sensor consists of two inter digitated electrodes (IDE) connected by the metal oxide sensing material. The micro heater unit is placed below the substrate material in order to have a full coverage for the heat. They are electrically isolated by an insulating layer with high temperature tolerance. The device is commonly built on a silicon substrate.

Metal oxide semiconductor has advantages such as the measurement simplicity, durability, low cost, long lifetime and a wide range of sensing materials. However they have some practical limitations such as the higher power consumption of the micro heater which limits the portable applications and the heating units are not always preferred in the bio sensing applications. Although array configuration is possible with this sensor, the heat dissipation on a large scale array is considerably difficult to manage [38-39].

2.2.3 Conducting Polymer Sensor

The conducting polymer sensor are known for their wide range of available active sensing materials such as the polypyrrole (PPy), polyaniline (Pani), polythiophene (PTh) and their derivatives [40]. Conducting polymer sensors have many advantages such as the high sensitivity, simple design, short response time and stability at room temperature. However, they are sensitive to temperature changes and humidity. The conducting polymers possess fine mechanical properties which makes the fabrication of the polymer sensor process much easier than its competitive gas sensors as shown in the Figure 2.3. When the gas target gas comes into contact with the sensing polymer, the change in the doping levels occurs. The doping levels of the conducting polymers strongly depend on the chemical reaction with chemical gas. This interaction either dope or undope the sensing material which alters the conductance of the material. This change in electrical property is measured which forms the basic working principle of this sensor [41].
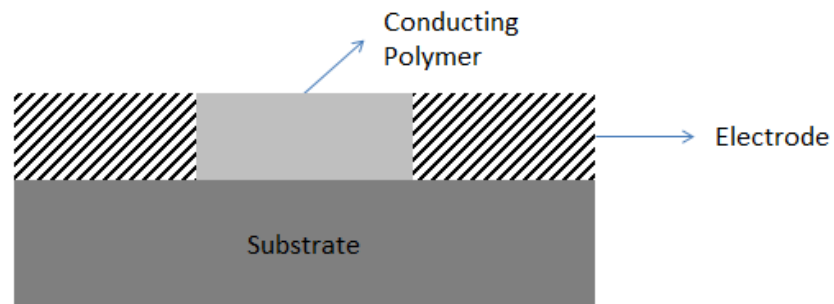
Fig. 2.3: Side view of conducting polymer sensor showing the employment of conducting polymer as the active sensing layer.

The polymer sensor consists of two electrodes usually made up of the gold for their high conductance and inertness properties which are interconnected with the polymer derivatives. The polymer material forms the active sensing layer. These conducting polymers can be synthesized either through the chemical or electrochemical process of oxidizing the corresponding polymer. These electrodes and the conducting

polymers are fabricated in the silicon substrate. In some cases, in order to improve the performance of electrical conductivity, inter digitated electrodes are employed [42].

Conducting polymers sensor has several advantages such as the high sensitivity, wide range of available polymers and short response time [43]. Nevertheless, they have some disadvantages including their sensitivity to the temperature and humidity [44], poor reversibility and they not suitable for array configuration as the sensor occupies large space [45].

2.2.4 Carbon Nanotubes Sensor

Carbon nanotubes are known for their extremely high adsorptive capacity even up to an atomic level which is considered as the significant reason for its excellent sensitivity and the popularity of the sensor [46]. Carbon nanotubes (CNT) possess several characteristics such as the high strength, large electrical and thermal conductivity, and high surface to volume ratios. These physical properties of the CNT provide smaller dimensions for the overall size and higher electrical sensitivity for the sensor. CNT are utilised in various types of sensors such as the resistive, capacitive and resonant frequency change sensors [47]. However, the resistive type of measurement is the most used sensor with CNTs owing to their simple geometry as shown in the Figure 2.4. The interaction between the CNT and the target gas causes changes in the physical properties of the CNT such as increase in the mass which subsequently increases the resistance and decreases the conductance. CNT sensor uses conductance as the measurable variable. This change in the electrical current can be measured which forms the basic working principle behind the CNT sensors [48].
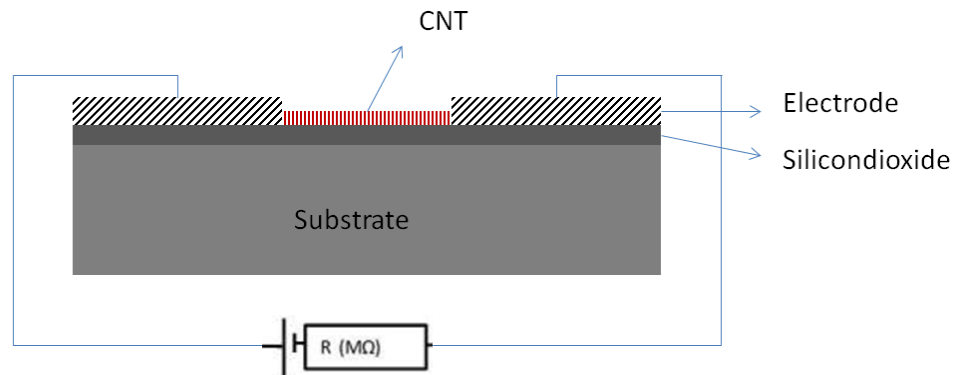
Fig. 2.4: Side view of carbon nanotube sensor showing the highly adsorptive carbon nanotube as the sensing matrial with the ohmmeter as the measurement unit.

The carbon nanotubes can be either single walled or multi walled with varying band gaps which act as semiconducting structures. The design of the CNT sensor is more similar to the MOS gas sensor. The carbon nanotube sensors consist of electrodes bridged by the carbon nanotubes which act as the active sensing layer. The source and drain electrodes are connected by this CNT while the gate is insulated by the dielectric barrier layer such as the silicon dioxide layer built on the silicon substrate [49].

Carbon nanotube sensor has several advantages such as the high sensitivity, great adsorptive capacity. However, they have disadvantages such as the high in cost, complex procedures to synthesise the carbon nanotube, fabrication complexity, long recovery time, possible irreversible changes of carbon nanotube conductivity, poor selectivity and they are also sensitive to the ambient conditions such as the presence of humidity and gas flow rate [50].

2.3 Sensors Based on Acoustic Variations

2.3.1 Quartz Crystal Microbalance Sensor

The quartz crystal microbalance (QCM) sensor consists of AT cut quartz substrate sandwiched between the two electrodes. The AC voltage is applied on the top electrode

while the bottom electrode is grounded. Electrodes are usually made of gold or silver while chromium is used as the adhesive layer for the electrodes and substrate. Gold is mostly preferred as the electrode material due to its high conductivity and inertness property. Due to its simple design, it has high potential for alterations in the design and has the possibility to detect multiple gas targets simultaneously in the array configuration [51].

Quartz crystal microbalance sensor is a mass sensitive device, which can detect nanogram level of mass changes. Therefore, it is a preferred candidate sensor for various fields of applications where there is a need for detection of target gases at low concentration levels [52]. They are also preferred in the practical applications due to their simple geometry and low cost of fabrication without compromising its performance in sensing the gases. Due to their simple structure and geometry, the design modifications are quite easy as per the demand in complex multiple gas sensing applications as shown in the Figure 2.5. The quartz crystal microbalance depends on the piezoelectric property of the quartz substrate [53]. The piezoelectric effect of the quartz can be defined as the accumulation of charges in the surface of quartz crystal when they are subjected to physical or mechanical stress. This voltage produced is proportional to the amount of mechanical or electrical stress produced. In turn, when an AC electric potential is applied across the quartz crystal, a mechanical deformation is produced and the crystal undergoes thickness shear mode of oscillation at the resonant frequency. Any mass changes in the electrically active area during the oscillation produce a direct shift in the resonant frequency of the quartz [54]. These variations in the resonant frequencies can be

measured with an impedance analyzer, which form the basic working principle of the quartz crystal microbalance sensor [55].
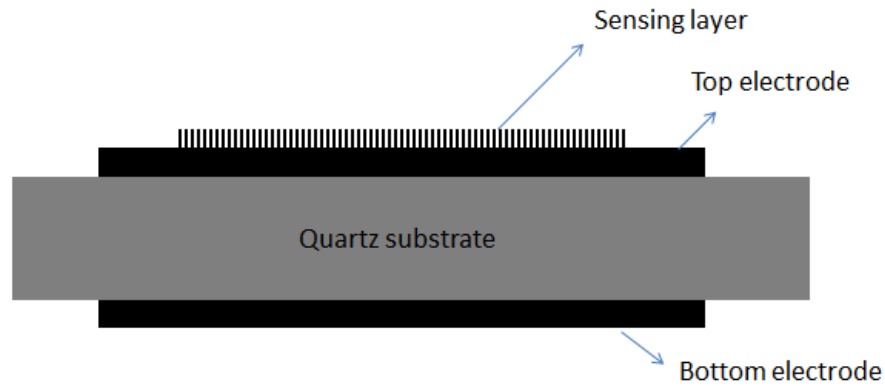
Fig. 2.5: Side view of quartz crystal microbalance sensor showing the quartz substrate sandwiched between two electrodes.

The quartz crystal microbalance has several advantages in the case of volatile detection such as the high sensitivity, wide range of sensing materials, potential to detect multiple targets, simple geometry and ease of fabrication and reversibility depending on the sensing material and high selectivity. Some of the sensing materials such as the carbon nanotube, if used on the QCM sensor could result in sensitivity towards temperature and humidity [56]. Although the conventional QCM operates with single channel limiting its ability, design alterations are proposed to be made to operate in array configurations as it will be investigate in Chapter 6 of this thesis.

2.3.2 Surface Acoustic Wave Sensor

The Surface Acoustic Wave (SAW) gas sensor is made up of interdigitated gold transducers placed on the piezoelectric substrate. For the chemical and biological sensing applications, the appropriate sensing material such as the polymer, carbon nanotube and the metal oxides are coated on the surface layer which undergoes changes in the form of mass, viscoelasticity or the conductivity when the target gas comes into contact [57].

Surface acoustic wave (SAW) sensors are widely popular for their high sensitivity in gas applications and its ability to work in wireless modes. Such competitive advantages had received continuous research and technological attention for the SAW gas sensor [58].

The SAW gas sensor depends on the variations in the SAW during the propagation of the acoustic wave through the target gas. These variations are directly proportional to the concentration of the target gas in the sensing region of the SAW sensor. Initially, the surface acoustic waves are produced the interdigitated transducers implanted on the piezoelectric material. These surface acoustic waves travel through the surface region of the piezoelectric material depending on the order of the wavelength and are detected by the receiver interdigitated transducer as shown in the Figure 2.6. Surface acoustic wave undergoes change in either phase or frequency when they are interacted by the corresponding gas targets. These changes can be accurately measured with impedance analyzer or can be wirelessly received and processed which is the basic working principle behind this sensor [59]. There are three stages in the operation of the SAW gas sensor,

   i.   Excitation of the piezoelectric substrate with the interdigitated transducer (IDT) to produce acoustic waves.

  ii.   Acoustic waves undergoing modulation due to their interaction with the target gases.

 iii.   Detection of the change in acoustic wave with interdigitated transducer.
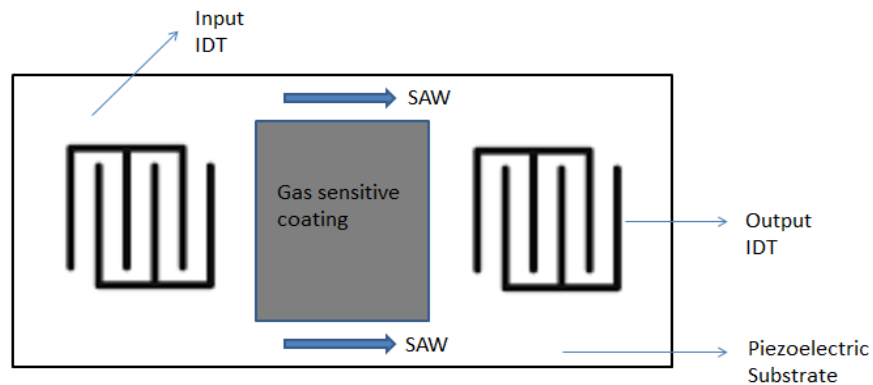
Fig. 2.6: Top view of surface acoustic wave sensor showing the propagation a SAW waves across the sensing material from IDT.

The surface acoustic wave sensor has advantages such as the high sensitivity, excellent response time, smaller size, wireless mode of operation, and planar structure. Although possessing such high advantages, it is inevitable for disadvantages such as the complexity in the fabrication process and its difficulty to operate in an array configuration that is a requirement for gas detection in a complex environment. Array configuration ability is significant to detect multiple gas targets. The main difficulty in the design for an array configuration with SAW sensor is the process of reducing the size of the sensor comparative to the other competitive sensors such as the quartz crystal microbalance which can provide the similar performance without design complications. [60].

2.4 Sensors Based on Optical and Calorimetric Variations

2.4.1 Optical Sensor

The optical sensor consists of fiber optic cable with source of the light beam on one side and the receiver of the light on the other side. The source of the light is usually white light or laser and the receiver is the spectrometer analyser to detect the variations.

The cladding of the fiber cable is coated with the sensing material. The whole optic fiber setup is fabricated on the silicon substrate as shown in the Figure 2.7 [61].

Optical sensors are widely known for their high sensitivity in the gas sensing applications. The accuracy of the optical sensors is comparatively better than other competitive sensors. These fiber optic gas sensors depend on the pulse width modulation of the source light for sensing the target gas concentration [62]. Initially the beam of light is passed through the fiber optic from the source which is modulated by the interaction with the chemical gases. This modulation causes variations in the physical properties of the source white light beam which is measured at the receiver end through a photo voltaic reader. The refractive index of the source beam changes when an adsorption or scattering occurs due to interaction. This measured variation in the refractive index of the pulse width modulation is directly proportional to the concentration of the chemical gas detected at the sensing region. The sensitivity can be increased by employing the appropriate sensing materials [63].
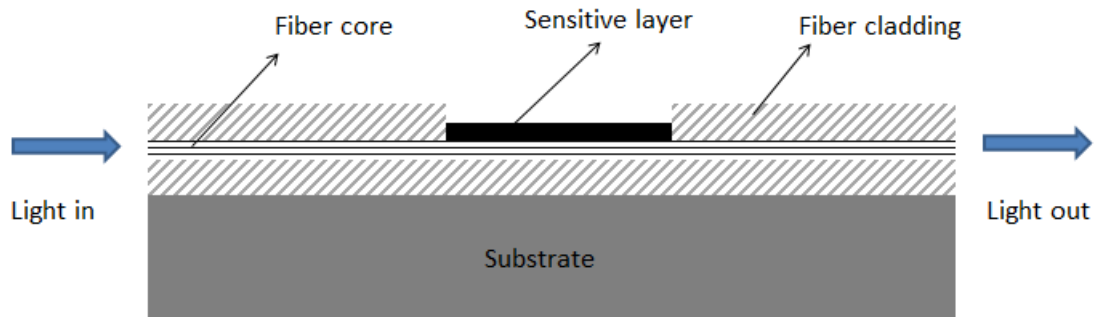
Fig. 2.7: Side view of optical sensor showing the light propagating through fiber and getting modulated due to the interaction with target gas.

The optical sensor has several advantages such as the high sensitivity, accuracy of detection, very good selectivity. It has disadvantages such as the higher size dimensions,

expensive setup and its difficulty to work in an array configuration for multiple targets detection simultaneously. Despite having several advantages, the optical sensors are not preferred in the volatile detection because of the difficulty in miniaturization and difficulty in array configuration setup [64].

2.4.2 Calorimetric Sensor

The calorimetric sensor has several chemi-adsorptive dyes implanted which turns colour when the target gas comes into contact with the sensing layer of the sensor. This interaction between the chemi-adsorptive dye and the gas undergoes chemical process and the colour of the dye changes. This change in the colour is further detected and calculated with a suitable image processing system and the presence of the target gas is detected. The calorimetric sensors are the most low cost gas sensor for the volatile detection and they work in an array configuration.

The calorimetric sensor some advantages such as the low cost, ability to work in array configuration and stability. However, it has disadvantages such as the irreversibility of the sensor response, long response time, low accuracy, high image processing power [65].

2.5 Conclusion

From a comprehensive analysis of the commercial and common gas sensors, the advantages and disadvantages of each individual sensor are analyzed and interpreted. This interpretation determines that there are various gas sensors which can be used to detect the volatiles. However, there are certain quality requirements specifically for complex environment applications in the sensor performances. Among all the investigated sensors, quartz crystal microbalance exhibits promising competitive

advantages over the other sensors such as its high sensitivity, reversibility, selectivity, long lifetime, robustness, simple design, ease of fabrication, potential for array configuration and low cost of fabrication. Thus, implementing this candidate sensor in an array configuration could provide a platform to detect multiple gas targets simultaneously. Since QCM exhibited most of the required qualities and potential, the focus of this thesis is on the design and development of high performance QCM sensor in an array configuration for volatile detection in a complex environment.

CHAPTER 3

QUARTZ CRYSTAL MICROBALANCE SENSOR

3.1 Introduction

Quartz crystal microbalance sensor is one of the candidate technologies for gas detection and has received a high attention in the research and development due to their advantages during the recent decades [66]. The simplicity in the design of this sensor combined with high potential qualities is one of the major reasons for this research focus. As discussed in the previous chapter, this sensor provides a competitive advantage and qualities over other gas sensors in its range such as the wide choice for the sensing material, potential to detect multiple gas targets in array configuration and smaller size. The working mechanism of the Quartz crystal microbalance sensor and its physics of operation are discussed and investigated in detail in this chapter.

3.2 Basic Structure and Mechanism of Operation

3.2.1 Quartz Crystal Microbalance – Design Principle

The Quartz crystal microbalance sensor is commonly built on an AT cut quartz crystal that usually has a thickness ranging between 330μm to 168μm as shown in the Figure 3.1 depending on the need for resonant frequency. The AT cut of the quartz crystal is achieved by cutting the quartz crystal 35° 15' degree to the principle optical axis of the crystal (z-axis) as shown in the Figure 3.2 [67]. The quartz crystal that are found in nature are rare and expensive, therefore, they are nowadays synthetically grown. These crystals are subjected to various process such as annealing and electrical sweeping in order to reduce the number of defects and impurities in the crystal, which may cause errors in their fabricated devices [68]. AT cut of quartz is usually preferred because of

22

their stability in operation and its temperature tolerance, which helps the device to operate even at higher temperature without causing shift in the frequency. Quartz can have piezoelectric effect even up to 573° C [69]. In a quartz crystal microbalance structure, this AT cut quartz crystal is sandwiched between the two metallic electrodes in order to apply the AC potential. In these devices, electrodes are usually made of gold, titanium, silver or platinum however, gold is preferred for its high conductivity and inertness property as it is chemically non-reactive. Although copper and silver are more conductive than the gold, they do not possess inertness property similar to gold [70].

| ■ Gold | ■ AT – cut Quartz substrate |

(a) (b)
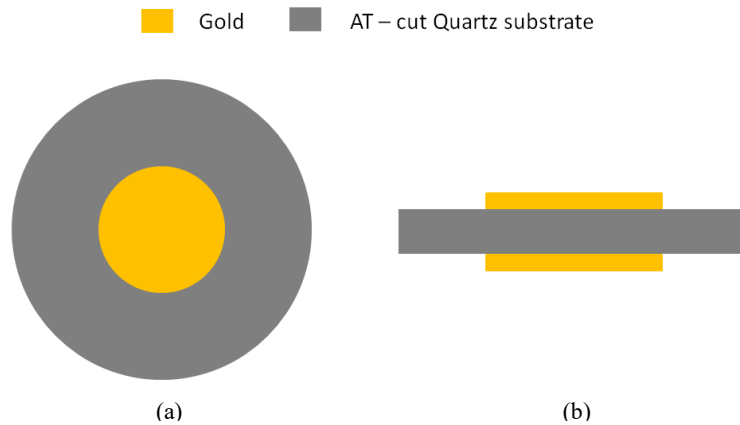
Fig. 3.1: Quartz crystal microbalance sensor (a) Top view of a quartz crystal microbalance sensor showing the top gold electrodes (b) Side view showing the quartz sandwiched between two gold electrodes.

(a) (b)
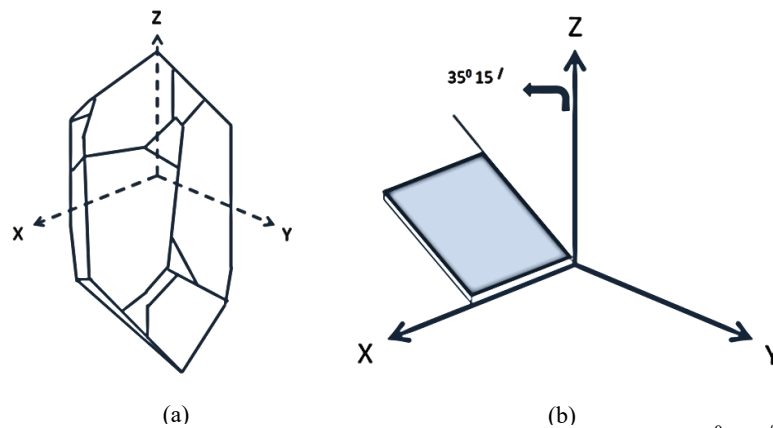
Fig. 3.2: Quartz crystal orientation (a) Quartz crystal (b) AT cut - crystal $35^0 \ 15^/$ degree to the z-axis

3.2.2 Thickness Shear Mode (TSM) Oscillation

Quartz is made up of silicon and oxygen bonds. These silicon and oxygen bonds have a non-linear nature, which results in a net dipole moment in the quartz. When an alternating current is applied across the metallic electrodes that are deposited on both sides of the crystal, the opposite ends of the dipole tend to pushed in the opposite directions followed by the dipoles tending to rotate themselves to be aligned along the direction of the applied electric field [71]. This displacement results in a net strain. The displacement in the dipoles of the quartz also varies with the electric field resulting in the mechanical deformational of the quartz crystal. As a result, the acoustic shear waves are launched in the direction perpendicular to the direction of the crystal from the either sides of the crystal. When this alternating current supply is removed, the crystal comes back into its original form from the deformed state due to the absence of strain in the crystal. The AT cut of the quartz is responsible for the thickness shear mode of oscillation as shown in the Figure 3.3. AT cut is mostly used in quartz-based applications because of its exceptional frequency stability [72].
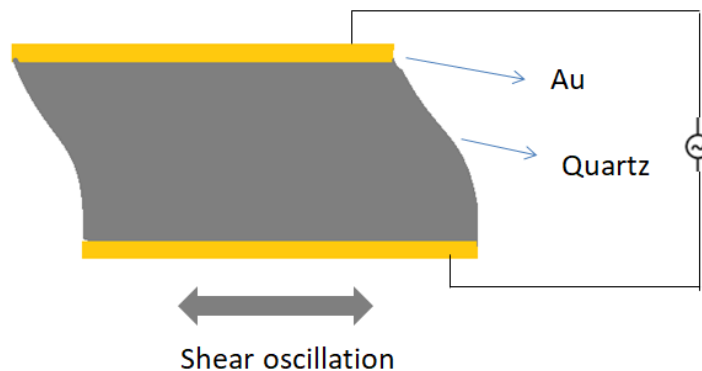
Fig. 3.3: Quartz crystal microbalance sensor undergoing th6wickness shear mode of oscillation when AC current is applied.

3.2.3 Piezoelectric Property of Quartz

The deformation of the quartz on the application of alternating current is the result of inverse piezoelectric effect. Since quartz is a piezoelectric crystal, it exhibits piezoelectric property which is the production of electric field in its surface when a mechanical stress is induced [73]. The magnitude of the electric current produced is directly proportional to the amount of stress applied on the crystal. Thus, inversely when an electric current in an alternating form is applied between the top and bottom electrodes, the quartz undergoes mechanical deformation in the form of an oscillation. Inverse piezoelectric effect is the responsible for the thickness shear mode of oscillation of the quartz crystal microbalance sensor [74].
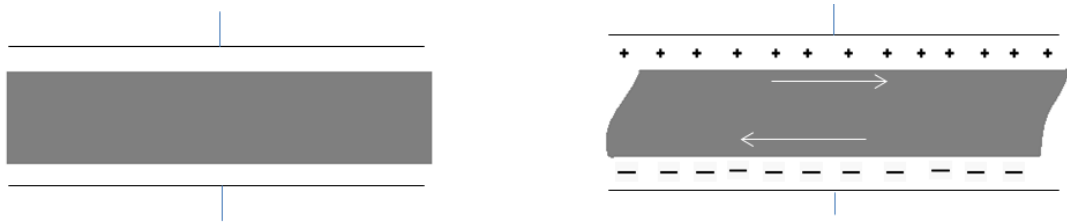
Fig. 3.4: Piezoelectric effect (a) Quartz crystal when no electric potential is applied (b) Quartz when electric potential is applied between its two electrodes and exhibiting inverse piezoelectric effect.

3.2.4 Resonant Frequency

The frequency at which the piezoelectric quartz crystal undergoes thickness shear mode of oscillation under the influence of applied alternating current (usually sine wave) is called as the resonant frequency. This fundamental resonant frequency of the quartz is used for sensing and acts as an indicator for the sensor exposure which undergoes variations. It either increases or decreases by a certain level of Hz depending upon the addition or removal of the mass on the surface of the electrically active sensing electrode area [75]. The addition of mass reduces the resonant frequency, while the removal of the

mass increases the resonant frequency. These variations in the resonant frequency can be monitored with a high frequency oscillator. The relationship between the frequency and mass in the quartz crystal microbalance was first observed by Sauerbrey, a German physicist in 1959 and devised equations called as the Sauerbrey's equation of mass and frequency relationship [76].

3.2.5 Sensitivity

The magnitude of variation in resonant frequency for a particular amount of mass determines the sensitivity of the Quartz crystal microbalance sensor. In an ideal case, Quartz crystal microbalance can detect up to 1ng amount of change in mass on its sensing electrode surface. If the center resonant frequency of the quartz crystal microbalance is higher, the sensor tends to be more sensitive towards the mass which results in a larger shift in the resonant frequency compared to sensor with lower center resonant frequency [77]. Although higher resonant frequency has advantage of more sensitivity, they are fragile due to their thin quartz substrate compared to lower resonant frequency sensor that uses comparatively thicker substrate [78].

3.3 Mass and Frequency Relationship

When an alternating current is applied on the metallic electrodes of a Quartz crystal microbalance, the device starts to oscillate at the resonant frequency [79] which is given by,

$$f_0 = \frac{\sqrt{\mu_q/\rho_q}}{2t_q} \qquad (3.1)$$

where, f_o is the resonant frequency of the resonating quartz crystal, μ_q is the shear modulus of the quartz crystal ($\mu_q = 2.947 \times 10^{11}$ g cm^{-1} s^{-2}), ρ_q is the density of the quartz crystal ($2.648 \times$ g cm^{-3}) and t_q is the thickness of the quartz crystal. Since μ_q and ρ_q are

constant values, the resonant frequency is directly influenced by the thickness of the quartz crystal.

This resonant frequency f_0 of the quartz changes either by addition or removal of the mass on the electrically active sensing area. This mass and frequency relation is devised in an equation by Sauerbrey,

$$\Delta f = -S_c \frac{\Delta m}{A} \qquad (3.2)$$

where, A is the area of electrodes of the quartz crystal microbalance, Δf is the change in the resonant frequency, S_c is the Sauerbrey constant equals to 2.264×10^{-6} g^{-1} cm^{-2} s and Δm is the change in mass on the surface of electrode. The negative sign denotes the reduction in the resonant frequency by addition of mass on the top of electrode. The Sauerbrey's equation of mass-frequency relationship is derived as follows:

$$m_q = \frac{M_q}{A} = t_q \rho_q \qquad (3.3)$$

where, m_q is the mass per unit area and M_q is the total mass of the quartz crystal. This Equation 3.3 is combined with 3.1, to obtain,

$$f_0 = \frac{\sqrt{\mu_q \rho_q}}{2m_q}. \qquad (3.4)$$

By addition of some quantity of mass to the electrode causes change in the resonant frequency which can be written as,

$$f_0 + \Delta f_0 = \frac{\sqrt{\mu_q \rho_q}}{2(m_q + \Delta m_{q)}}. \qquad (3.5)$$

Equation 3.4 is substituted in the above equation 3.5, to obtain,

$$\Delta f_0 = \frac{\sqrt{\mu_q \rho_q}}{2(m_q + \Delta m_{q)}} - \frac{\sqrt{\mu_q \rho_q}}{2m_q}. \qquad (3.6)$$

The above equation 3.6 is written as,

$$\Delta f_0 = \frac{\sqrt{\mu_q \rho_q}(-\Delta m_q)}{2m_q^2 \left(1 + \frac{\Delta m_q}{m_q}\right)}.$$ (3.7)

Substituting equation 3.4 in the above equation to obtain,

$$\Delta f_0 = \frac{f_0(-\Delta m_q)}{m_q \left(1 + \frac{\Delta m_q}{m_q}\right)}.$$ (3.8)

For a thin deposit, the Δm_q is lower than m_q, to obtain,

$$\Delta f_0 = \frac{f_0(-\Delta m_q)}{m_q}.$$ (3.9)

The above equation can also be written as,

$$\Delta f_0 = \frac{f_0(-\Delta m_q)}{t_q \rho_q}.$$ (3.10)

Then substituting equation 3.1 in the above equation to obtain,

$$\Delta f_0 = \frac{2f_0^2(-\Delta m_q)}{\sqrt{\mu_q \rho_q}}.$$ (3.11)

The above equation is rewritten as,

$$\Delta f_0 = -\frac{2f_0^2}{\sqrt{\mu_q \rho_q}}\frac{\Delta m}{A} = -S_c \frac{\Delta m}{A}.$$ (3.12)

Equation 3.12 is the Sauerbrey's equation which determines the relationship change in the resonant frequency and the mass change in the surface of the electrode.

Thus from the following derivation, it is found that the change in the frequency is directly proportional to the change in the mass. This equation 3.12 is used to calculate the resonant frequency variation of the proposed sensors in this work.

3.4 Sensor Equivalent Circuit Model

The equivalent circuit model study of the quartz crystal microbalance provides a better understanding of its principle of operation. It can be modeled in terms of mechanical and electrical form as follows.

3.4.1 Mechanical Equivalent Model

The mechanical model of the quartz crystal microbalance can be modeled with the mass (M), compliance (C_m), and a resistance (r_f). The compliance is the representation of the energy stored during the oscillation and the resistance is the representation of the energy dissipated during the oscillation [80].
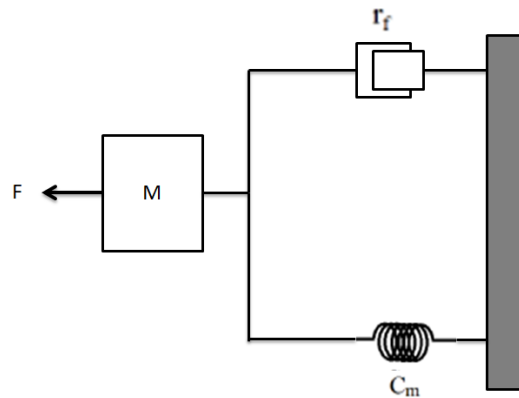
Fig. 3.5: Mechanical equivalent model of the quartz crystal microbalance.

3.4.2 Electrical Equivalent Model

The mechanical equivalent circuit of the quartz crystal microbalance can be modeled as the electrical circuit in the Resistor, Inductor and Capacitor (RLC) form. The electrical equivalent model consists of basic RLC circuit where the R represents the energy dissipated during the oscillation, C represents the energy stored during the oscillation and L represents the inertial component related to the dissipated mass. The addition of the electrodes in the quartz crystal microbalance adds a capacitance to the

circuit. These RLC parameters of the equivalent circuit can be divided into motional components and static components.
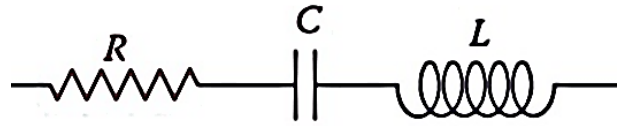
Fig. 3.6: Electrical equivalent model of the quartz crystal microbalance without electrode contact.

The motional components are the R_m, L_m, and C_m which are derived from the resonance operation of the QCM and the additional parallel static capacitor C_0. The addition capacitor C represents the dielectric energy storage because the oscillation crystal is established between the top and bottom electrodes. This model is called as the Butterworth Van Dyke (BVD) equivalent circuit [81].
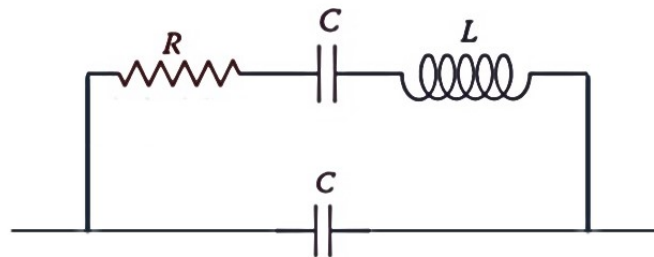
Fig. 3.7: Electrical equivalent model of the quartz crystal microbalance with electrode contact (Butterworth Van Dyke equivalent circuit).

The mass variation of the quartz crystal changes the inductance in this equivalent circuit. Both the series resonant frequency and the parallel resonant frequency depend upon inductor element which is also the function of the mass displacement. When the thin film is deposited on the surface, the decrease in the frequency can be correlated to the increase in mass using the Sauerbrey's equation.

$$\Delta f_s = -\frac{2f_0^2 mn}{\sqrt{\mu_q \rho_q}} \qquad (3.13)$$

where, f_0 is the resonant frequency, m is the mass added, n is the harmonic number and the μ_q and ρ_q represents the density and shear modulus of quartz.

3.5 Conclusion

The basic physics involved in this sensor's operation including the piezoelectric effect of quartz, highly conductive gold electrode with inertness property, thickness shear mode oscillation, and resonant frequency of the device are studied. The mechanical and electrical equivalent circuits provided a better understanding of the device. The Sauerbrey's equation of mass and frequency change derivation has provided the basic understanding of the working principle behind the sensor. It has also disclosed the inversely proportional relationship between the thickness of the quartz crystal and the resonant frequency. Although it has provided the basic relation between the mass and frequency change of the quartz crystal, they needed to be analyzed furthermore for a more complex configuration proposed in this thesis as well as the designed sensor arrays by plugging in with the real time values for analytical modeling which is done in the following next chapter.

CHAPTER 4

DESIGN PARAMETER ANALYSIS AND MODELLING

4.1 Introduction

The quartz crystal microbalance sensor design is comprised of several critical design parameters that influence the output performance of the device. The influencing design parameters include thickness and radius of the quartz substrate as well as the metallic gold electrode, along with the electrode configuration. These critical design parameters have a direct effect on the performance of the device including the resonant frequency of the oscillating crystal and mass loading area on the electrode surface. Using the analytical modeling techniques, the prior mentioned significant critical parameters can be modeled and analyzed. However, they cannot be applied when some of these design parameters such as the electrode dimensions of the quartz crystal microbalance is complex and customized. This demands the need for finite element analysis which can accurately model the device despite having complex geometries in the design and increase the overall output performance. Therefore, the following analytical modeling and finite element analysis are done in this chapter to investigate and analyze the effect of design parameters in order to optimize the device sensitivity and functionality.

4.2 Quartz Crystal Microbalance - Analytical Modeling

The analytical modeling of the quartz crystal microbalance sensor can be carried out based on the Sauerbrey's equation of mass and frequency change relationship [79] shown below as,

$$\Delta f = -\frac{2f_0^2}{\sqrt{\mu_q \rho_q}}\frac{\Delta m}{A} \qquad (4.1)$$

where, μ_q is the shear modulus of the quartz crystal ($\mu_q = 2.947 \times 10^{11}$ g cm^{-1} s^{-2}), ρ_q is the density of the quartz crystal ($2.648 \times$ g cm^{-3}), A is the area of electrodes of the quartz crystal microbalance, Δf is the change in the resonant frequency, Δm is the change in mass on the surface of the electrode.

The parameters $\mu_q \rho_q$ are the constant values depending on the quartz crystal properties while the parameters A and f_0, the resonant frequency are the variable parameters which are further studied and analyzed.

4.2.1 QCM Resonant Frequency

Since quartz is a piezoelectric crystal, a shear displacement occurs in the quartz, when an alternating current is applied between the top and bottom electrodes. The applied alternating current produces a resonant oscillation in the quartz crystal when the wavelength of the shear displacement in the quartz crystal corresponds to double the thickness of the substrate. The frequency at which this process occurs is called as the resonant frequency. Based on the following equation, the resonant frequency is dependent on the thickness of the quartz crystal which increases if the thickness of quartz is reduced and decreases if the thickness of the quartz is increased.

$$f_0 = \frac{\sqrt{\mu_q/\rho_q}}{2t_q} \qquad (4.2)$$

where, t_q is the thickness of the quartz crystal which is inversely proportional to the resonant frequency of the crystal. In order to investigate the change in the resonant frequency with the change in the quartz thickness for the range of available quartz substrate, the thickness of the quartz is varied and the resonant frequency values are plotted. In this study, the $\mu_q = 2.947 \times 10^{11}$ g cm^{-1} s^{-2} and $\rho_q = 2.648 \times$ g cm^{-3} are the constant values which depend on the physical properties of the quartz. Figure 4.1 shows

33

the analytically modeled results showing the relationship between the thickness of quartz with the fundamental resonant frequency. It states that the resonant frequency increases with the decrease in thickness of the quartz crystal.
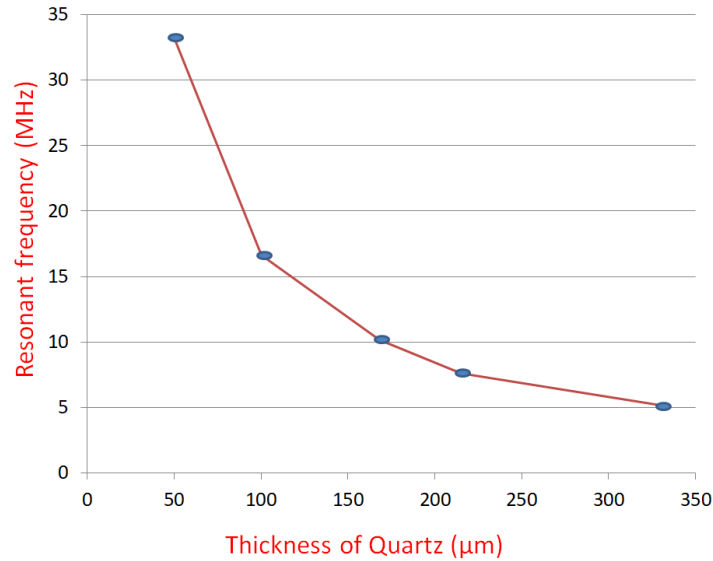
Fig. 4.1: Analytical modeling result presenting relationship between the resonant frequency, f_0, and the thickness of quartz substrate, t_q.

The most commonly used fundamental resonant frequency for the quartz crystal microbalance ranges between 5 MHz and 10 MHz because stability in the design structure associated with the thickness of the quartz and their compatibility in un-etched array design, thus suitable for the practical applications [82]. Within this range, a higher frequency quartz crystal microbalance can provide a larger response to the deposited thin film mass compared to the quartz crystal microbalance with lower resonant frequency. This means that a device with a higher resonant frequency is more sensitive to the mass changes compared to a lower resonant frequency device. However, the limitation for a higher resonant frequency is that if the thickness of quartz is reduced, the quartz substrate becomes thinner and fragile that makes it prone to breakage which might limit it usage in the practical applications such as an electronic nose portable device. The requirement for

the portable sensor system suggest to employ a quartz crystal microbalance that is robust but without a significant degradation in the device sensitivity and performances [83].

4.2.2 Frequency and Mass Relationship

The ability of the quartz crystal microbalance to detect the mass changes arises from the Sauerbrey's equation of relationship between the change in frequency and change in mass. This equation is the linear relationship between the resonant frequency of the oscillating crystal and the mass changes given by,

$$\Delta m = -C.\Delta f /n \qquad (4.3)$$

where, C is the constant value depending on the properties of quartz and n is the overtone number. For a most common standard 5 MHz crystal, the constant C value equals 17.7 ng. cm^{-2}. Hz^{-1}. This indicates that if 17.7 nanogram of mass is adsorbed on a centimeter square area of the top active electrode surface, resonant frequency of about 1 Hz is reduced or in other words, about 0.057 Hz is reduced when 1 nanogram of mass is adsorbed. The above equation can be used when the deposited mass on the quartz crystal microbalance is a thin layer of rigid film which is firmly attached to the crystal surface. However, if the attached mass layer is soft, thick or not coupled to the surface, then this equation cannot be applied [84].

In order to investigate the expected range of frequency change for a practical change in the mass, the center frequencies are calculated with the increased area of the electrode of 500µm on a 5 MHz crystal. The linear characteristic of the change in mass and frequency equation is shown in the following Figure 4.2.
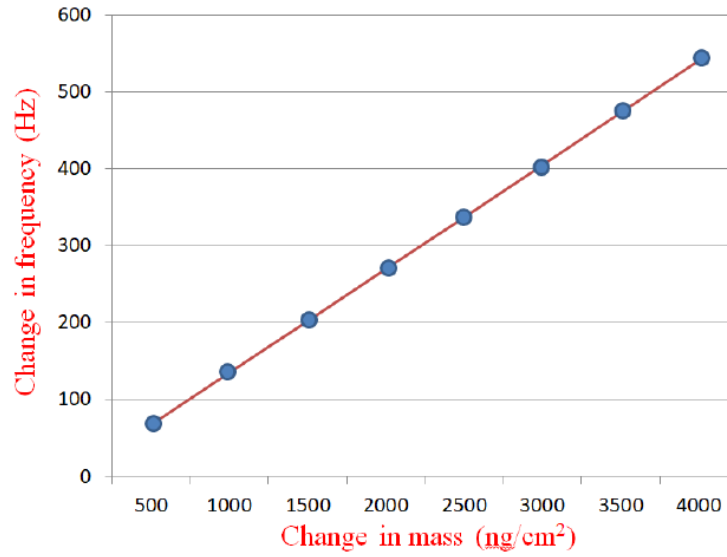
Fig. 4.2: Analytical modeling result presenting the linear relationship between the mass and frequency with a sensitivity of 0.135 ng. cm^{-2}. Hz^{-1}.

Therefore, the sensitivity of the sensor also depends on the size of the electrode which can be explained by equation

$$A = \pi r^2 \tag{4.4}$$

where, A is the area of the top sensing electrode and r is the radius of the sensing electrode. Thus it is clear that the size of the sensing electrodes is a significant factor for the sensitivity of the quartz crystal microbalance sensor.

4.2.3 Mass Sensitivity (Δf/Δm) and Radius of the Electrode (r) Relationship

The radius of the electrode is directly affecting the sensitivity of the device. According to the Sauerbrey's equation, the smaller radius of electrodes provides a higher mass sensitivity compared to a larger radius of electrode. The magnitude of this sensitivity variation of the device is larger with higher resonant frequency device compared to the device with lower resonant frequency as shown in the Figure 4.3 and 4.4.
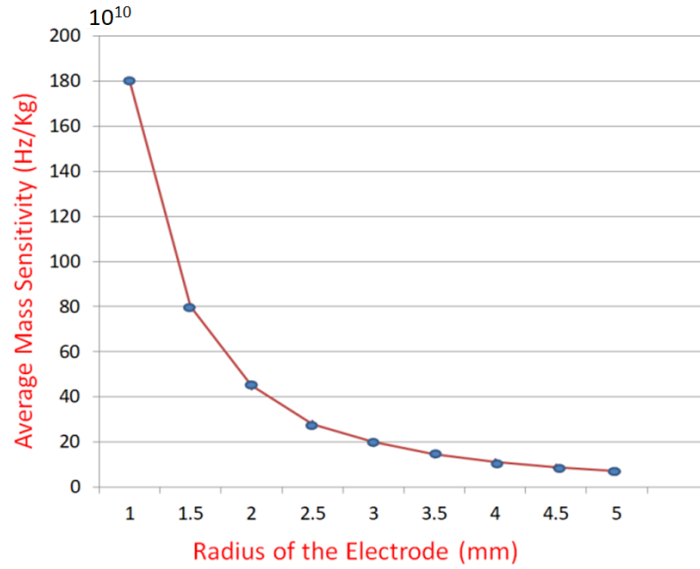
Fig. 4.3: Analytical modeling result presenting relationship between the average mass sensitivity (Δf/Δm) and radius of the electrode (mm) for a 5MHz quartz crystal microbalance sensor.
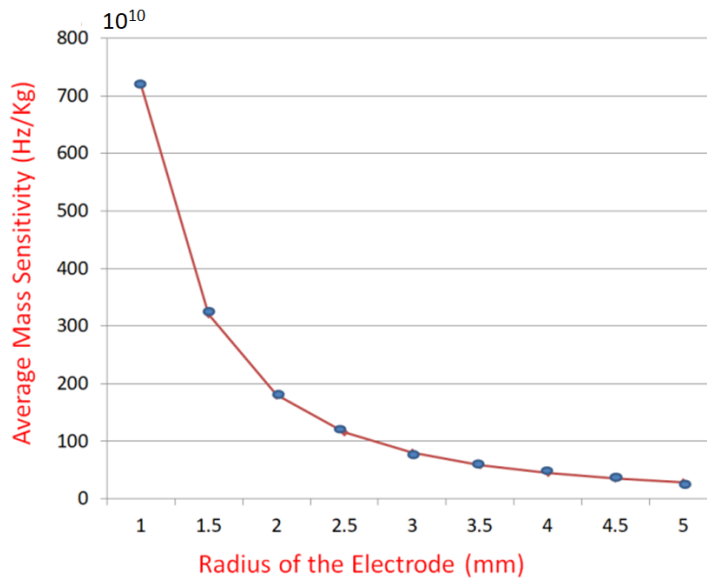
Fig. 4.4: Analytical modeling result presenting relationship between the average mass sensitivity (Δf/Δm) and radius of the electrode (mm) for a 10 MHz quartz crystal microbalance sensor.

From Figures 4.3 and 4.4, the significance of a smaller electrode is determined as it provides a higher average mass sensitivity. Despite providing a higher mass sensitivity for the device, it also has a disadvantage of reduces mass loading area. This phenomenon

of trapping of energy at the center of quartz is called as the energy trapping effect. Due to this energy trapping property of quartz, most of the energy is trapped on the center of the electrode while the quartz acting as an acoustic lens [84-85]. The distribution of the mass sensitivity in the quartz can be described as a Gaussian curve in the radical direction due to the energy trapping effect. Therefore, it is shown that a larger mass loading area on the surface of the active top sensing electrode is required for a better performance. This is due to the fact that a larger mass loading area provides a platform for more target gas to interact with the quartz crystal microbalance which in turn produces a higher shift in the resonant frequency compared to lower mass loading area [86].

Although the resonant frequency and mass sensitivity characteristics are modeled in the analytical modeling, the same modeling techniques cannot be applied when the shape of the electrodes are complex as proposed in this research work or when the mass layer is applied on the top electrode similar to the application of this work. Thus, with the help of finite element analysis, the device can be modeled for various customized structure of electrodes, array configurations and also to analyze its critical design parameters.

4.3 Finite Element Analysis

The finite element analysis is the process of simulating the predefined physical phenomenon using the numerical technique called finite element method. Finite element analysis technique is used to design customized geometric designs of a device because in some cases that need complex modifications, the analytical modeling cannot model complex structures and provide the results. This technique of finite element analysis can also be useful to reduce the number of needed physical prototypes and experiments.

In the case of quartz crystal microbalance sensor, the theoretical calculations can be used only to understand the basic conventional design of the device. The need for a multiple sensors on the same substrate in an array configuration or to determine the effect of certain design parameters on the performance of the device such as the thickness of the electrode, radius of the quartz can be modeled and optimized with the finite element analysis methods.

4.3.1 COMSOL Multiphysics

COMSOL Multiphysics can combine multiple physics based environment, set complex boundary conditions in multi-dimensional forms, and build detailed geometry structures for analysis [87]. It has wide range of materials with predefined physical properties which can be applied for the designed geometries. The COMSOL is also integrated with an ample physics conditions and features with which a virtual prototype of quartz crystal microbalance can be accurately designed and modeled. With the help of this comprehensive modeling tool, meshes can be built. Furthermore, it has a wide range of study collection and post processing abilities.

4.3.2 Meshing Characteristics

In COMSOL Multiphysics after building the geometry, assigning the boundary conditions and setting the physics conditions, the designed model has to be meshed before conducting the comprehensive study. The mesh is a vital part in deciding how the designed geometry is solved. The meshing characteristics define the way in which the geometry in divided, shape of the mesh elements, size and density of the elements. The following physics controlled meshes can be set in the predefined meshing qualities such as,

- extremely fine,

- extra fine,

- finer,

- fine,

- normal,

- course,

- courser,

- Extra course and extremely course.

Depending on the following predefined meshing qualities, the COMSOL software divides the geometries into segments of small sizes, shape and density. Increasing the density of the meshing provides more accurate results with the cost of processing power and time. Thus in order to get the most accurate results in the best possible minimal time, the meshing characteristics of the COMSOL is conducted on the basic geometry of the quartz crystal microbalance and analyzed. The parameters of the quartz crystal microbalance are set as per the Table 4.1 and the meshing characteristic analysis is conducted for the primal meshes.

Table 4.1: Dimensions of the quartz crystal microbalance sensor for mesh accuracy analysis

Parameters	Value	Unit
Radius of quartz	12	mm
Thickness of quartz	333	μm
Radius of electrode	500	μm
Thickness of electrode	300	nm

The meshes are built starting from the normal to extra fine meshes since the course meshes are scarcely arranged. This meshing analysis has provided different results for the resonant frequencies from the adaptive frequency study. The segmentation of the different meshes in which the electrode areas are densely packed due to their smaller dimensions. The two dimensional plot of mechanical response gives the resonant frequency values which are captured and presented in the following Figure 4.5.
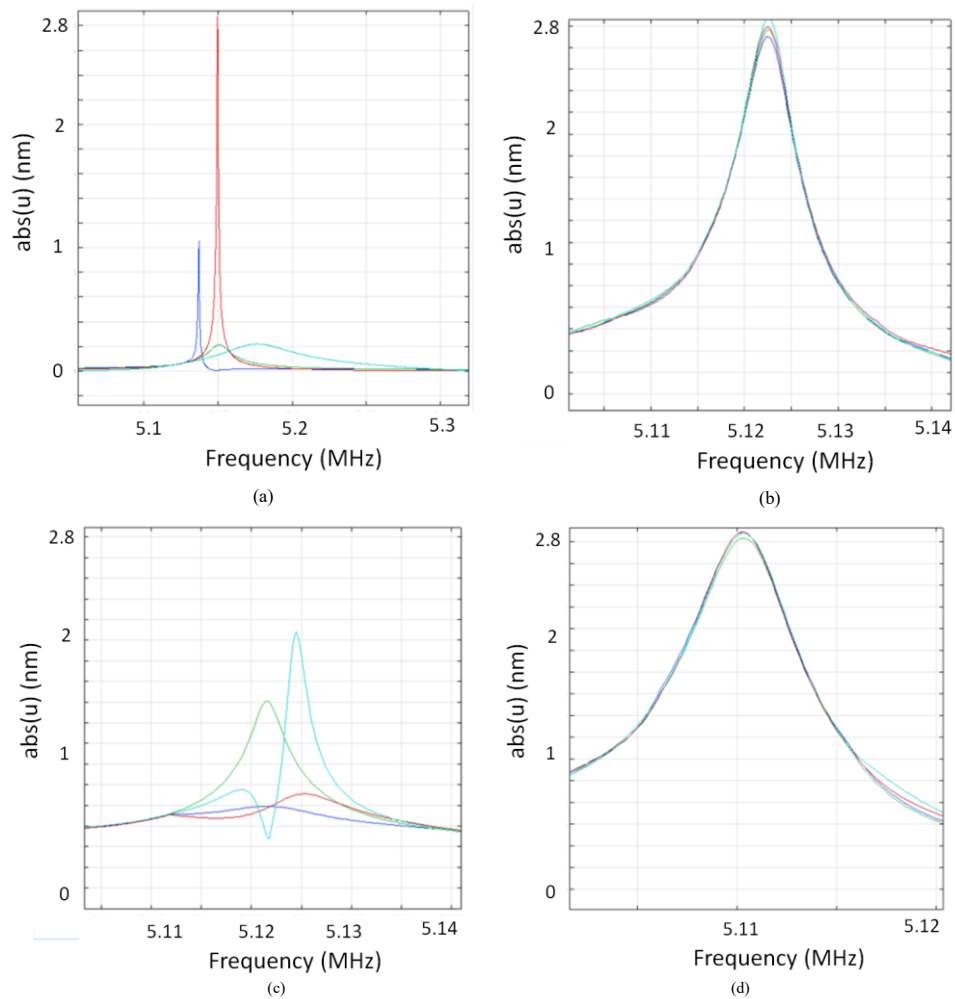
Fig. 4.5: COMSOL simulation results showing the resonant frequency characteristics to analyze the meshing characteristics (a) Normal mesh (b) Fine mesh (c) Finer mesh (d) Extra fine mesh.

From the following analysis, the resonant frequency of the sensing device is found to be constant when the meshing characteristics are finer and above as illustrated in

the Figure 4.6. The absence of any change in the resonant frequency after a certain mesh number is an indicator of the ability of finer mesh and beyond to provide independency to the meshing density results with the minimal possible simulation time. Moreover, meshing above the quality of finer meshing would take longer simulation times, while providing the same results as the finer meshing. Thus, the following finer mesh has been chosen for the upcoming simulations of the proposed designed sensors in this work. Furthermore, this analysis on the meshing characteristics has assured the independency of the results to the meshing density during the finite element analysis simulations.
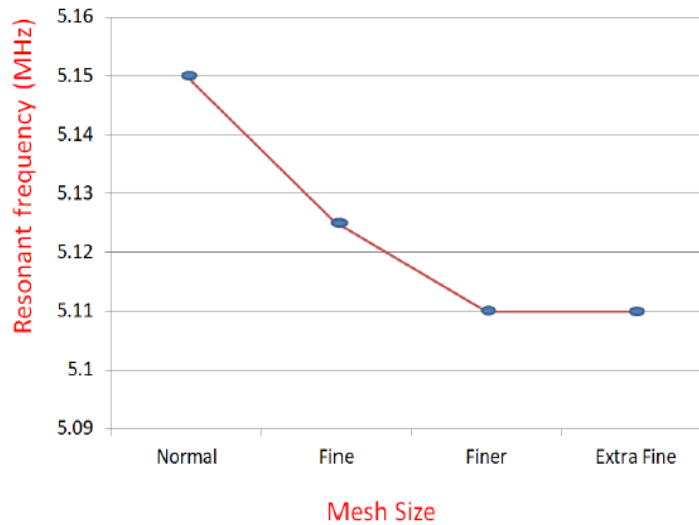
Fig. 4.6: COMSOL simulation results illustrating the effect of meshing on the output resonant frequency.

4.3.3 Investigation of Thickness of Quartz Crystal

The thickness of the quartz crystal is an important parameter which determines the basic fundamental resonant frequency of the quartz crystal microbalance sensor. This fundamental resonant frequency determines the basic sensing capability of the sensor also through the Sauerbrey's equations. From the analytical modeling, it is been found that the resonant frequency increases when the quartz crystal thickness is decremented and

decreases when the quartz crystal thickness is incremented. In order to verify the results of analytical modeling and also to analyze its behavior for a more complex sensor configuration, the finite element analysis of thickness of quartz is carried out in COMSOL software.

Accordingly, the geometry of the quartz in the form of a cylinder is built with the inbuilt COMSOL kernel and the boundary conditions are set to be free material. In order to eliminate any external mass factors on the quartz crystal, the electrodes are removed for this frequency analysis and the alternating current is applied on the top and bottom of the quartz substrate. Due to the absence of complex geometrical structures, the mesh size is kept user controlled in order to reduce simulation time. A parametric sweep from 50μm to 333μm is selected and the adaptive frequency study is conducted in the COMSOL in order to analyze their resonant frequency response by plotting the frequency versus the displacement. The frequency in which the highest displacement takes place in the following plot represents the resonant frequency. Abs(u) is the function of displacement. The values are plotted in a two dimensional graph in the COMSOL and shown in the Figure 4.7.

(a)   (b)
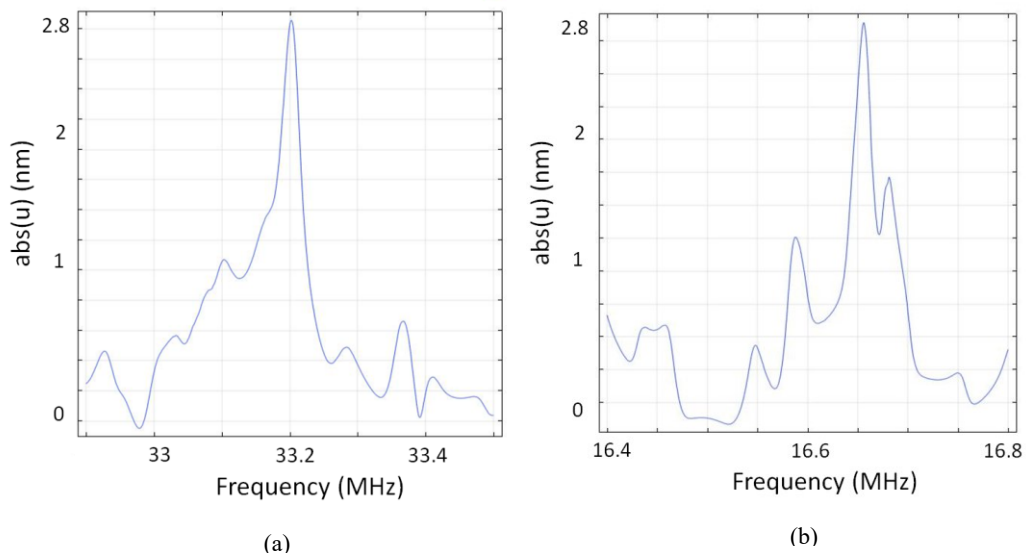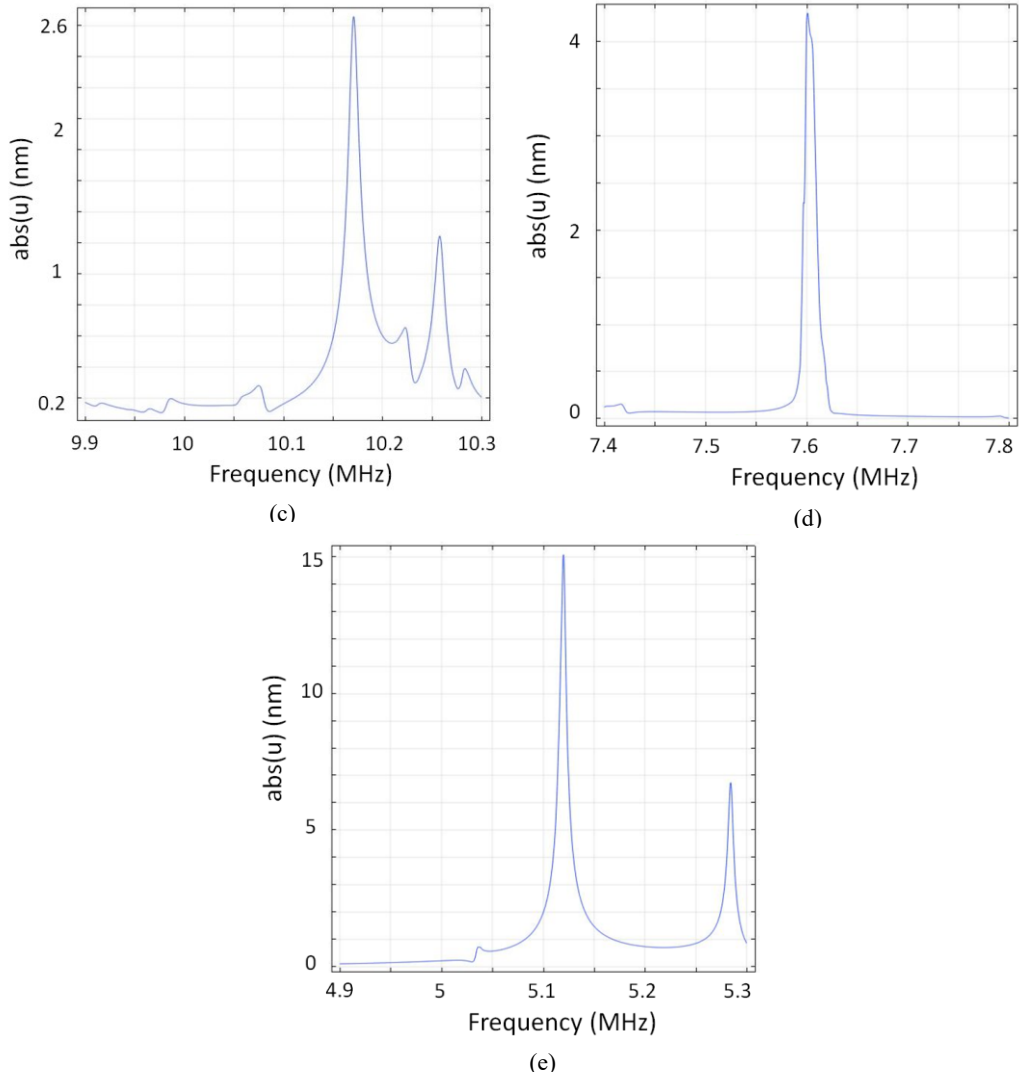
Fig. 4.7: COMSOL simulation results showing the resonant frequency characteristics to analyze the thickness of quartz crystal (a) 50μm (b) 100μm (c) 168μm (d) 215μm (e) 333μm.

Followed by the simulations, the results of the relationship between change in the thickness of the quartz and the change in the resonant frequency are plotted in the Figure 4.8. Figure 4.8 shows that the relationship is fairly linear, the resonant frequency shift is observed to be higher as the thickness of the quartz is reduced. The 5MHz and the 10MHz quartz crystal microbalance is the most employed category due to their robustness and stability. A thickness of quartz of 168μm and 333μm can provide this particular resonant frequency for the sensing device.
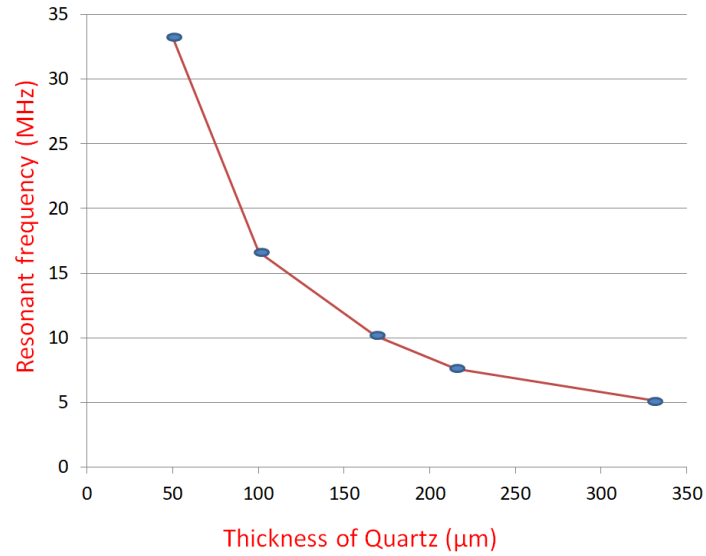
Fig. 4.8: COMSOL simulation results illustrating the relationship between the resonant frequency and the thickness of quartz (μm).

An accuracy rate of 99.99 % has been achieved between the variations in analytical modeling and the finite element analysis using the COMSOL software which is shown in the Table 4.2.

Table 4.2: Comparison between the theoretical and simulation resonant frequency for different values of thickness of quartz.

Thickness of quartz crystal (μm)	Theoretical resonant frequency (MHz)	Simulation resonant frequency (MHz)
50	33.2	33.2
100	16.66	16.651
168	10.17	10.17
215	7.6	7.6
333	5.12	5.12

4.3.4 Investigation of Radius of Quartz Crystal

As per the analytical modeling results and derivations, the radius of the quartz crystal does not have any significant effects on the output of the sensor with a conventional design. However, if this conventional design is altered, the output performance has the probability to vary. Thus in order to analyze the characteristics of this parameter, a parametric sweep is conducted in the COMSOL to observe any variations in the resonant frequency.

During the analysis of change in the radius of quartz crystal parameter, all other critical parameters such as the thickness of quartz and gold electrode and radius of gold electrode were kept constant in order to avoid any other possibilities for resonant frequency variations. Followed by setting all other parameters constant, a parametric sweep is done between 500μm to 12mm and the resonant frequency characteristic analysis is conducted and the results are plotted using a two dimensional graph in COMSOL and recorded resonant frequency variation results are shown in the Figure 4.9.

(a)

(b)
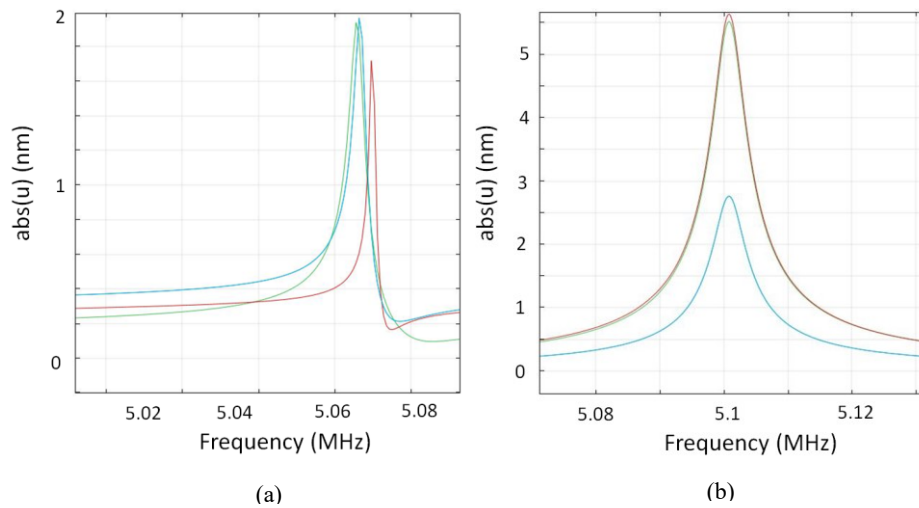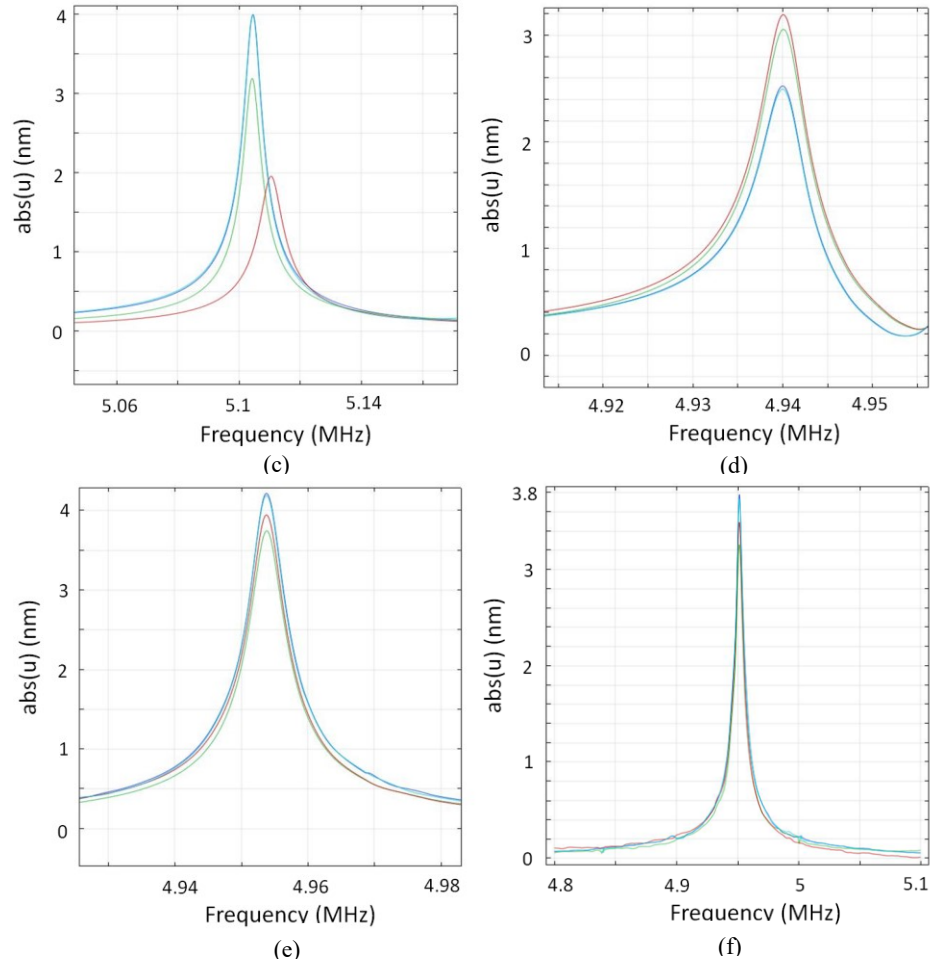
Fig. 4.9: COMSOL simulation results showing the resonant frequency characteristics to analyze the radius of quartz crystal (a) 500μm (b) 750μm (c) 1mm (d) 2mm (e) 3mm (f) 7mm.

Followed by obtaining the data, the resonant frequency on each radius of quartz crystal is plotted in a graph as shown in Figure 4.10. The results indicate that the resonant frequency varies with the variation in the radius of quartz dimensions. This variation is due to the fact that the vibration of the crystal during the TSM mode of oscillation travels through the quartz for up to a certain range depending on the size of the electrodes. For a 500μm radius of electrode, the vibrations travels up to 3mm and the resonant frequency stays stable beyond. These vibrations will affect the results of the quartz crystal microbalance sensor when it is designed in an array configuration [88]. In the case of a

conventional single channel QCM design, the variations can be neglected as it does not affect the final sensor output during sensing.
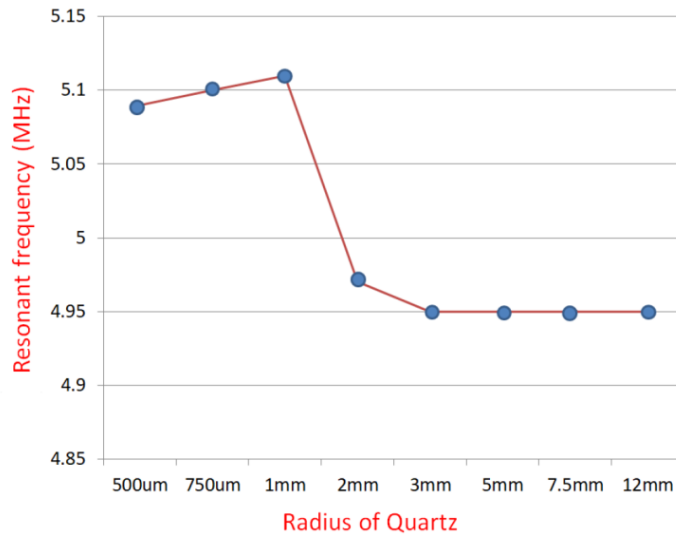
Fig. 4.10: COMSOL simulation results illustrating the relationship between the resonant frequency and the radius of quartz (μm).

4.3.5 Investigation of Thickness of Gold Electrode

The increment in the displacement of the quartz crystal microbalance can be correlated to the higher sensitivity. Therefore, in order to obtain a better sensitivity with the device, the effect of the electrodes dimensions needs to be assessed to analyze its role on the displacement characteristics [89]. To conduct test on the thickness of gold electrode characteristics, all other critical parameters are kept constant including the radius of quartz and gold electrode and the thickness of quartz crystal. Followed by this process defining the parameters, the adaptive frequency study is conducted and the mechanical response of the quartz for the applied potential is plotted in a two dimensional graph and shown in Figure 4.11.
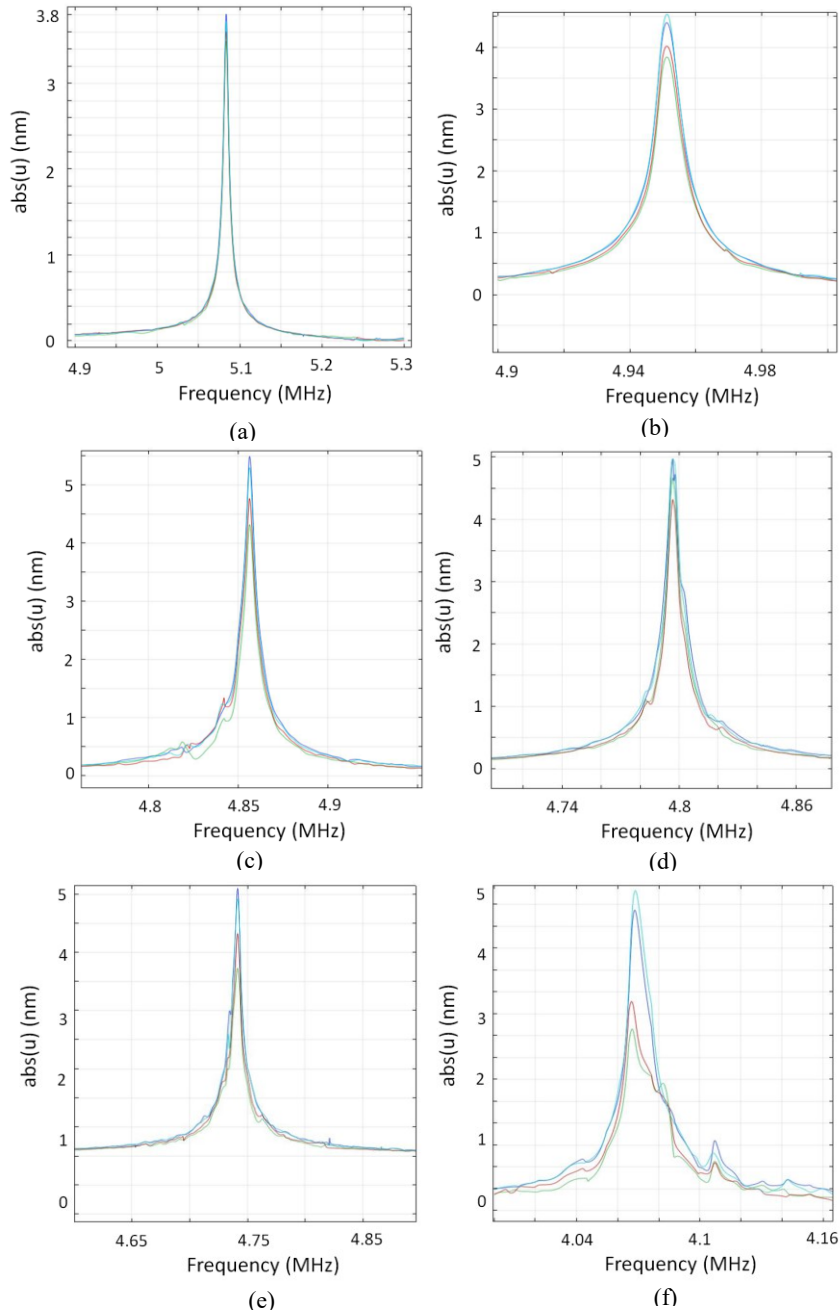
Fig. 4.11: COMSOL simulation results showing the resonant frequency characteristics to analyze the thickness of gold electrodes (a) 50nm (b) 200nm (c) 300nm (d) 400nm (e) 500nm (f) 1000nm.

The results indicate that the thickness of 300 nanometer of gold electrode exhibits higher displacement compared to the other thickness values. It exhibited a displacement of approximately 5.5 nanometers which can provide better output during the sensing process as shown in the Figure 4.12.
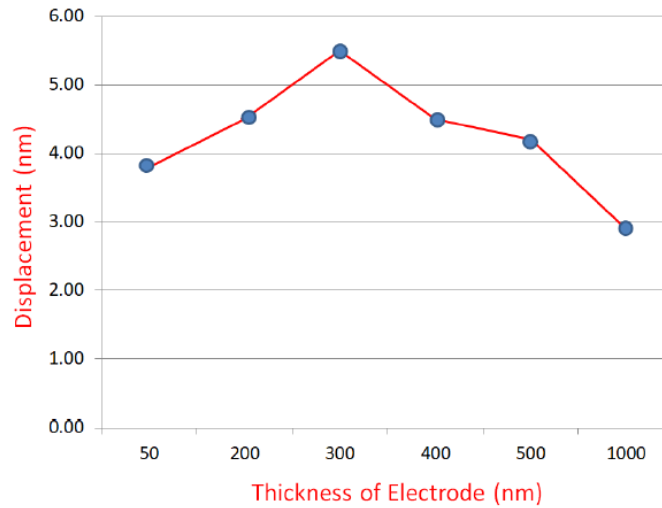
Fig. 4.12: COMSOL simulation results illustrating the relationship between the displacement and the thickness of gold electrode (nm).

4.3.6 Investigation of Radius of Gold Electrode

The radius of electrode is a significant parameter for the operation and performance of the sensing device. It serves as the active sensing area, where the target gas are prone to get interacted with the device and makes changes in the resonant frequencies which are further measured for the detection purpose. The radius of the electrode also plays a vital role in deciding the mass loading area. A higher mass loading area can provide a higher shift in the frequency due to the fact that the larger electrode size could provide more area for the interaction of the target gas with the sensor. In other words, a higher mass loading area could be platform for higher sensitivity [90]. Accordingly such a significant parameter is analyzed with finite element analysis tool to study its characteristics.

The finite element analysis is conducted by considering all other critical design parameters constant and the resonant frequency is calculated by conducting the adaptive frequency study and the results are shown in the Figure 4.13. The meshing conditions

were kept constant for all the electrode sizes and according re-meshed before each simulations.
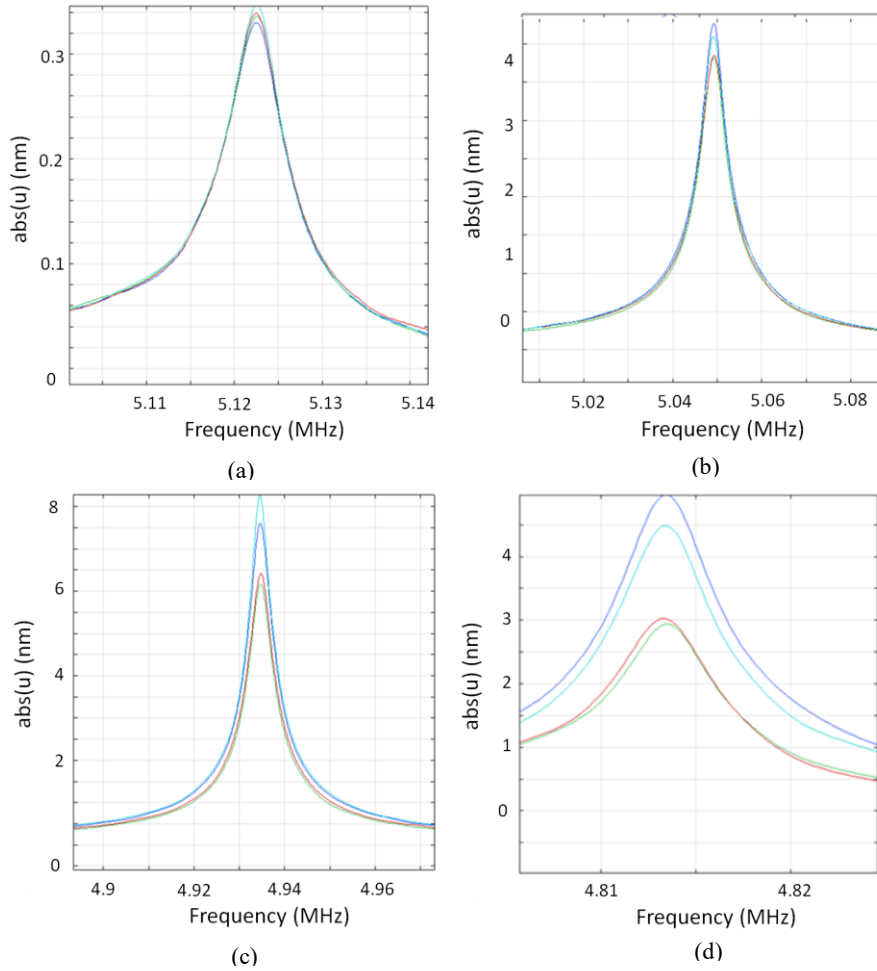
Fig. 4.13: COMSOL simulation results showing the resonant frequency characteristics to analyze the radius of gold electrodes (a) 100μm (b) 300μm (c) 1mm (d) 3mm.

As it can be seen from Figure 4.13, the results show that the smaller electrodes are exhibiting higher resonant frequency compared to the larger electrodes. This is due to the effect of the basic mass sensitivity of the quartz crystal microbalance. The variation in the resonant frequency is near linear and dependent on the fundamental resonant frequency of the sensor. In order to verify this dependency on the fundamental resonant frequency, the analysis is repeated with the quartz crystal microbalance of 10MHz range which

exhibited a higher response for the electrode mass compared to the 5MHz range as shown in the Figure 4.14 and 4.15.
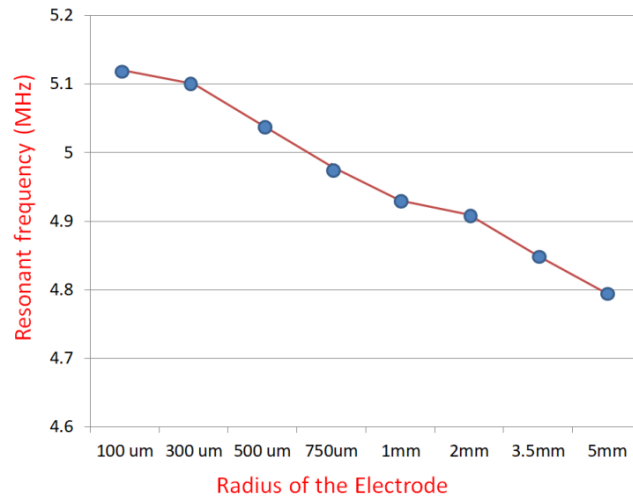
Fig. 4.14: COMSOL simulation results illustrating the relationship between the resonant frequency and the radius of gold electrode for the 5MHz range.
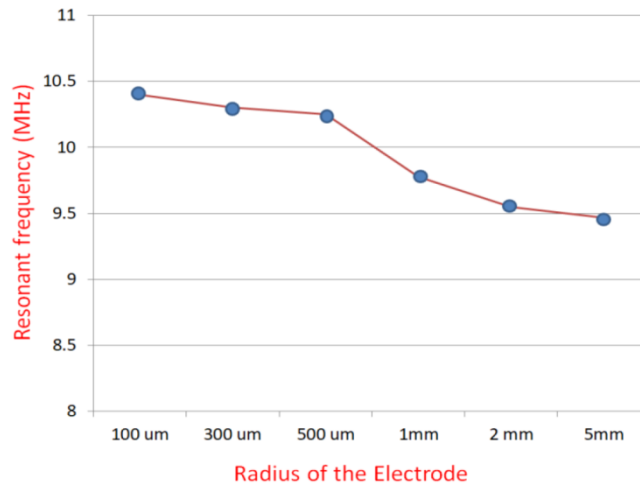
Fig. 4.15: COMSOL simulation results illustrating the relationship between the resonant frequency and the radius of gold electrode for the 10MHz range.

4.4 Conclusion

In this chapter the analytical modeling has been presented and the modeling results have shown the effects of thickness of quartz on the fundamental resonant frequency of the sensor and the relationship between the mass change frequency change

relationship. For the parameters where the analytical modeling cannot be applied due to the design complications, the finite element analysis has been employed. The accuracy of the simulations is ensured with the meshing characteristic analysis and a comparison between the theoretical calculations and the simulation results which exhibited a 99.99% accuracy rate. During the analysis of the radius of electrode in this chapter, it is been found that the sensitivity of the sensor is concentrated towards the center of the electrode. This phenomenon of higher sensitivity on the center of the electrode is analyzed further in the upcoming chapter to obtain an approximately uniform distribution of the sensitivity.

CHAPTER 5

ANALYSIS OF ELECTRODE STRUCTURES AND DISPLACEMENT PROFILE

– ELECTRODE DESIGN

5.1 Introduction

The structure and size of the electrode greatly influences the overall sensitivity of the quartz crystal microbalance sensor, which indeed provides possibilities for optimization and improvement of the sensitivity distribution over the surface of electrode [91]. The conventional quartz crystal microbalance sensor with the circular electrodes has its sensitivity concentrated towards the centre of the electrode. Energy trapping effect of the quartz is responsible for this accumulation of higher sensitivity towards the centre of the electrodes [92]. With this phenomenon of energy trapping, the conventional electrodes fail to utilize the complete potential of the sensing area, which in return degrade the device performance [93]. Moreover, due to this energy trapping effect, the circular electrodes are usually reduced in terms of size for better sensitivity by sacrificing the mass loading area on the electrode [94]. In this work, a proposed approach to address the drawbacks of these conventional sensors is to design a new electrode configuration that provides a high-performance and efficient electrodes. In this approach, there are possibilities of attaining high uniform sensitivity over the entire electrode surface irrespective of the sensitivity attained through fundamental resonant frequency. A quartz crystal microbalance sensor can be considered to be utilizing its full potential when it has a larger mass loading area on the electrode with high uniform sensitivity over the whole electrode. With configurations such as larger mass loading area and higher uniform sensitivity on the electrode, the sensor could be able to exhibit larger shift in the resonant

frequency when the target gas is absorbed on the sensing electrode. In order to achieve these qualities in the electrode, in this chapter, the finite element analysis and modelling are performed on several designs with various electrode structures and investigated. A novel design of electrode pattern called as the concentric electrodes has been further proposed, studied and compared with the conventional electrode.

5.2 Relationship between Electrode Structures and Mass Sensitivity

The mass sensitivity at a particular point of the electrode is directly proportional to the vibrational amplitude produced at that particular point of the electrode during the thickness shear mode of oscillation. In other words, the local mass sensitivity of the sensor depends on the local intensity of the inertial field developed on the crystal surface during crystal vibration, which is proportional to the vibrating amplitude in that particular point [95]. Thus, the displacement produced during the vibration can state the range of the sensitivity produced at the active sensing electrode. In the past decades, Sauerbrey's equation has been used to calculate the mass sensitivity of the quartz crystal microbalance sensor [96] but it fails to account the effect of electrode structure and type of metal used to calculate the sensitivity which results in inaccuracy for complex sensor array designs. The mass sensitivity of the quartz crystal microbalance can be described as a Gaussian curve across the active sensing electrode which can be described with the Bessel equation [97] which is derived as follows.

$$S_f(r,\Theta) = \frac{|A(r,\Theta)|^2}{2\pi \int_0^\infty r|A(r,\Theta)|^2 dr} \times C_f \tag{5.1}$$

where, $S_f(r,\Theta)$ is the mass sensitivity function with a unit of Hz/Kg, C_f is the Sauerbrey's sensitivity constant with a value of 1.78×10^{11} Hz. Cm^2 /kg. $A_f(r,\Theta)$ is the

particle displacement amplitude function and r is the distance from the centre. The particle displacement amplitude function A(r) is the solution of the following Bessel equation.

$$r^2 \frac{\partial^2 A}{\partial r^2} + r \frac{\partial A}{\partial r} + \frac{K_i^2 r^2}{N} A = 0 \tag{5.2}$$

where, N = 2.0443 according to the materials constant of the AT-cut quartz crystal, $K_i^2 = (\omega^2 - \omega_i^2)/c^2$, where i = E,P,U (E, P and U represents the full electrode region, partial electrode region and non-electrode region, respectively), $c = \sqrt{c_{66}/\rho_q}$ is the acoustic wave velocity in the crystal, where c_{66} is the elastic stiffness constant, ρ_q is the density of the quartz, ω_i is the cut off frequency of full electrode region ω_E, partial electrode region ω_P and non-electrode region ω_U [97]. On a 10 MHz quartz crystal microbalance, the mass sensitivity at r(0) of the electrode position has the highest sensitivity due to the energy trapping effect and it decreases exponentially with Gaussian curve when the distance from the centre increases [97]. In order to study and analysis the applications of these equations in conventional and proposed configuration in a complex array structure and to achieve a more uniform mass sensitivity across the electrode, the finite element analysis and modelling have been done using COMSOL Multiphysics simulation tool.

5.3 Finite Element Analysis on Various Electrodes

The objective of this finite element analysis is to achieve a more uniform distribution of sensitivity to achieve larger effective mass loading area comparative to the other conventional electrode of quartz crystal microbalance sensor.

5.3.1 Investigation of Conventional Circular Electrode

The conventional circular electrode has the advantage of easier fabrication process. However, the displacement is highly concentrated at the centre of the electrode, which limits the potential to react with all the target gas in an environment to achieve high detection capability.

In order to verify the Gaussian distribution of the sensitivity in the circular electrodes, the finite element analysis is conducted with an electrode radius of 4.25mm on a 12mm radius of quartz substrate. The fundamental resonant frequency of 5MHz range has been adopted to test the electrodes in this chapter. Commercially available quartz substrate with thickness of 333μm and resonant frequency of 5MHz has been used for all the analysis in this work. As previously investigated and identified, the meshing characteristics have been set to finer conditions to attain accurate results. The resonant frequency of the quartz crystal microbalance is studied by the adaptive frequency study performed between the range of 4.4 to 4.5 MHz in which the Eigen frequency is found to be 4.43MHz for the investigated design. Followed by this, the total displacement distribution on the electrode surface is plotted on a 2 dimensional plot. The results verified that the total displacement is distributed as a Gaussian curve as shown in the Figure 5.1 (b) and (c). From the displacement profile in Figure 5.1 (b), it can be seen that the total displacement is concentrated towards the inner area of the circular electrode which attained a displacement of 8nm compared to the outermost point on the electrode which attained a displacement of 1nm. Due to this peak variation in the displacement profile of the circular electrodes, the sensitivity varies from center part to the outer part of the electrode. Thus, the target gas which comes into contact with the 8nm displaced electrode point will have a much greater influence on the resonant frequency shift

compared to that of the area with 1nm displacement level. In order to balance this unequal distribution of the displacement profile, alternate electrode structure are proposed and analyzed.

(a)

(b)

(c)
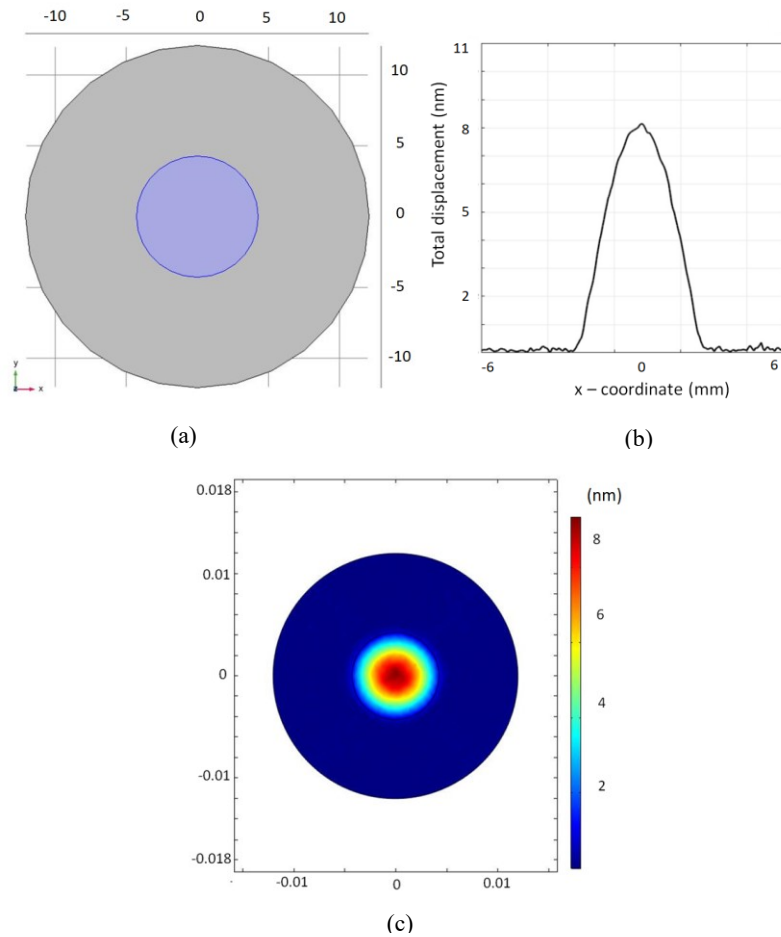
Fig. 5.1: Conventional circular electrode (a) Geometry - Radius of quartz (RQ) – 12mm, Radius of electrode (RE) – 4.25mm (b) Displacement profile along the electrode axis of RE – 4.25mm (c) 2D plot of displacement profile exhibiting Gaussian curve

5.3.2 Investigation of Ring Electrode

The ring electrodes are proposed as an alternative to the conventional circular electrodes. These electrodes are designed to indirectly cut and reduce the energy trapping effect by providing an approximately uniform sensitivity distribution on the surface of the electrode. Rings with various dimensions are analyzed to study their displacement

profile. The ring width of 2.125mm and 1mm with an overall radius of 4.125mm electrode has been modelled to have a better comparison with the latter electrode. The displacement profile is modelled and shown below in Figure 5.2.

<div align="center">(a)</div>

<div align="center">(b)</div>

<div align="center">(c)</div>

<div align="center">(d)</div>
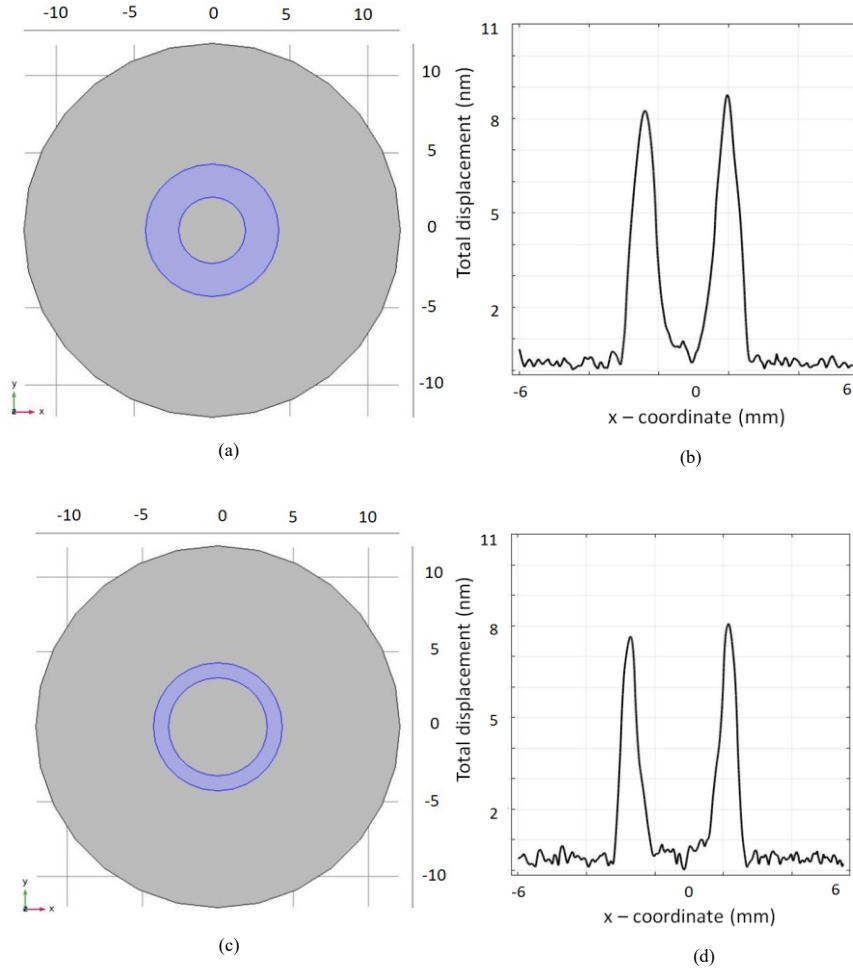
Fig. 5.2: Ring electrode (a) Geometry - Radius of quartz (RQ) – 12mm, Radius of electrode (RE) – 4.25mm, Ring width (RW) – 2.125mm (b) Displacement profile along the electrode axis with RW – 2.125mm (c) Geometry - Radius of quartz (RQ) – 12mm, Radius of electrode (RE) – 4.25mm, Ring width (RW) – 1mm (d) Displacement profile along the electrode axis with RW – 1mm.

The displacement profile of the 2.125mm ring width in Figure 5.2 (b), shows that the ring electrode structure has reduced the higher displacement in the centre of the electrode. The results further demonstrate that the energy trapping is comparatively

reduced than the circular electrodes in an indirect way. The displacement profile in the Figure 5.2 demonstrates 8nm displaced region around the outer part of the electrode while the centre part of the electrode provides 1nm displacement. Despite having a less mass loading area on the sensing surface compared to the circular electrodes, the ring electrodes exhibited better distribution of displacement.

5.3.3 Investigation of Ring Dot Electrode

The ring dot electrodes are designed as an improved version of the ring electrodes. Since the latter electrode's displacement profile has shown minimal displacement in the centre of the electrode, a dot in placed in this ring dot electrode to overcome the disadvantage. The ring dot electrode also has the comparative advantage of more mass loading area than the ring electrode with a potential improved distribution profile. The same ring width dimensions of 2.125mm and 1mm with a circle (dot) of 500μm in the middle of the electrode has been designed and analyzed for the displacement profile in order to compare them later.

(a)   (b)
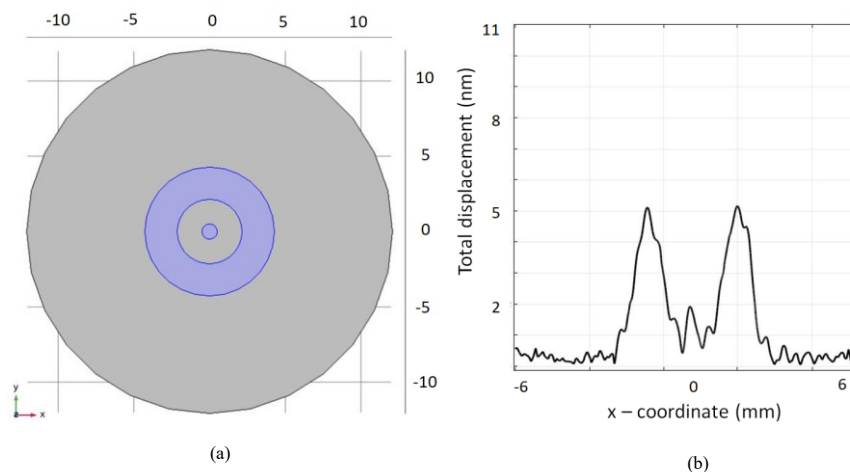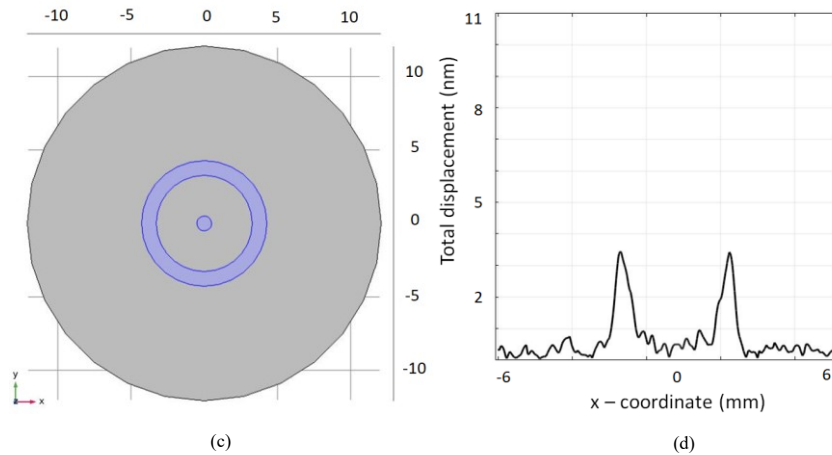
Fig. 5.3: Ring dot electrode (a) Geometry - Radius of quartz (RQ) – 12mm, Radius of electrode (RE) – 4.25mm, Ring width (RW) – 2.125mm with dot radius (RD) - 500μm (b) Displacement profile along the electrode axis with RW – 2.125mm (c) Geometry - Radius of quartz (RQ) – 12mm, Radius of electrode (RE) – 4.25mm, Ring width (RW) – 1mm with dot radius (RD) - 500μm (d) Displacement profile along the electrode axis with RW – 1mm.

The simulation results from Figure 5.3 show that the displacement profile of the ring dot electrode has provided a better distribution of the displacement compared to the ring electrodes because of the circular dot in the middle of the electrode. The circular structure in the middle region has contributed for the displacement in the middle region which has increased the displacement in the middle region of the electrode to 2nm. The ring dot width of 1mm provided better distribution compared to the 2.125mm ring dot electrode. Moreover, it also has extra surface area than the ring electrodes due to the circular structure of 500μm radius in the middle of the electrode

5.3.4 Comparison between Circular, Ring and Ring Dot Electrodes

In order to compare the various electrode's potential in the distribution of sensitivity or displacement, the displacement profile results for the similar overall electrode radius of 4.25mm are plotted using the MATLAB and shown in the Figure 5.4. The results indicate that the ring and ring dot electrode which are designed as an

alternative to the circular electrodes, have exhibited better distribution of the displacement along the axis of the electrodes. The electrode structures and dimensions contribute towards the distribution of displacement is wide range. The ring dot electrode has a variation in the displacement in the range of 3 – 5nm which along the electrode axis while the circular and the ring electrodes exhibited a variation in the range of 1 – 8nm and 2 - 8nm variation along the electrode axis. The ring electrode design provides a comparatively uniform displacement profile in the range of variation from 3 – 5nm. This means that the ring dot electrode structure has fairly even displacement profile. Thus, the ring dot electrode structure are concluded as a more suitable candidate for the uniform distribution of displacement comparative to the widely used conventional electrodes and further the ring dot electrode is further analyzed and improved.
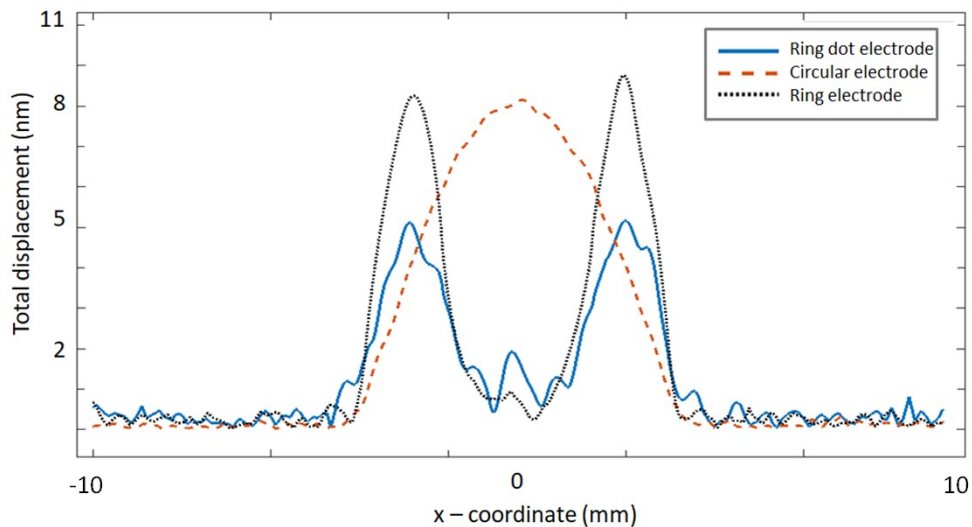
Fig. 5.4: Comparison of displacement profiles of circular, ring and ring dot electrodes.

5.4 Multiple Ring Design

Due to the factors such as the comparatively better uniform distribution in the displacement profile and higher mass loading area, the ring dot electrode is added with

multiple rings in order to improve the distribution and provide more area for mass loading. The multiple ring structure can provide the quartz crystal microbalance sensor electrode with higher area for the sensitive membrane and the target gas to react which in turn produces more shift in the frequency. Thus, an initial ring with similar ring width has been designed and studied as shown in the Figure 5.5 (a) and (b) which experienced a better distribution with higher surface area compared to the prior designs including the ring dot electrode. Dimensions of the following multiple ring design are listed in the Table 5.1.

Table 5.1: Dimensions of multiple rings with equal ring width and ascending ring width.

Multiple Rings	Equal Ring Width	Ascending Ring Width
Radius of quartz (RQ)	12mm	12mm
Radius of electrode (RE)	2.5mm	2.75mm
Ring width 1 (RW1)	500μm	500μm
Ring width 2 (RW2)	500μm	750μm
Dot radius (RD)	500μm	500μm

Furthermore, in order to extract the displacement from the centre of the electrode, on the next design as shown in Figure 5.5 (c) and (d), the outer rings are designed to be larger than the ring closer to the centre. In other words, the ring widths are designed in ascending order pattern in order to extract the displacement to the outer area of the sensing electrode. The results from the Figure 5.5 has demonstrated that the multiple rings in ascending ring width has delivers much better displacement profile compared to the previous designs, more rings are added and this ascending ring width pattern is studied and further analyzed as concentric electrodes in the upcoming section.
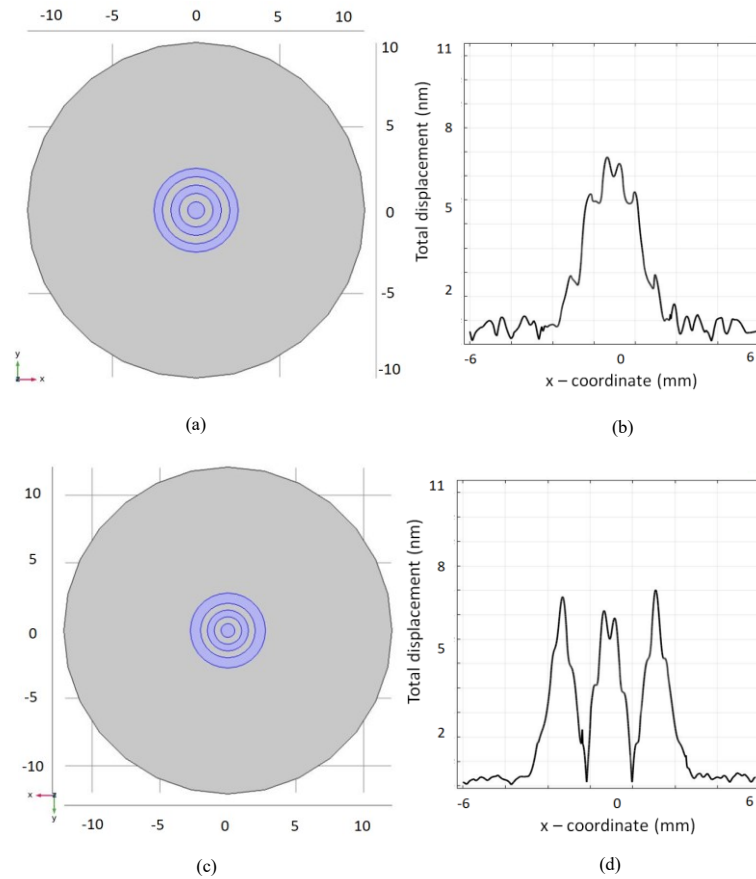
Fig. 5.5: Multiple ring electrode (a) Equal ring width (b) Displacement profile along the electrode axis with RE – 2.5mm (c) Ascending ring width (d) Displacement profile along the electrode axis with RE – 2.75mm.

5.5 Concentric Electrode Design

The concentric electrode structure is designed in a way that the adjacent rings are bigger than the previous rings in an ascending order pattern which enables a better distribution of the displacement across the electrode surface and thereby providing an approximately uniform sensitivity. These ascending rings encompasses the displacement in a way that it becomes approximately uniform despite providing a mass loading area almost equal to that of a circular electrode. Thus, due to its advantage of better even distribution of displacement and larger surface area for the target gas to react, it can

provides a higher level of shift in the frequency compared to all the previous electrodes which is the significant advantage of this electrode pattern in the QCM.

5.5.1 Design and Geometry

The rings are designed in a concentric pattern, in which the centre area is covered with a small 500µm circular electrode. The ring widths are set in ascending order in the ratio of 1:1.5:2. The gap is set constant with a constant dimension between the rings of 500µm. For example, if the radius of the centre circle is 500µm, then the rings width is in the order of 500µm, 750µm and 1mm which make the overall electrode size of 4.25mm with a constant gap between the adjacent structures of 500µm as shown in the Figure 5.6.
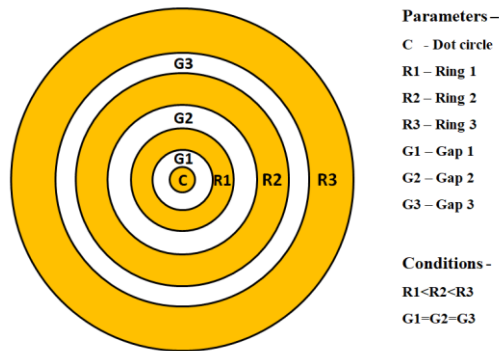
Fig. 5.6: Schematic illustration of the concentric circle electrode geometry with ascending ring width and equal gap.

5.5.2 Optimizing the Distribution Profile

A. Concentric Electrode with Increasing Ring Width

In order to study and analyze this ascending ring width pattern, various dimensions have been modelled to analyze the displacement profile. The ratios are set in the format of [Inner circle radius : Gap : Ring width 1 : Ring width 2 : Ring width 3]. Two ratios have been studied and analyzed for displacement profile as follows 1) ratio 1 – [1:1:1.5:2], 2) ratio 2 – [1:0.5:1:2:3]
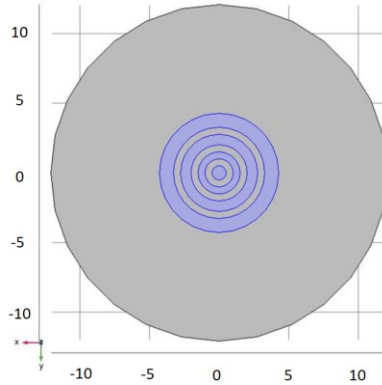
Fig. 5.7: Designed concentric circle electrode geometry with ascending ring width and equal gap with quartz substrate in COMSOL.

Initially, ratio 1 as shown in Figure 5.7 and 5.8 has been analyzed with C = 250μm and 500μm which provided a displacement pattern in which the distribution of the displacement from the outer to inner layer is contained between 2 – 3 nm. Then the ratio 2 set with the decreased gap to analyze the minimal gap required to sustain this uniform distribution. The results of the ratio 2 with C = 250μm and 500μm has shown lower distribution of displacement compared to the ratio 1. Thus the ratio 1 is adopted and analyzed further for different gap pattern in the upcoming section.

(a)

(b)

(c)

(d)
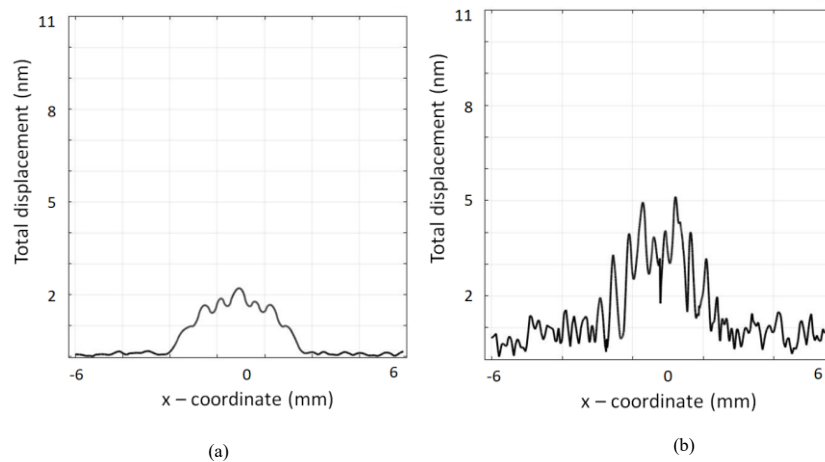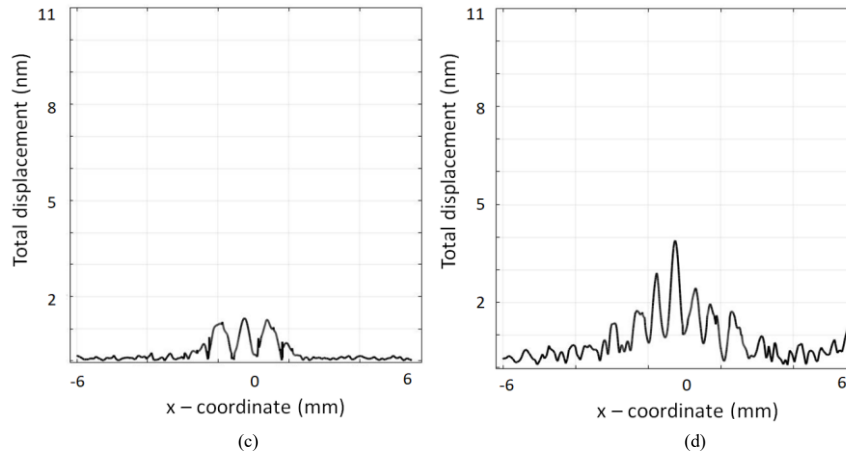
Fig. 5.8: Displacement profile of concentric electrodes (a) Ratio 1 [1:1:1.5:2] with C = 250μm (b) Ratio 1[1:1:1.5:2] with C = 500μm (c) Ratio 2 [1:0.5:1:2:3] with C = 250μm (d) Ratio 2 [1:0.5:1:2:3] with C = 500μm.

B. Concentric Electrode with Ascending Ring Width and Descending Gap

In order to further reduce the overall size of the electrode, in addition to the increasing ring width pattern, the gap parameters are designed in descending order from the centre instead of a constant gap as shown in Figure 5.9. Thus, in addition to the ratio of 1:1:1.5:2, the gap ratio from the centre has been set to 1:0.3:0.5 in the descending order. The inner smaller rings have a larger gap to its neighbouring structures compared to that of the outer larger rings.
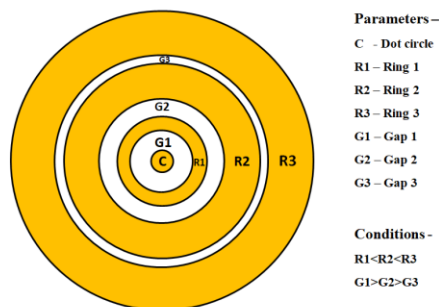
Fig. 5.9: Schematic illustration of the concentric circle electrode geometry with ascending ring width and descending gap.

67

The results as shown in the Figure 5.10 has given a much better distribution in the displacement profile with high overall electrode size of 4.25mm while providing the distribution within the average range of 2 – 4 nm variations across the axis of the electrode. The outermost point on the electrode has given a displacement of approximately 5nm compared to the 7nm in the centre of the electrode surface. Thus, the concentric electrode pattern can provide a more uniform sensitivity all over the electrode much better than its predecessors.

<div align="center">(a)   (b)</div>
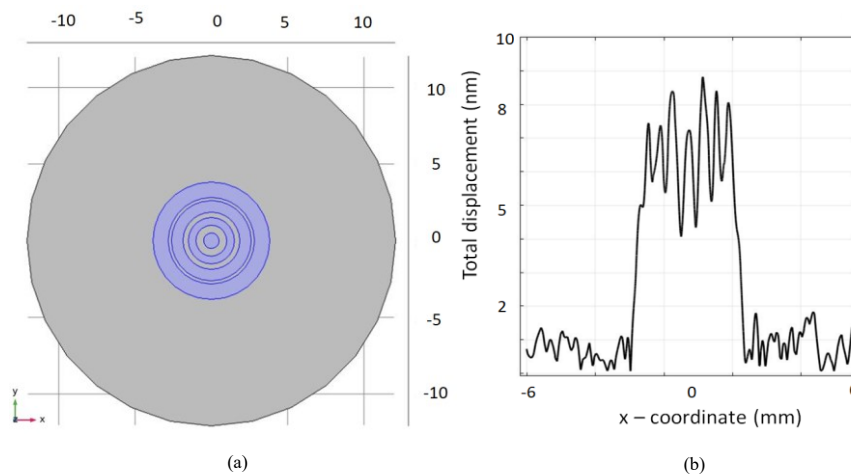
Fig. 5.10: Concentric electrode with ascending ring width and descending gap (a) Geometry - Radius of quartz (RQ) – 12mm, Radius of electrode (RE) – 4.25mm, Ring width 1 (RW1) – 500μm, RW2 - 750μm and RW3 – 1mm with dot radius (RD) - 500μm, Gap 1 (G1) - 500μm, G2 - 350μm, G3 - 200μm (b) Displacement profile along the electrode axis with RE – 3.8mm.

A comparison is made between the displacement profile of the final concentric electrode design and the initial conventional circular electrode in the Figure 5.11. The distribution profile ratios of the concentric electrode are fairly linear in the electrode region compared to the circular design while having the similar overall size of radius 4.25mm. It can be concluded that the concentric electrodes has provided a better uniform distribution of the total displacement across the axis of electrodes compared to the conventional electrode design.
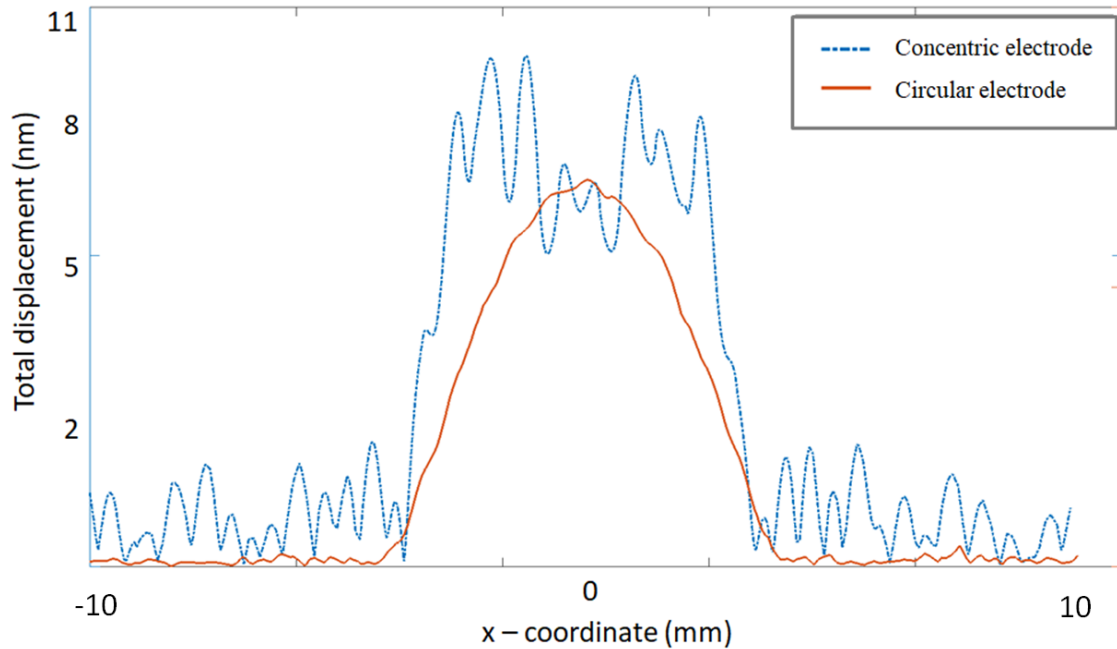
Fig. 5.11: Comparison of displacement profiles of conventional circular electrode and concentric electrode.

5.6 Conclusion

The displacement profile in the quartz crystal microbalance electrode is investigated and optimized to provide an enhanced uniformity of the displacement, which results in an improved sensitivity. The designed ascending ring width and descending gap pattern electrode has provided the highest uniform distribution without losing the surface area for interaction of the target gas. Moreover, the proposed concentric electrode design has similar dimension of a conventional circular electrode while providing an enhanced displacement performance. Furthermore these electrodes are deigned in an array configuration to enable the multiple target detection in the next chapter.

CHAPTER 6

MONOLITHIC MULTIPLE CHANNEL DESIGN – ARRAY CONFIGUARTION

6.1 Introduction

A multichannel quartz crystal microbalance (QCM) sensor, which is an array of QCM sensors is designed, simulated and analyzed in this chapter. Two types of arrays have been proposed in this chapter. The first design is the un-etched 5MHz QCM array that is developed with multiple concentric electrode channels where it still benefits from the simplified fabrication process without quartz etching process offered by advance micromachining techniques. The un-etched QCM array can be used only up to 5MHz range. If the resonant frequency is increased in the un-etched QCM array, the overall size of the array gets large which is the limitation of this un-etched QCM array. Therefore an alternate design called as the advanced high frequency etched QCM array has been proposed with 33.3MHz and 10MHz resonant frequencies which involves etching of the quartz for accommodating high resonant frequency operation within a small overall size for the miniaturized applications. It employs a dual inverted mesa structures on a monolithic quartz substrate to increase the frequency of the device without compromising the overall size. It has comparative advantages such as the high sensitivity due to high resonant frequency, smaller size and comparatively uniform distribution of displacement. Concentric electrodes are utilized in his design to overcome the disadvantage of high energy trapping of this design. Both the array designs has been investigated and analyzed for frequency interference between the channels and the minimal distance between the adjacent channels on the monolithic substrate without interference are further determined for each arrays.

6.2 Un-etched QCM Array – Multi Channel Design

6.2.1 Design and Frequency Interference

The un-etched QCM array design comprises of multiple electrodes on the same quartz substrate accompanied by their own pair of reference electrodes positioned on the bottom of the quartz substrate as shown in the Figure 6.1. This array structure is proposed by utilizing the previously proposed and designed concentric electrode configuration. Each electrode pair on the monolithic substrate acts as a channel. Every channel can operate as an independent QCM sensor and sense the target gas without any influence from the neighboring electrodes if they are placed at an optimal distance from each other in order to avoid the interference. This necessary optimal distance between the adjacent channels in the monolithic substrate ensures the absence of frequency interference between the adjacent channels [98]. In order to achieve this optimal distance, the electrodes are initially placed at the minimal distance to each other and then the distance is increased and the frequency interference pattern is investigated with the adaptive frequency study in COMSOL Multiphysics which is done in the following section. After optimization of the optimal distance, each QCM channel acts as an individual sensor utilizing the same quartz substrate [99]. In other words, a monolithic quartz crystal is utilized to operate multiple channels without interference. For instance, each QCM channels can be coated with different sensing materials and can be employed to detect a target gas in a complex environment using their measured unique patterns in the frequency shift [100].
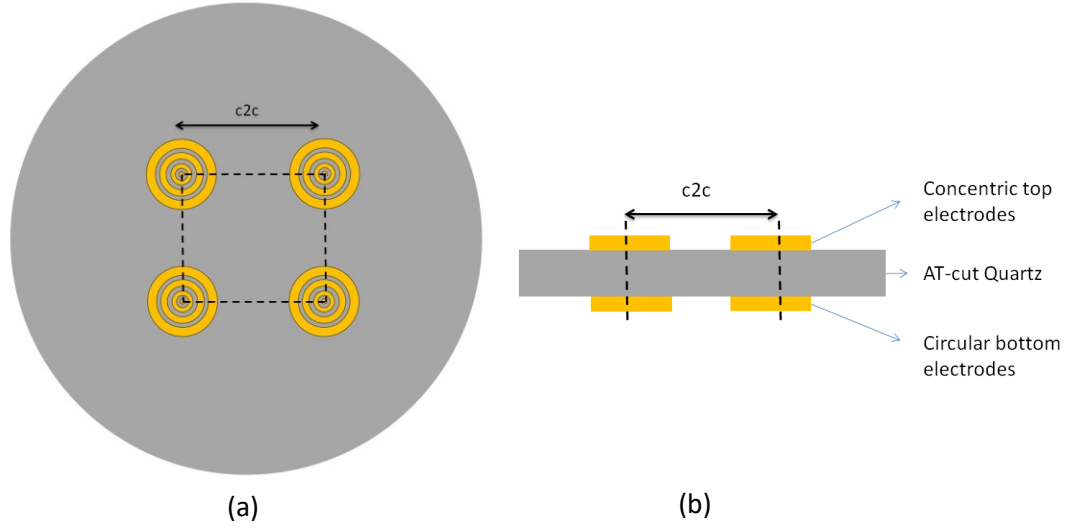
Fig. 6.1: Design of un-etched multichannel QCM design in which c2c is the distance between the center to center of adjacent electrodes (a) Top view showing four concentric electrodes (b) Side view of the un-etched QCM array.

6.2.2 Optimization and Elimination of the Frequency Interference

The optimal distance between the electrodes should preferably be as small as possible between the individual channels with the same resonant frequency across all the channels. The similar resonant frequency across the channels assures the absence of interference between the adjacent electrodes that is necessary for an accurate detection.

In order to find this optimal distance between the adjacent electrodes, the electrodes with constant dimensions of radius 500μm and thickness 300nm are placed as shown the Figure 6.2 with the center to center distance between the electrodes (c2c) started from 1.25mm and slowly increased up to 8mm with a step size of 1mm. The size of the quartz is kept constant with a radius of 12mm and a thickness of 333μm with a fundamental resonant frequency of 5MHz. Followed by this, the frequency study is conducted for each c2c value using the finite element modeling tools in order to find the resonant frequency of each individual channel. Finer meshing is utilized for this analysis. The resonant frequency characteristics of all the channels are analyzed in order to

monitor the interference. The results of this analysis are plotted in Figure 6.2 with the help of post processing tools, the resonant frequency across all the channels are investigated.

(a)   (b)
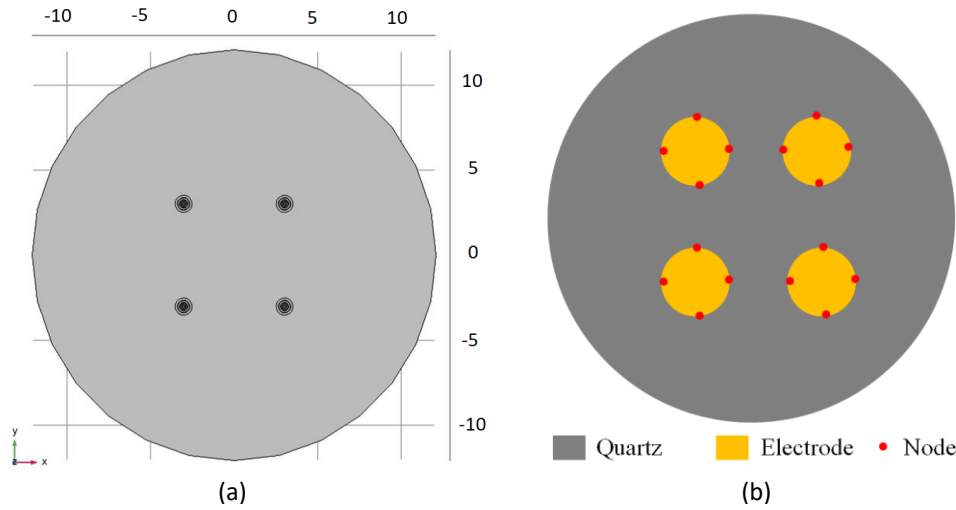
Fig. 6.2: Multichannel un-etched QCM design in COMSOL (a) Top view showing the four concentric electrodes (b) Node point pattern in COMSOL for the un-etched QCM design.

(a)   (b)
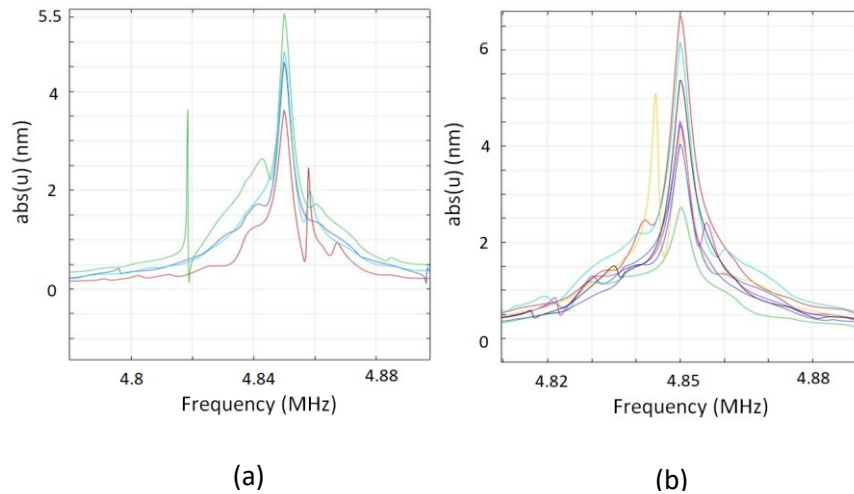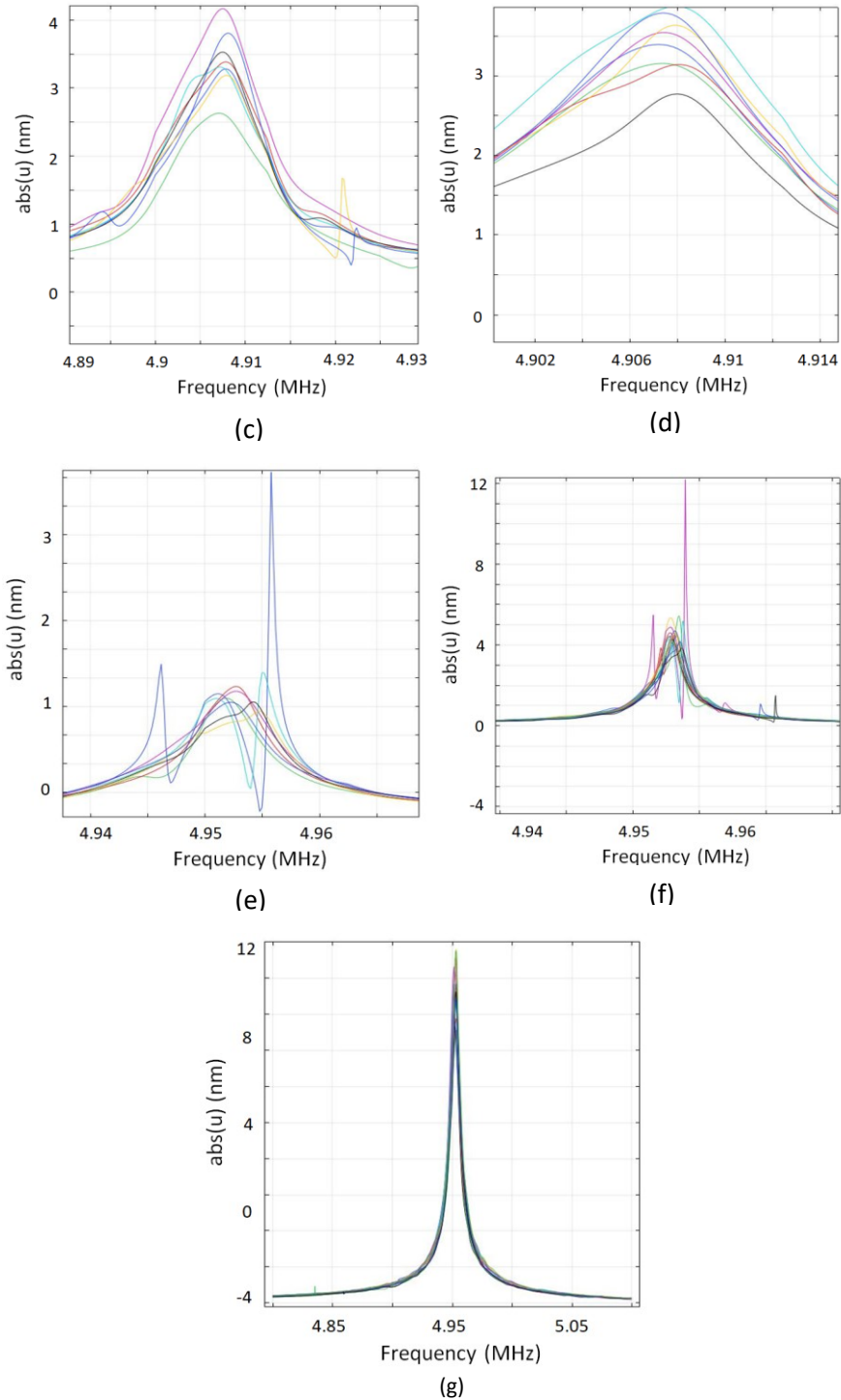
Fig. 6.3: COMSOL results showing the resonant frequency characteristics in order to analyze the frequency interference in un-etched QCM array for (a) c2c = 1.25mm, Electrode I, II (b) c2c = 1.25mm, Electrode III, IV (c) c2c = 2.5mm, Electrode I, II (d) c2c = 2.5mm, Electrode III, IV (e) c2c = 5mm, Electrode I, II (f) c2c = 5mm, Electrode III, IV (g) c2c = 6.5mm, Electrode I, II, III, IV.

The results of the resonant frequency analysis to monitor the interference between the four channels are shown in Figure 6.3 indicates that, for a c2c value of 1.25mm, the resonant frequencies of the electrodes are not similar across all the four electrodes. This is due to the fact that the displacement of a channel affects its neighboring adjacent electrode by causing disturbances in its thickness shear mode oscillation which further causes alterations in the frequency at which the electrode pair is oscillating. Therefore, it is concluded that the c2c distance of 1.25mm has frequency interference. Similarly the c2c values of 2.5mm, 5mm has frequency interference with the evident of varied resonant frequencies across the four electrodes as shown in the Figure 6.4. The c2c is further increased to 6.5mm from which the resonant frequency values across all the electrode pair or channels become equal. This equal resonant frequency values across all the channels indicate that the interference is totally eliminated and each of the electrode pairs or the channels operate as an individual QCM sensor with the ability to sense without any errors due to interference. The c2c distance above 6.5mm gives the similar zero interference. Thus, c2c of 6.5mm is chosen as the optimum distance between the center to center of electrodes for this proposed un-etched QCM array structure.
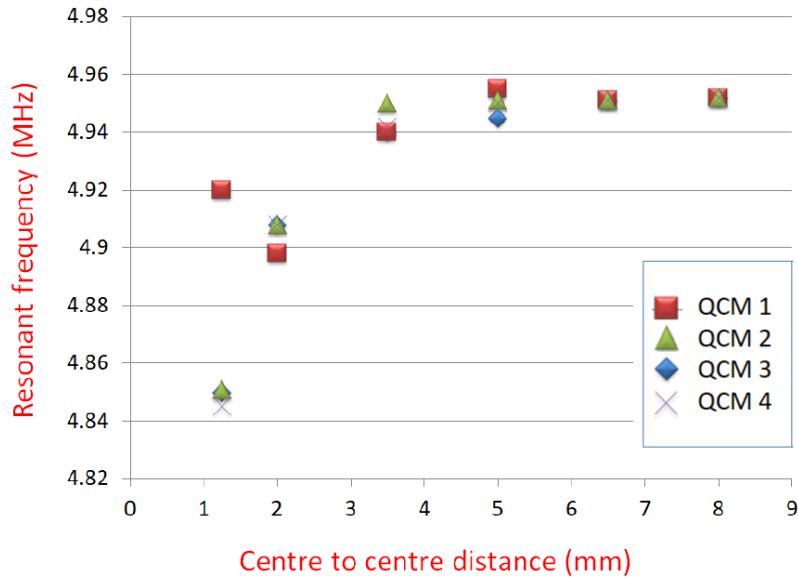
Fig. 6.4: COMSOL results illustrating the resonant frequency on all four un-etched QCM channels versus center to center (c2c) distance between the electrodes – c2c distance 6.5mm provides zero cross talk.

The designed four channel un-etched quartz crystal microbalance sensor with concentric electrodes has a fundamental resonant frequency of 5MHz. This proposed design has advantages such as the ease of fabrication, multiple target detection capability, approximately uniform distribution of electrodes with concentric electrodes and robust construction. Although it has its own advantages, the 5MHz frequency range can provide a limited range of sensitivity which may limit its performance due to the low resonant frequency.

Thus in order to increase the resonant frequency of the device for a further enhanced performance, the thickness of the quartz substrate needs to be reduced, which can increase the fragility of the substrate. If the resonant frequency is increased above 5MHz in this un-etched QCM design, the c2c distance will become larger to eliminate the interference, and ultimately increases the overall size of the sensor array. Thus, in order

to overcome this disadvantage an alternate high frequency QCM is proposed in the upcoming section which is designed with the aim of increasing the resonant frequency of the QCM above 5MHz without increasing the overall size of the array or even reducing the size than that of a 5MHz array.

6.3 Advanced High Frequency QCM Array

The advanced high frequency QCM is designed in the motive to overcome the limitations of the prior design such as the inability to operate at higher frequencies and large size between the adjacent channels if the resonant frequency is increased above 5MHz. This advanced high frequency QCM array can operate at high fundamental resonant frequency such as 10MHz and above with which a high mass sensitivity can be achieved during the operation. This advanced high frequency QCM design requires less area in the substrate for a channel compared to the conventional prior designed array due to the minimalistic design.

6.3.1 Proposed Design – Dual Inverted Mesa QCM with Concentric Electrodes

This proposed design consists of inverted mesa structures in the top and bottom of the quartz substrate as shown in the Figure 6.5. These two inverted mesa structures produce a thin quartz layer which is the vibrating area in the design with a thickness (VT) of 50µm in the quartz substrate. Thus, this thin quartz layer is naturally mount on the strong, thick walls of quartz as shown in the Figure 6.6, which are designed with the intent of providing them an independent area to oscillate without any cross talk from the adjacent channels and also to contain the displacement of a channel within its own zone [101]. The wall thickness is dependent on the center to center distance (c2c) of the adjacent electrodes. Furthermore, in order to electrically excite these thin quartz layers, a

77

concentric electrode is designed on the top of the vibrating thickness layer (VT) with a circular electrode on the bottom.

The vibrating layer thickness (VT) is six times the thickness of the actual quartz substrate. This high ratio of thickness difference of 6:1 ensures the stability and robustness to the overall structure of the device. If the VT is reduced beyond 50μm, the fragility of the device increases. Thus it is set to 50μm which has stability in the operation and providing a resonant frequency of 33.3MHz.
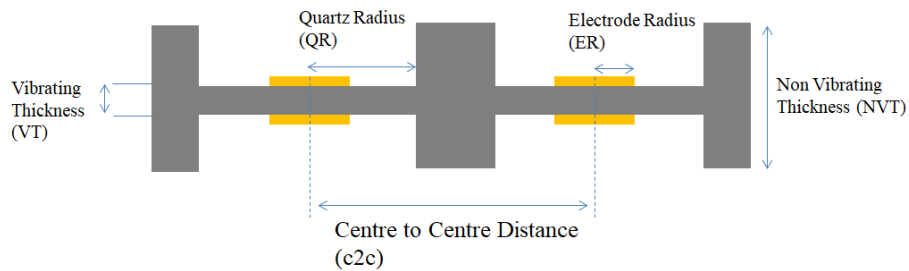
Fig. 6.5: Schematic illustration of the side view of dual inverted mesa QCM with concentric electrodes showing the significant parameters.
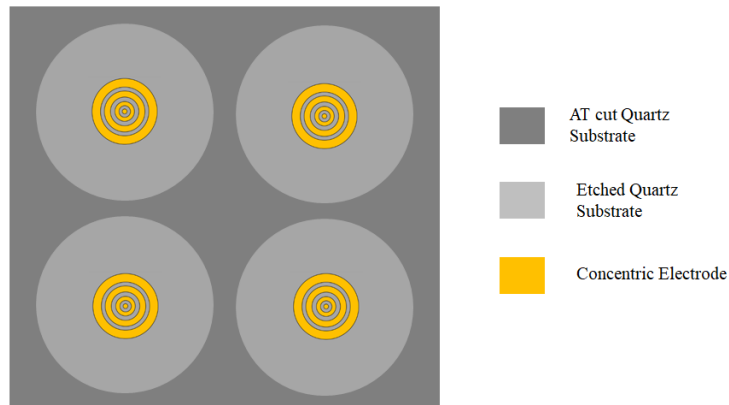
Fig. 6.6: Schematic illustration of the top view of dual inverted mesa QCM with concentric electrodes array showing the etched portions of the quartz substrate with the concentric electrodes.

When the alternating electric current is applied on these electrodes, the thin quartz layer with the thickness of the 50μm starts to oscillate at a fundamental frequency of 33.3MHz and the oscillating frequency decreases when the target gas comes into contact which forms the working principle of this design. The width of the wall, thickness of the non-vibrating substrate (NVT), center to center distance between the electrodes (c2c), quartz radius (QR) are the significant parameters in this design which majorly contribute in the process of eliminating the frequency interference and they are optimized in the upcoming sections.

6.3.2 Comparative Advantages and Disadvantages

The dual inverted mesa QCM with concentric electrode design has several advantages over the conventional QCM array such as:

1. High resonant frequency operation which provides a high mass sensitivity [102]. Most of the conventional QCMs designs operate between 5MHz and 10MHz zone but each channel in the dual inverted mesa QCM can operate at a fundamental frequency of about 33.3MHz.

2. Comparatively small size of array due to the advanced dual inverted mesa design which can trap the displacements within the zone of vibration. In conventional QCMs, the c2c distance is larger which results in a comparatively large size of the array.

3. High durability of the array due to the fact that they are supported and mounted by the thick walls of quartz. On the contrary, if the conventional QCMs are designed to operate at higher resonant frequency of 33.3MHz, the device becomes fragile due to the complex mounting needs for a thin substrate (50μm).

4. Concentric electrodes in this design provide an approximately uniform mass sensitivity across the electrodes during the high frequency operation which enhances the performance of the sensor furthermore.

Despite such peculiar advantages, this dual inverted mesa QCM has some amendable disadvantages such as:

1. High energy trapping effect due to the strong natural mount of the thin vibrating quartz layer which increases and accumulates the sensitivity in the center of the electrodes [103]. However, with the leverage of concentric electrodes, as discussed in the previous chapter, the energy trapping effect can be eliminated.

2. Due to the high resonant frequency, there are high chances of cross talk in the channels, if the critical design parameters of the sensor array are not fully investigated [103]. Thus, the critical design parameters to eliminate the frequency interference are analyzed and optimized in the upcoming section.

6.3.3 Optimization and Elimination of the Frequency Interference

The critical design parameters of the array need to be investigated in order to eliminate the frequency interference between the adjacent channels and to minimize the channel size. Initially, for an electrode radius of 500μm, the vibrating area size (RQ) is optimized in order to obtain a clear thickness shear mode oscillation with a minimum size. This investigation is done on a single channel high frequency QCM.

Then, the thickness of the non-vibrating area (NVT) is varied and the suitable center to center distance between the electrodes (c2c) for each NVT is studied and investigated. For this cross talk investigation, two channel high frequency QCM array is employed. If the frequency interference is eliminated in between these two channels, then

the same dimensions can be used to fabricate a high number of channels on a monolithic quartz substrate.

6.3.3.1 Vibrating Area – Radius of Quartz (RQ)

In the process of minimizing the size of the array, the size of the vibrating area needs to be adjusted in such a way that it provides a fine thickness shear mode oscillation at a minimum radius of quartz (RQ). This is the region which undergoes the thickness shear mode oscillation on the application of alternating electric potential with the electrodes. This region has a thickness of about 50μm which provides a high resonant frequency of about 33.3MHz. Finite element analysis has been utilized in order to investigate its effect on the oscillation. This analysis is carried out on a single channel. With a fixed electrode radius of (ER) 500μm, the radius of quartz is increased up to 2mm with a step size of 1mm and the resonant frequency characteristics are obtained using the frequency study in the finite element modeling tools. The node point pattern for the resonant frequency analysis in COMSOL to analyze the TSM mode is shown in the Figure 6.7. The resonant frequency analysis for various RQ values are simulated and the results are plotted using the post processing tools and are shown in the Figure 6.8.
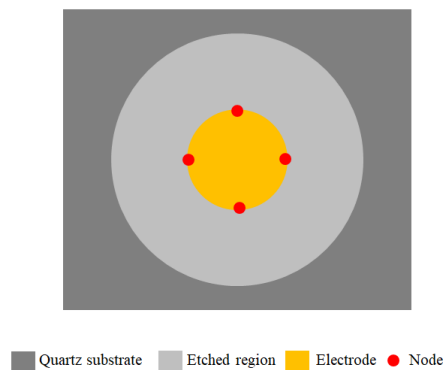
Fig. 6.7: Node point pattern in COMSOL for a single channel high frequency dual inverted mesa QCM design.
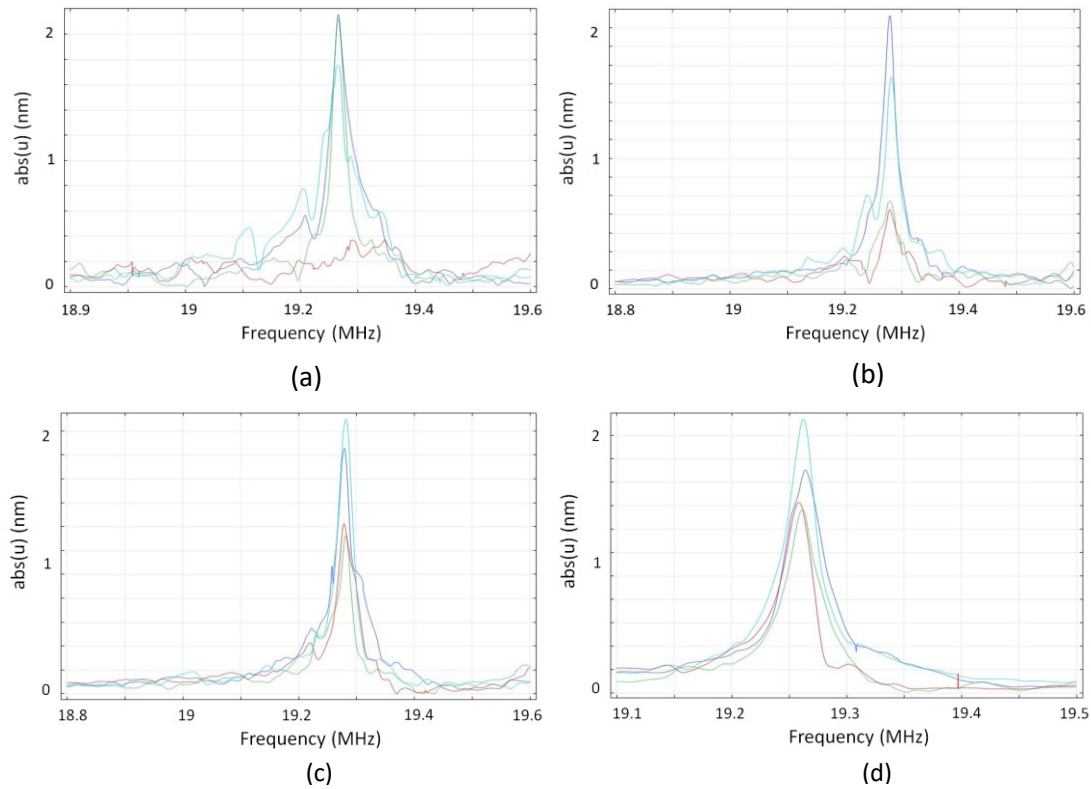
Fig. 6.8: COMSOL simulation results showing the resonant frequency characteristics for various radius of quartz (RQ) (a) RQ = 0.75mm (b) RQ = 1mm (c) RQ = 1.5mm (d) RQ = 2mm.

The results indicate that the resonant frequencies are varying below RQ = 2mm, while the resonant frequencies are getting constant from RQ = 2mm. The unstable resonant frequencies below RQ = 2mm is due to the insufficient area for thickness shear mode oscillation. The insufficient vibrating area produces a stress in the thickness shear mode oscillation from the boundaries which causes the resonant frequency to vary. When the RQ is 2mm or higher, the area to undergo thickness shear mode oscillation is sufficient without any barrier to cause stress and the resonant frequency remains constant as shown in Figure 6.9. Thus the RQ value of 2mm which is the minimum value at which the resonant frequency becomes constant and it is chosen for the further upcoming interference test in the array with multiple channels.
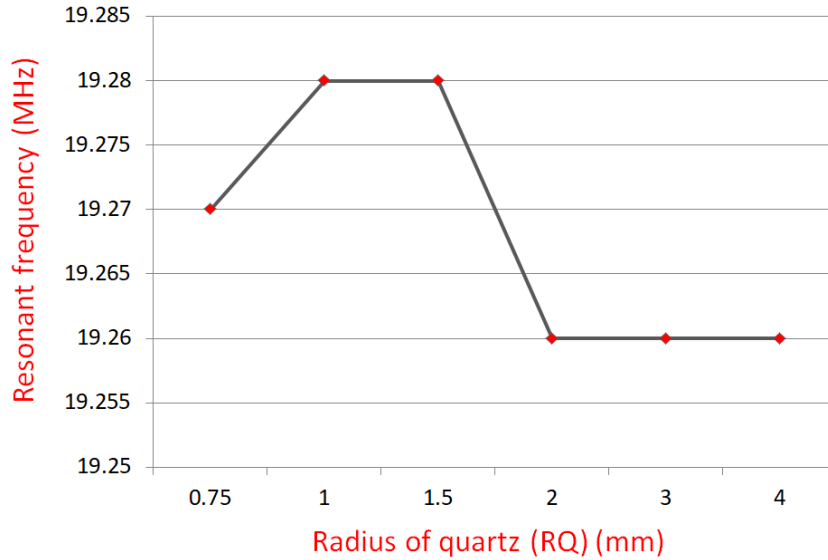
Fig. 6.9: COMSOL simulation results illustrating the characteristics of resonant frequency versus the radius of quartz (RQ) in which RQ is observed to be constant from 2mm.

6.3.3.2 Non-Vibrating Thickness (NVT) and Center to Center Distance (c2c)

A. For Vibrating Thickness (VT = 50μm) with a Resonant Frequency of 33.3 MHz

In order to test the interference between neighboring channels in the array, a high frequency 33.3MHz QCM array with two channels are considered. By eliminating interference between the two channels, the same array can be replicated with the similar dimensions on a large scale substrate with multiple channels. The electrode radius of 500μm and a quartz radius of 2mm for each channel are fixed from the previous investigations. The vibrating thickness (VT) is kept constant as 50μm which has a fundamental resonant frequency of 33.3MHz. There are two critical design parameters in the design that needs investigations in order to eliminate frequency interference between the channels. They are the non-vibrating thickness (NVT) and the center to center distance between the electrodes (c2c). The non-vibrating thickness (NVT) is the measure of the actual quartz substrate without the inverted mesa structures and the center to center

distance between the electrodes (c2c) is the parameter that decides the distance between the adjacent channels and the width of the quartz wall separating the neighboring adjacent channels. To eliminate frequency interference between the two high frequency QCM channels, the non-vibrating thickness (NVT) is kept constant for each iteration and the frequency interference is investigated with the different value of center to center distance (c2c) starting with the minimum c2c value. The most common quartz wafer thicknesses available are 333μm and 168μm.

For instance, the NVT is considered 168μm on the first iteration followed by the second iteration with 333μm. The c2c is increased starting from 4.5mm and increased up to 20mm with a step size of 2mm till it reaches zero interference. The resonant frequency analysis is initiated with c2c = 4.5mm because if it is reduced below 4mm, the vibrating zones of the two adjacent channels will overlap. The node point pattern for the resonant frequency analysis in COMSOL to analyze the interference is shown in the Figure 6.10. The resonant frequencies characteristics are studied in order to analyze the interference pattern for the two iterations with different c2c values using the finite element modeling tools and the results are plotted as shown in the Figure 6.11.
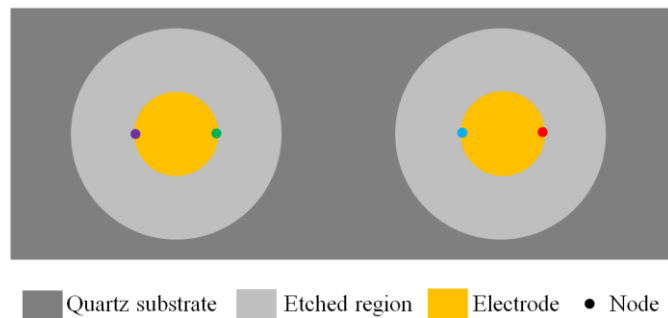
Fig. 6.10: Node point pattern in COMSOL for the two channel high frequency dual inverted mesa QCM design.

When NVT = 168μm, the c2c is increased starting from 4.5 to 20mm with the step size of 2mm.
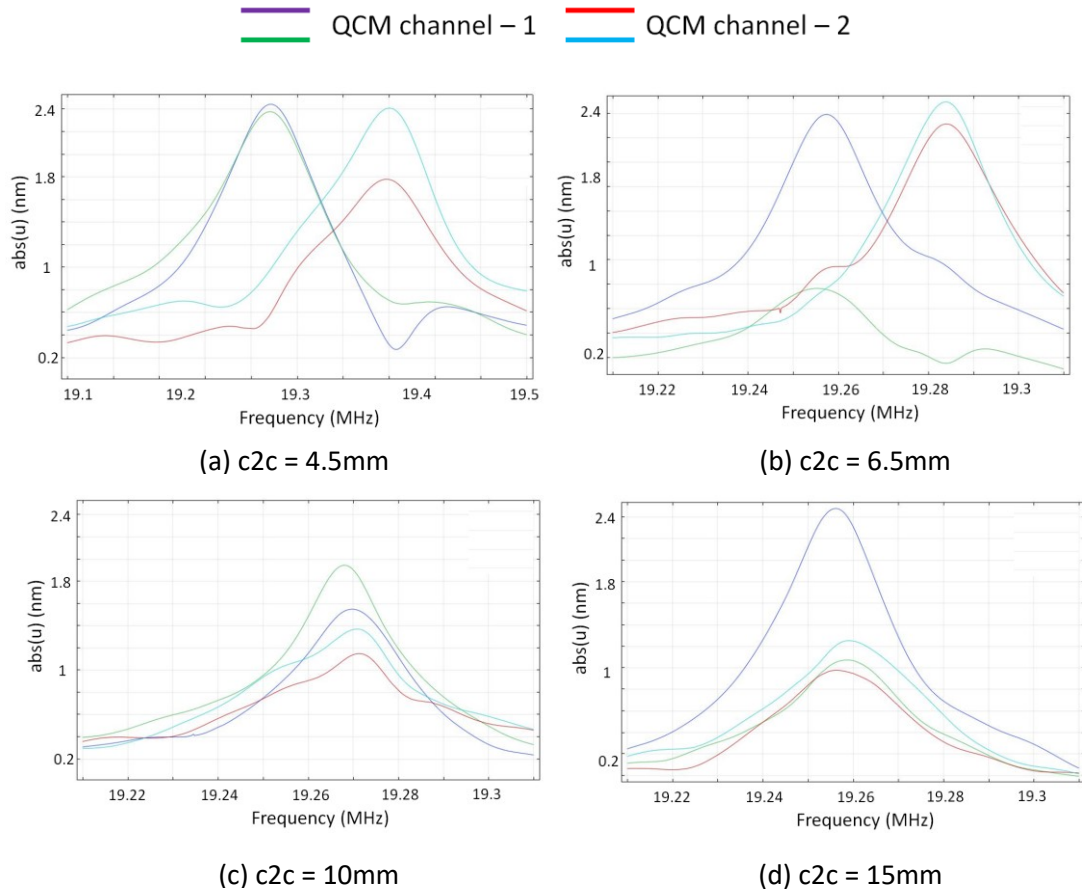
Fig. 6.11: COMSOL results showing the resonant frequency plot of the two 33.3MHz frequency channels which indicates the level of interference for various c2c values with NVT = 168μm. (a) c2c = 4.5mm (b) 6.5mm (c) 10mm (d) 15mm.

The simulation results of the analysis indicate that the frequency interference gradually decreases when the c2c is increased and finally attains the zero interference state when c2c = 15mm for NVT of 168μm. The results also state that the c2c value needs to be large enough for a given NVT value in order to attain the zero interference state. Similarly, the interference analyzes between the two high frequency QCM channels are conducted for NVT = 333μm.

When NVT = 333μm, the c2c is increased starting from 4.5mm to 20mm with the step size of 2mm and the resonant frequency characteristics to analyze the interference are plotted in the Figure 6.12.
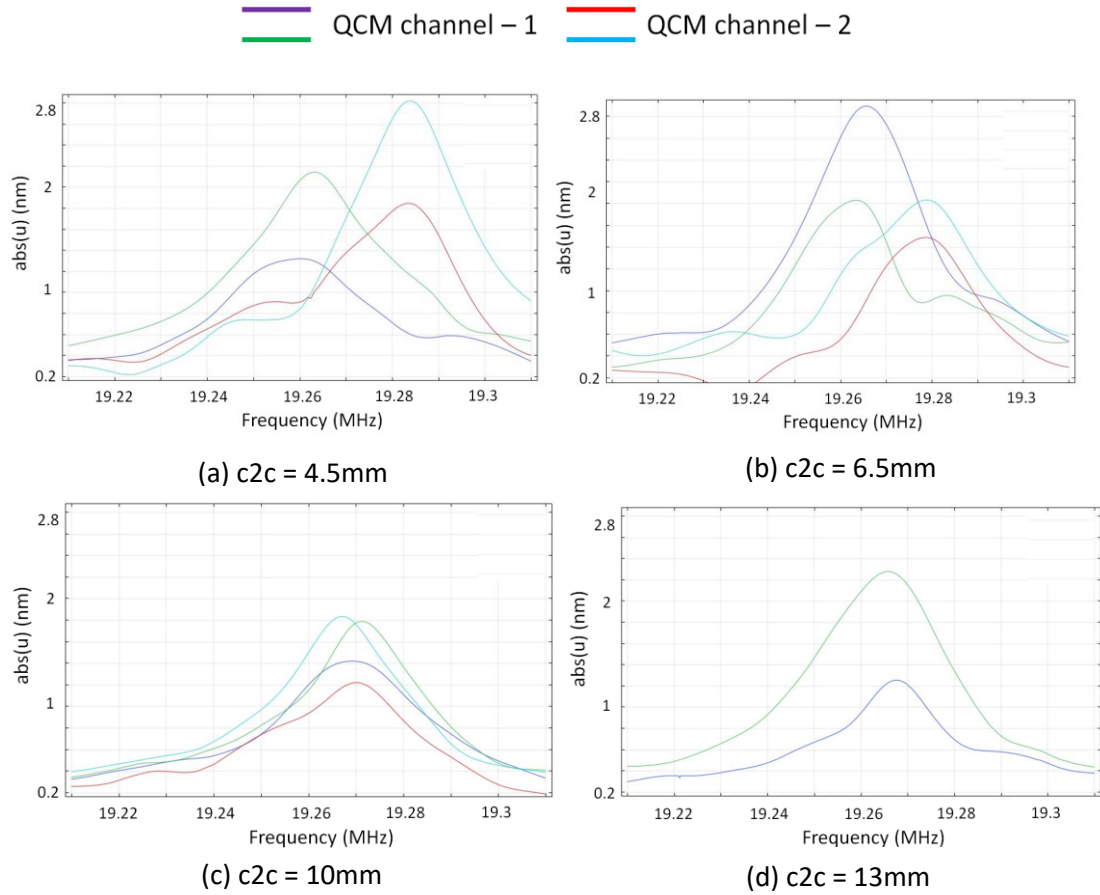
Fig. 6.12: COMSOL results showing the resonant frequency plot of the two 33.3MHz frequency channels which indicates the level of interference for various c2c values with NVT = 333μm. (a) 4.5mm (b) 6.5mm (c) 10mm (d) 13mm.

The resonant frequency analysis is done in order to monitor the interference between the channels and the results are shown in Figure 6.10 indicate that the frequency interference slowly decreases when the c2c is increased and is eliminated when c2c is 13mm. A higher quartz substrate thickness reduces the distance between the electrodes and provides a zero interference state. Thus, the NVT and c2c are directly proportional to each other to eliminate interference zone. If the NVT is large, the zero-interference zone

can be obtained with a smaller value of c2c compared to that of a small NVT value. Thus if the non-vibrating thickness (NVT) is large, then the c2c value gets comparatively small.

The c2c value on an array also depends on the fundamental resonant frequency of the vibrating quartz plane. Due to the high resonant frequency of 33.3MHz with VT = 50μm, the zero resonant frequency state has been achieved at 15mm and 13mm for the substrate thickness (NVT) of 168μm and 333μm. This is due to the fact that oscillation of high frequency quartz produces more displacement than a less frequency quartz. In order to prove this, the same analysis has been carried out on a 10MHz array with the same design which should provide a comparatively small c2c value than 33.3MHz array.

B. For Vibrating Thickness (VT = 168μm) with a Resonant Frequency of 10 MHz

The frequency interference analysis has been repeated with the dimensions similar to that of the 33.3 MHz except for the vibrating thickness (VT) of 168μm in order to attain 10MHz. The substrate thickness (NVT) of 333μm is chosen for the analysis and the finite element analysis is conducted and the results are shown below in the Figure 6.13. When NVT = 333μm, the c2c is increased starting from 4.5mm to 10mm with the step size of 0.5mm.

(a) c2c = 4.5mm   (b) c2c = 5.5mm

(c) c2c = 6mm
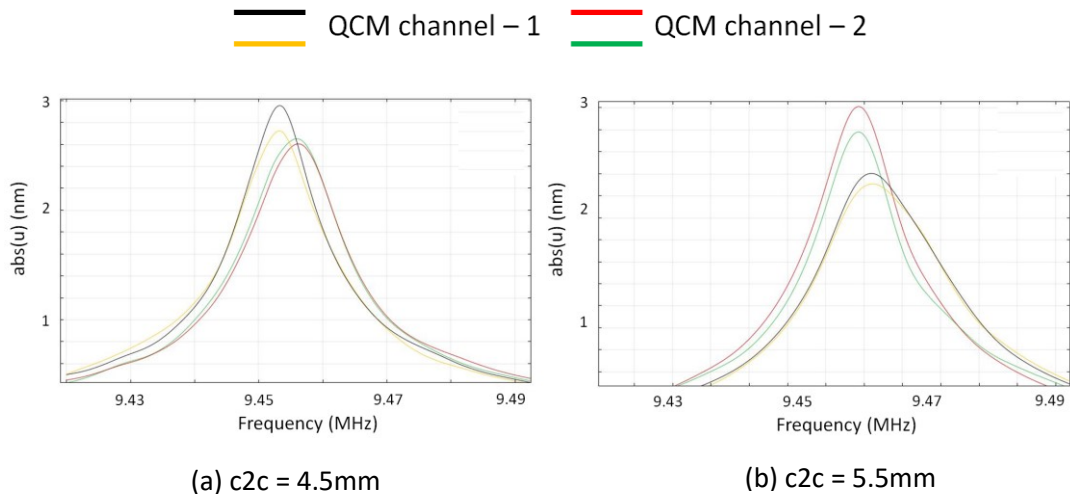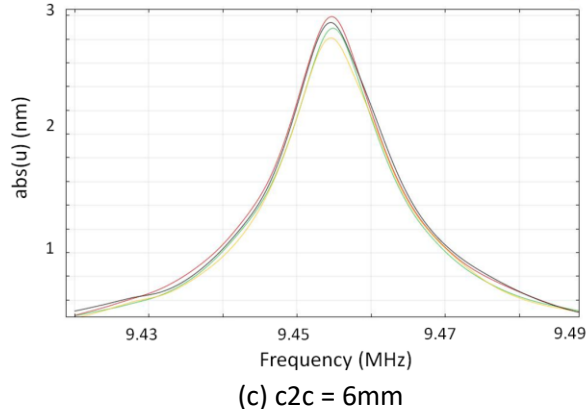
Fig. 6.13: COMSOL results showing the resonant frequency plot of the two 10MHz frequency channels which indicates the level of interference for various c2c values with NVT = 333μm. (a) 4.5mm (b) 5.5mm (c) 6mm.

The results indicate that the frequency interference between the 10MHz channels in the array are slowly decreasing from c2c = 4.5mm and has been completely removed from c2c value of 6mm. Thus compared to 33.3 MHz array, the c2c value in the 10MHz is smaller.

Furthermore, with this 10MHz dual inverted mesa design QCM array, c2c value of 6mm achieved which is lower than the c2c value of 6.5mm achieved on the conventional non-etched 5MHz QCM array. With this dual inverted mesa QCM design, the array size has been made smaller although the fundamental resonant frequencies of the QCM channels are increased.

6.4 Conclusion

Two types of QCM arrays has been proposed in this chapter. The initial fundamental QCM array is a monolithic multiple channel design with a resonant frequency of 5MHz without altering the structure of the quartz substrate. The un-etched QCM array has achieved zero frequency interference at a c2c value of 6.5mm. Followed by this, the second type of QCM array is proposed which is an advanced high frequency

multiple channel QCM with a resonant frequency of 33.3MHz and 10MHz. These design involved alterations in the structure of the quartz with the dual inverted mesa design. The frequency interference has been eliminated between the multiple channels in the etched monolithic quartz array and the size of the array has been reduced than the lower 5MHz array design despite being equipped with high resonant frequencies of 33.3MHz and 10MHz. The concentric electrodes in these advanced high resonant frequency arrays will increase the performance in terms of uniform distribution of the displacement as discussed in the previous chapter. The fabrication procedure of this advanced high frequency QCM array will be discussed in the next chapter.

CHAPTER 7

PROPOSED FABRICATION PROCEDURE

7.1 Introduction

The procedure for the micro and nano fabrication of the multichannel dual inverted quartz crystal microbalance sensor is proposed and discussed in this chapter. The quartz crystal microbalance sensor benefits from a noncomplex micromachined fabrication process compared to most of the other gas sensors in its range such as the metal oxide semiconductor sensor, surface acoustic wave sensor, and optical sensor [104]. This is due to the advantage of absence of complex structures or other assisting operational units such as the temperature stabilizing micro heater. The simple structure of the quartz crystal microbalance sensor contributes to the low cost manufacturing and fabrication of the device [105]. The fabrication process is discussed for four channels in this chapter but based on the size of the substrate, the number of channels in the array can be increased accordingly which is explained furthermore in this chapter.

7.2 Developed Fabrication Process Steps

The fabrication procedure of the dual inverted mesa QCM array with a fundamental resonant frequency of 33.3MHz has been proposed further.

A. Cleaning the substrate

The initial step of the fabrication process is the cleaning of AT cut quartz crystal with a thickness of 333μm which involves native oxide and contamination removals in the chemical solution such as the piranha solution which has sulphuric acid (H_2SO_4) and hydrogen peroxide (H_2O_2) in the ratio of 3:1 at a temperature of 110 ^{0} C [106]. A clean quartz crystal without impurities is necessary in order to have a better cohesion between

the quartz and the electrodes. The impurities present during the fabrication process contaminate the device and affects the performance of the device.

B. Photolithography – Patterning the etch area on top

Photolithography is the process of patterning the substrate with the help of a predesigned mask and exposing it to UV light in order to make a pattern in the substrate. The photolithography is carried out on the AT cut quartz substrate to pattern the area for the etching process of the quartz. The photolithography is started with the deposition of the photoresist layer on the quartz substrate as shown in the Figure 7.1. Followed by this, the mask with the top electrode pattern is aligned on the photoresist layer and it is exposed to the UV light. The substrate is then immersed in a developer solution that further removes the exposed area of the photoresist. This transferred circular patterned area from the mask to the substrate has a radius of about 2mm which is the area that needs to be etched further.

Quartz crystal   Photoresist

(a)

UV light

Quartz crystal   Photoresist   Mask

(b)

Quartz crystal ▮ Photoresist ▮

(c)
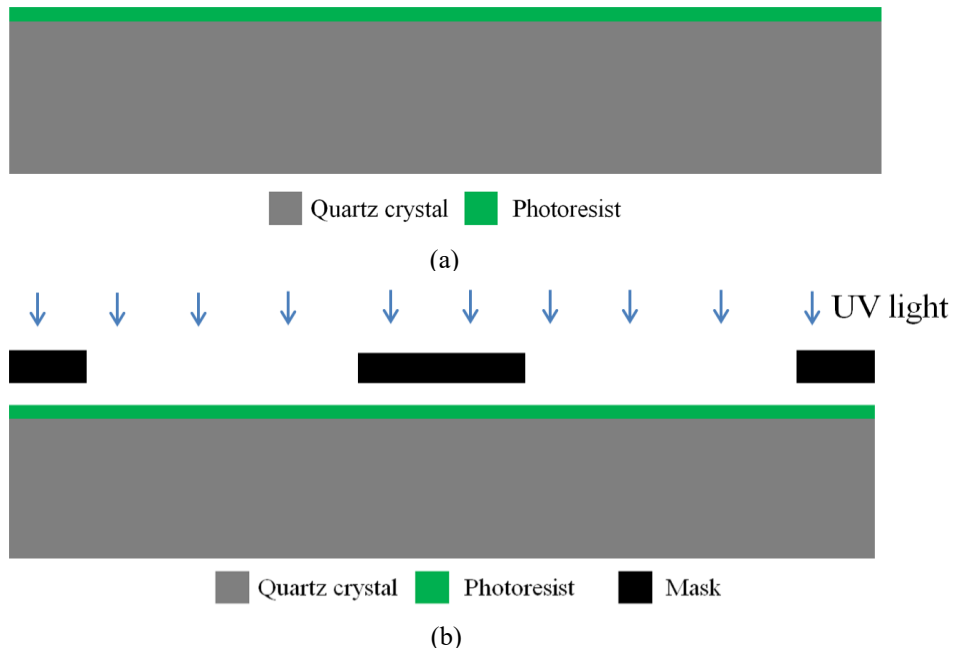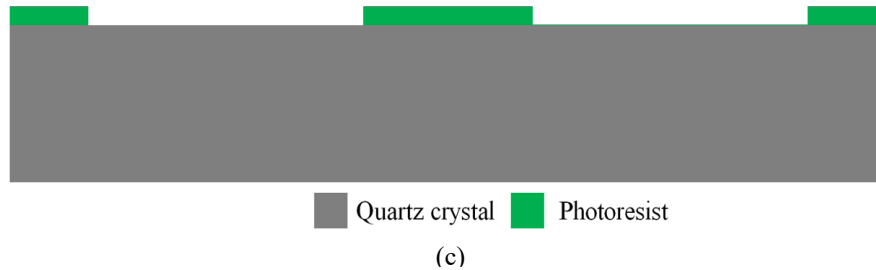
Fig. 7.1: Schematic views of photolithography process to pattern the quartz etch area (a) deposition of photoresist on the quartz crystal (b) Alignment of mask and UV light exposure (c) patterned quartz crystal.

C. Deep reactive ion etching (DRIE) – To build inverted mesa structures on top

After patterning the area for etching through photolithography, the patterned area needs to be etched in order to fabricate the inverted mesa structure in the quartz substrate. The quartz can be etched either by wet etching with chemicals such as hydrofluoric acid of 16% or the deep-reactive ion etching process. The deep reactive ion etching has many comparative advantages such as the good anisotropic etching ability and more accurate structures without structural defects. Thus, deep reactive ion etching is preferred in quartz etching. The deep reactive ion etching can be carried out with the SF_6 and Xe gases [107]. The following DRIE process can be carried out at a process pressure of 1.5mTorr, and cathode temperature of 20^0 C. The etch rate is usually within the range of 0.4 – 0.5 μm/min [107]. Thus the inverted mesa structure of depth of 141.5μm is be obtained on the top side of the device. The etched area is washed with the dilute HF solution of 1% in order the remove the reaction products on the etched quartz surface and then the photoresist layer is removed. Thus the inverted mesa structures are developed in the top side of the quartz substrate as shown in the Figure 7.2.
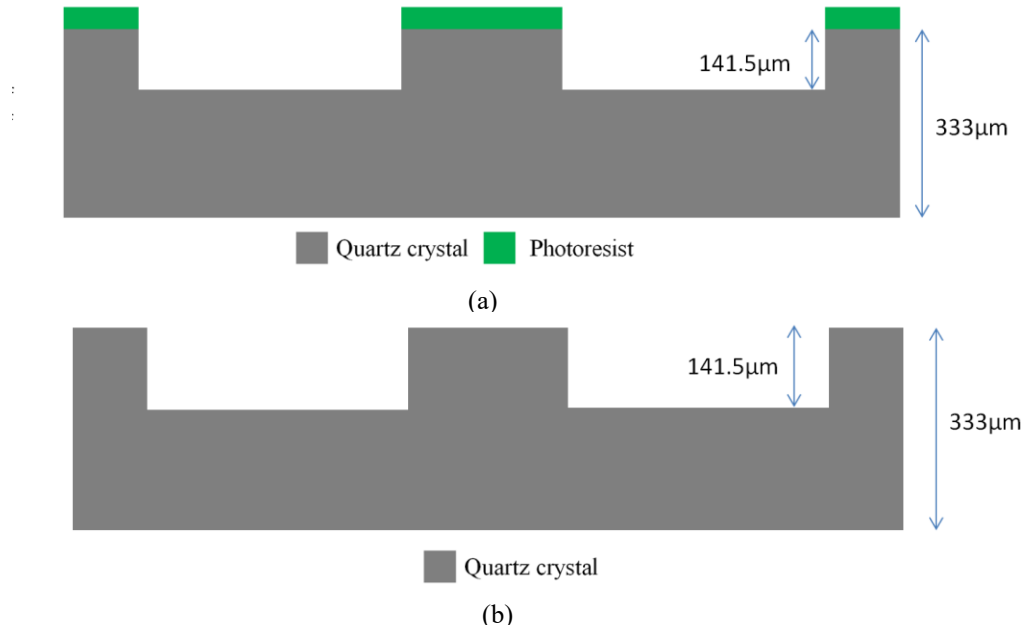
Fig. 7.2: Schematic view of AT cut quartz etching process (a) Deep reactive ion etching process (b) Etched quartz with inverted mesa structures.

D. Deposition and patterning of top electrodes

The deposition of top electrodes is carried out by electron beam evaporation process. Electron beam evaporation is the process in which the current is passed through the tungsten element, which leads to electron emission. High voltage is used to accelerate the electrons and a strong magnetic field focuses these electrons into the target gold metal which in turn evaporates and sublimate into the quartz substrate. The electron beam evaporation has many advantages such as the high directional control, low level of impurity, high efficiency in utilizing the metal, excellent uniformity, high deposition rate of 100Å/s which is better than sputtering and resistive thermal evaporation for high throughput [108]. The chromium layer of thickness 20nm is deposited on the patterned area and gold layer of 300nm thickness are then deposited using the electron beam evaporation process as shown in the Figure 7.3 (a). The chromium layer of thickness 20nm increases the adhesion between the gold electrodes and the quartz substrate.

In order to obtain a concentric pattern for the top electrode, the gold layer is patterned with the help of photolithography process. The photolithography process is carried out with the deposition of photoresist layer followed by the alignment of the lithographic mask layer. Then the setup is exposed to UV light which forms the required pattern. The following process patterns the top electrodes as shown in the Figure 7.3 (b), (c), (d) and prepares the region for further removal of unwanted gold and chromium layers.

(a)

(b)

(c)

(d)
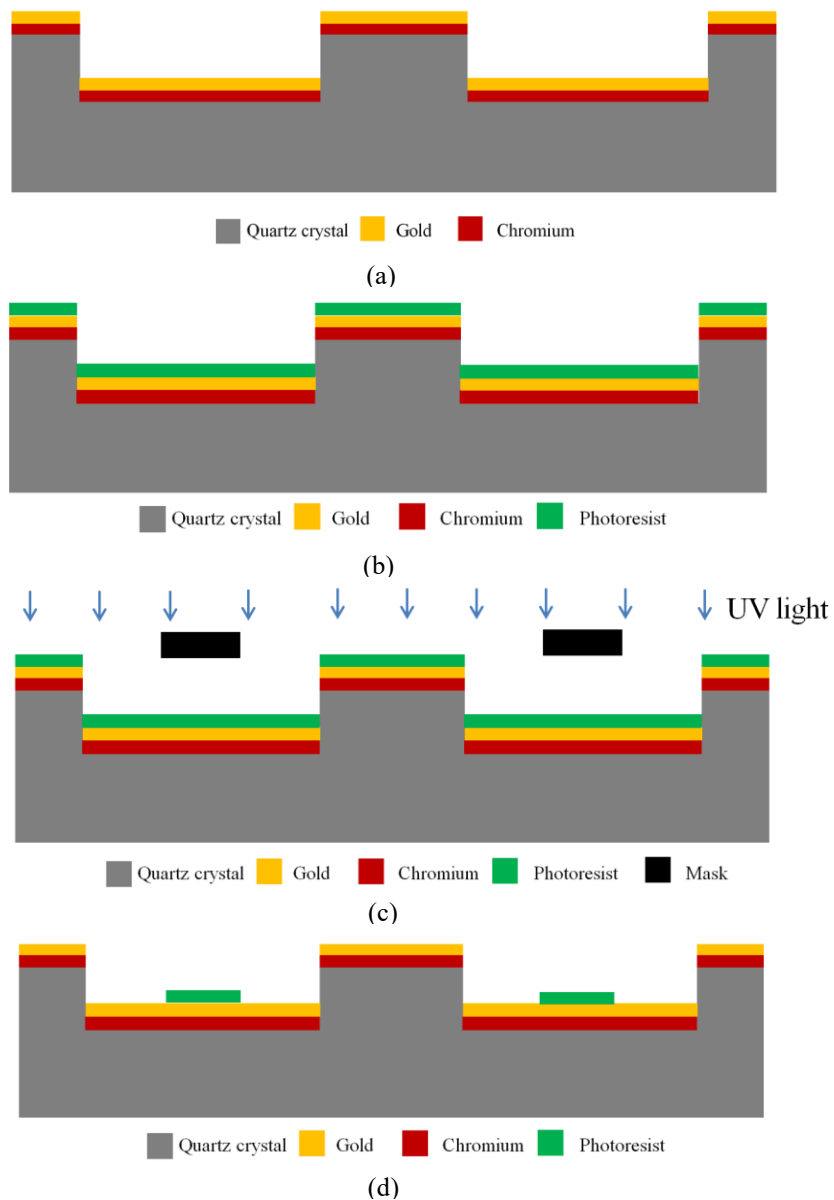
Fig. 7.3: Schematic view of deposition of chromium and gold followed by the photolithography process to pattern the electrode area (a) deposition of chromium of 20nm and gold of 300nm (b) deposition of photoresist (c) Alignment of mask layer and exposure to UV light (d) Patterned gold layer.

E. Formation of top electrodes and spray coating of photoresist protection

Using etchants, the exposed chromium and the gold layer without the photoresist layer protection are removed. Then the substrate is immersed in the chemical solution such as acetone to remove the photoresist layer to form the final top electrode structure as shown in the Figure 7.4 (a) which is made up of 20nm of chromium and 300nm of gold.

Then, the photoresist layer is spray coated in the fabricated top surface of the device as shown in the Figure 7.4 (b). The photoresist layer acts as a protective layer which protects the fabricated top surface from exposure to etching gases during the upcoming bottom layer fabrication of the device.

(a)

(b)
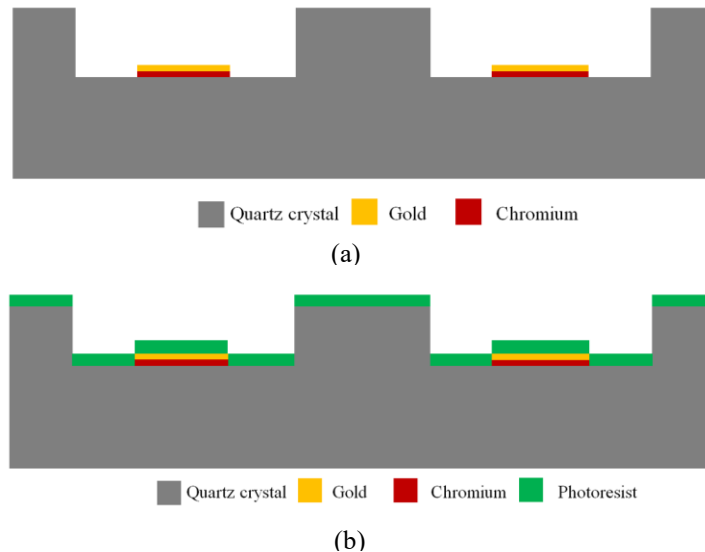
Fig. 7.4: Schematic view of defining the top concentric electrodes (a) Using gold and chromium etchants, the exposed metallic layers are removed (b) Spray coating of photoresist on the top surface as a protective layer for further fabrication.

F. Photolithography – Patterning the etch area on the inverted device

95

The device is inverted for the further fabrication of the reference electrodes on the inverted mesa structures. The photoresist layer is spray coated on the surface followed by the alignment of the lithographic mask and exposure to UV light which pattern the surface for quartz etching process with a dimension of 2mm radius which is similar to the radius of top etched area as shown in the Figure 7.5.
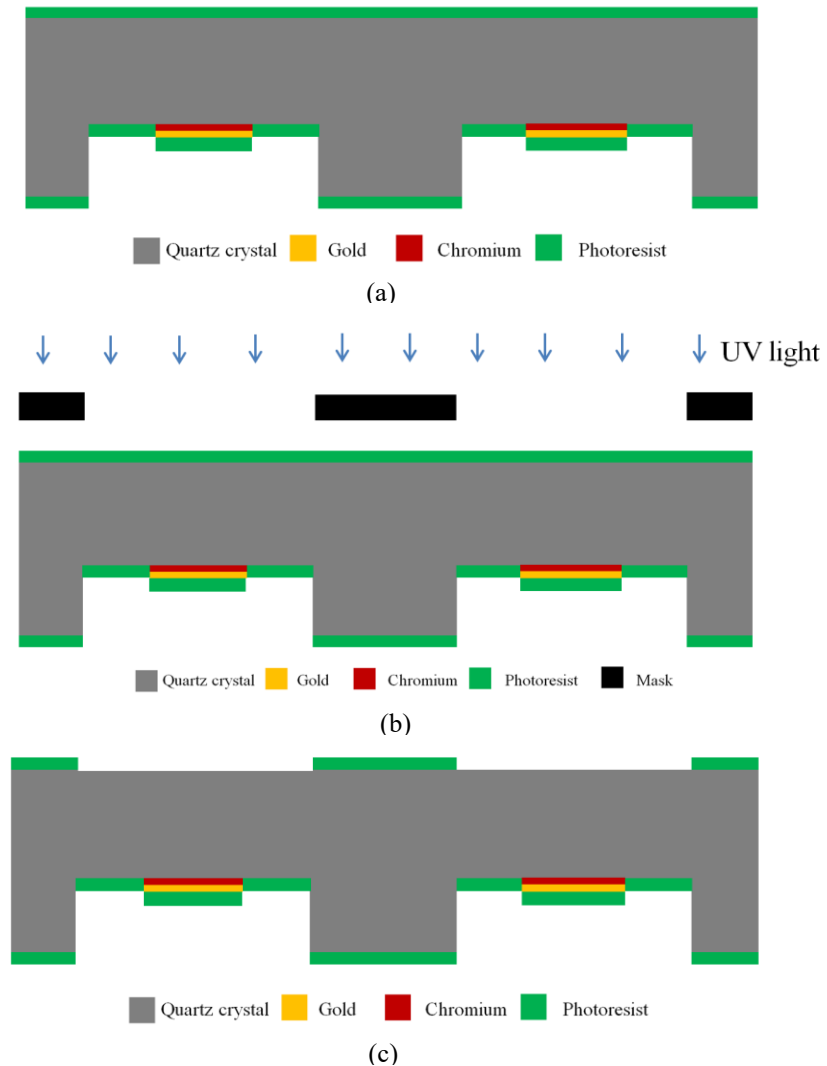
Fig. 7.5: Schematic views of photolithography process to pattern the quartz etch area on the inverted device (a) deposition of photoresist on the quartz crystal (b) Alignment of mask and UV light exposure (c) patterned quartz crystal.

G. Deep reactive ion etching (DRIE) – To build inverted mesa structures on inverted device

In order to form inverted mesa structures on the inverted device, the deep reactive ion etching process is repeated on the patterned region of the quartz crystal for up to 141.5μm. This develops a vibrating quartz plate of thickness 50μm in the middle region. Then the etched area is washed with the dilute HF solution of 1% in order the remove the reaction products on the etched quartz surface and then the photoresist layer is removed by immersing the device in the chemical solution as shown in the Figure 7.6. This process also removes the protective photoresist layer on the top surface which was earlier deposited and exposes the concentric electrodes.

(a)

(b)
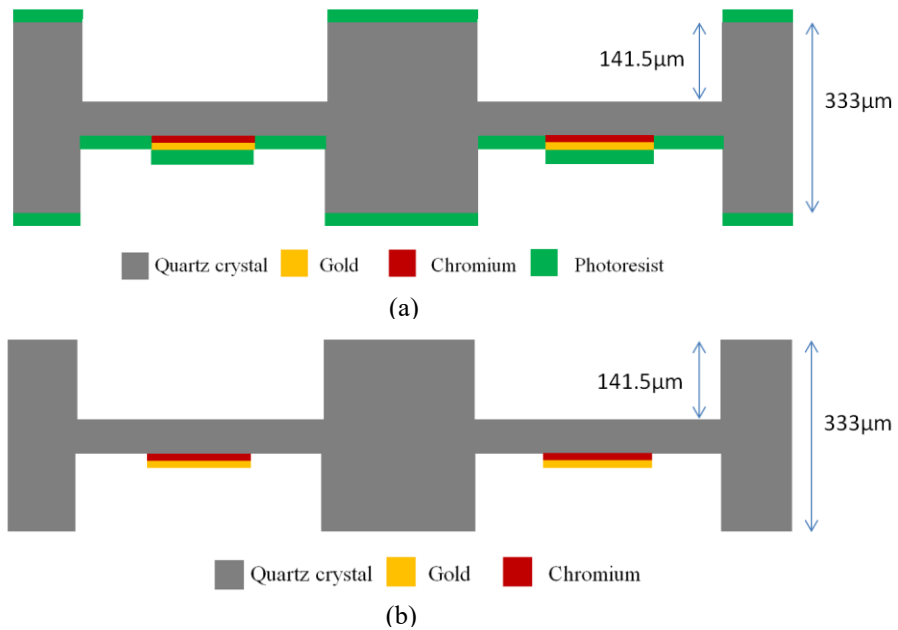
Fig. 7.6: Schematic view of deep reactive ion etching process on the inverted device (a) etched quartz crystal (b) Removal of photoresist layer.

H. Deposition and patterning of reference electrodes

The chromium of 20nm and gold of 300nm is deposited on the inverted etched quartz crystal by the electron beam evaporation process. Then the deposited metal layers

are patterned by the photolithography process to pattern the circular reference electrodes with a radius of 500μm which is similar to the radius of the top electrode as shown in the Figure 7.7.

(a)

(b)

(c)

(d)
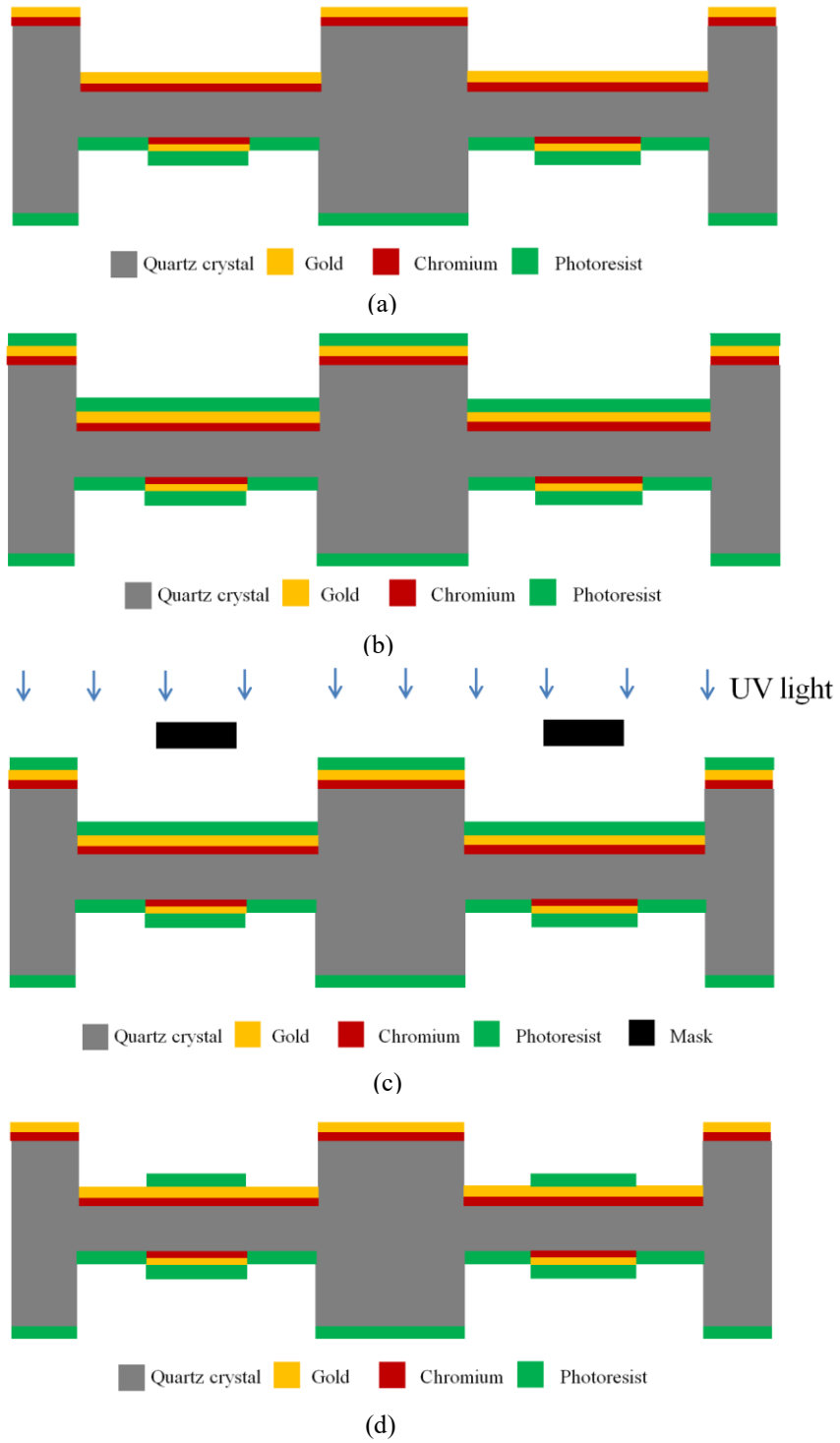
Fig. 7.7: Schematic view of deposition of chromium and gold followed by the photolithography process to pattern the circular reference electrode (a) deposition of chromium of 20nm and gold of 300nm (b) Deposition of photoresist (c) Alignment of mask layer and exposure to UV light (d) Patterned gold layer on quartz.

I. Formation of reference electrodes

The exposed gold and chromium metal layers on the inverted quartz are removed away by the etchants as shown in the Figure 7.8 (a). Then the remaining photoresist layer on the device is removed is immersing the quartz in the chemical solution such as acetone to form the circular reference electrodes as shown in the Figure 7.8 (b). Thus the proposed 33.3MHz dual inverted mesa quartz crystal microbalance sensor array is fabricated.

(a)

(b)
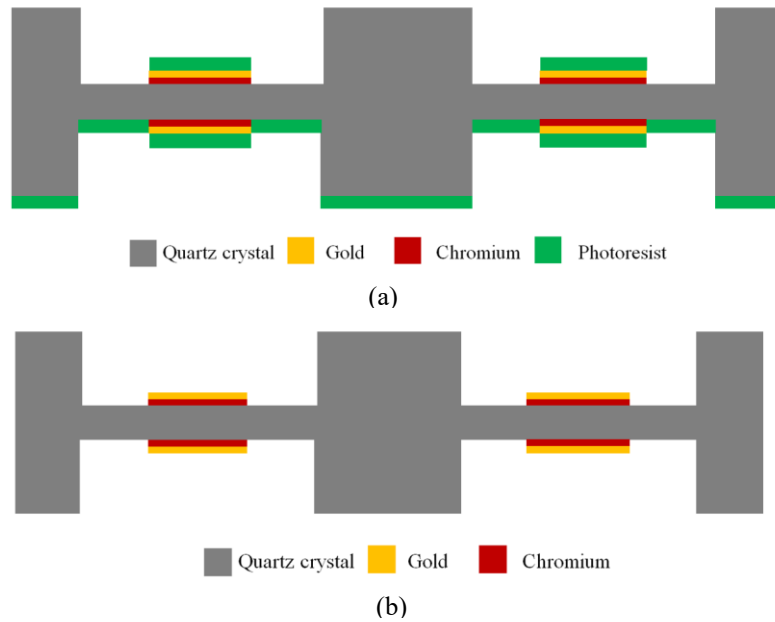
Fig. 7.8: Schematic view of formation of bottom circular electrodes (a) Using gold and chromium etchants, the exposed metallic layers are removed on the inverted quartz (b) Photoresist layers are removed by the developer solution.

The proposed fabrication process can be employed on multiple QCM channels depending on the substrate size. For instance, with a constant radius of electrode of

500μm and radius of vibrating quartz of 2mm, the number channels that can be employed are given below.

- With a non-vibrating quartz substrate dimension of 26mm × 26mm and a thickness of 333μm, four dual inverted mesa channels with a fundamental resonant frequency of 33.3MHz can be fabricated.

- With a non-vibrating quartz substrate dimension of 12mm × 12mm and a thickness of 333μm, four dual inverted mesa channels with a fundamental resonant frequency of 10MHz can be fabricated.

The 4 × 4 array of dual inverted mesa quartz crystal microbalance sensor dimensions for the 33.3MHz and 10MHz fundamental resonant frequency are listed in the Table 7.1.

Table 7.1: Dimensions of dual inverted mesa quartz crystal microbalance for 10MHz and 33.3MHz fundamental resonant frequency.

Resonant frequency	10MHz	33.3MHz
Radius of electrode (RE)	500μm	500μm
Thickness of electrode (TE)	320nm	320nm
Radius of quartz (RQ)	2mm	2mm
Center to center distance (c2c)	6mm	13mm
Vibrating thickness (VT)	167μm	50μm
Non vibrating thickness (NVT)	333μm	333μm
Length * breadth of each channel	6mm × 6mm	13mm × 13mm

The top and bottom view of the final design of the advanced dual inverted mesa quartz crystal microbalance sensor with the electrical connections has been shown in the Figure 7.9 and 7.10.
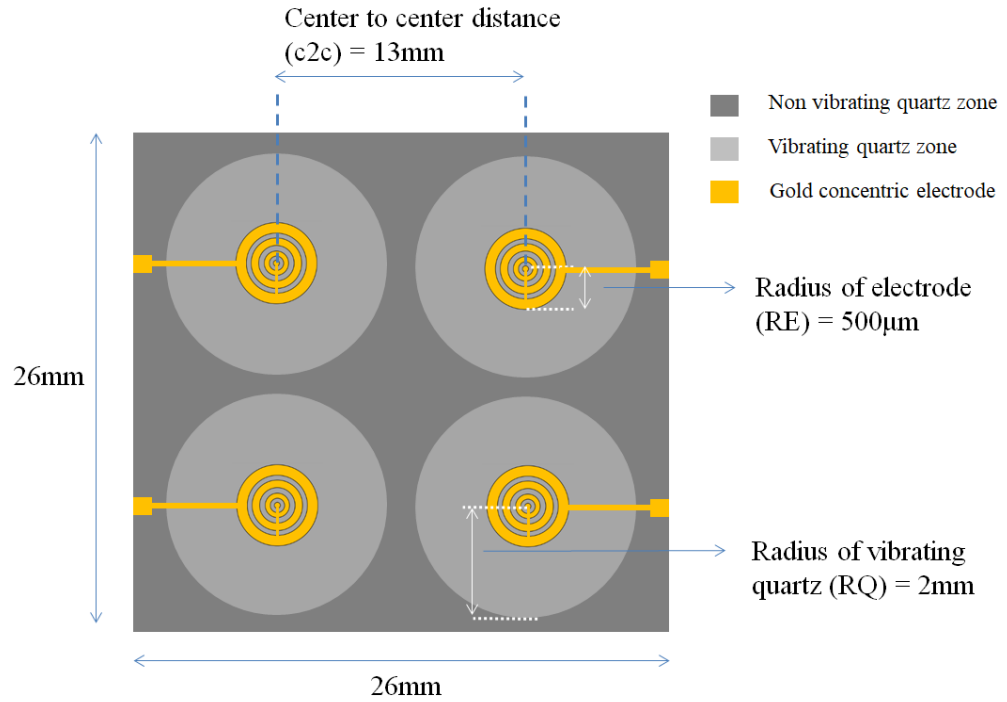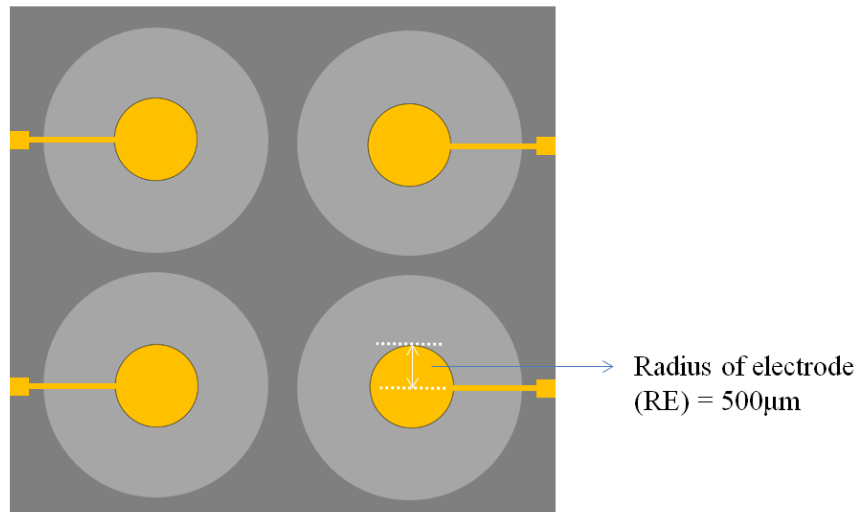
Fig. 7.9: Schematic view of dual inverted mesa quartz crystal microbalance sensor for 33.3MHz (a) Top view of the sensor showing four channels with concentric electrodes (b) Bottom view of the sensor showing four channels with circular reference electrodes.
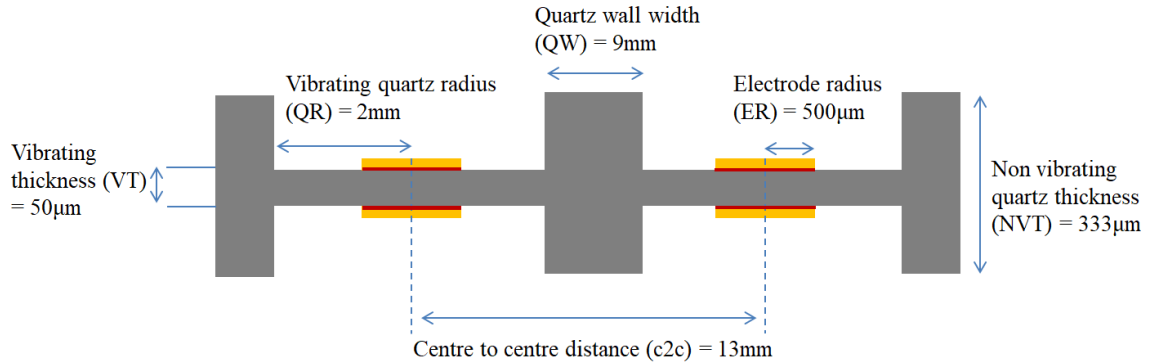
Fig. 7.10: Schematic view of dual inverted mesa quartz crystal microbalance sensor showing side view of the device for 33.3MHz.

7.3 Conclusion

The fabrication procedure of the multichannel dual inverted mesa structured quartz crystal microbalance sensor is proposed in the chapter. The deep reactive ion etching process has been chosen over the other quartz etching process such as the wet chemical etching. In order to deposit the metallic electrodes, there are various deposition process from which the electron beam evaporation has been chosen over the other deposition methods such as the sputtering, thermal evaporation because of its poor side wall coverage or highly directional and fast deposition. Furthermore, the complete fabrication steps have been analyzed and the difference in the dimensions between the 10MHz and 33.3MHz channels are tabulated which also states the space required for each channel in the quartz substrate. Depending upon the number of channels, the electrical connections are modeled in order to save space.

CHAPTER 8

CONCLUSION AND FUTURE WORK

Lung cancer is recognized as the second leading disease with highest death rate after the heart disease by the data provided by world health organization. Lung cancer has claimed more than 1.76 million lives in the year 2018. Due to the fact that 90% of the lung cancer patients are diagnosed only during the later stages, the process of treating the lung cancer becomes highly complicated for the medical practitioners. At the later stage of the cancer, the tumorous cells spread to the other parts of the body which makes the treatment process more complex. Thus the lung cancer patients become less probable to be cured completely. Various researches have suggested that the early diagnosis of the lung cancer provides a higher probability for the patients to be cured. Studies have suggested that the lung cancer patients exhale volatile organic compounds in their breath in very low concentrations. Therefore detecting these volatiles with appropriate gas sensors at the early stages can detect the lung cancer before the tumour cells have become difficult to treat.

There are various gas sensors available to detect these volatile organic compounds at low concentrations. Each gas sensors has their own advantages and disadvantages in their working capabilities. However there are certain qualities in the sensor which makes it highly suitable towards the lung cancer detection on a wide range scale. The problem with the existing detection capabilities are high cost, large in size, higher processing times. The suitable qualities of an ideal gas sensor to detect these volatiles are listed below.

- High sensitivity to detect gas targets at low concentrations

- Multiple gas detection to detect multiple gas targets

- Low cost to enable accessibility on a wide range scale

- Comparatively easier fabrication procedure for fast and low cost manufacturing

- Comparatively robust design

The focus of this research was on quartz crystal microbalance gas sensor which came much closer to these qualities compared to the other gas sensors. Thus, the quartz crystal microbalance gas sensor is studied, analyzed, investigated and customized in this research to improve its performance and designing the sensor in a way to detect multiple volatile organic compounds. The designed customized quartz crystal microbalance gas sensor array has provided a platform for the detection of multiple volatile organic compounds with the above mentioned qualities and thereby enabling the early diagnosis of lung cancer detection feasible. The design process of this sensor with the predefined qualities is explained in the summary as follows.

8.1 Summary and Discussion

There are several types of the gas sensors available to detect the volatile organic compounds but each are constrained with various limitations that makes them unsuitable for the predefined qualities such as the ability to detect multiple gas targets in an array configuration, high sensitivity to the target gas, comparatively low cost of the materials used in the sensor and easier fabrication procedure which further reduce the cost of the device. Therefore each gas sensors are investigated for their own advantages and disadvantages and each of these sensors are analyzed for their ability to match closely to the predefined qualities. The results of this comprehensive analysis of the various gas sensors from different background of principle of operations have concluded that the

quartz crystal microbalance sensor as the sensor which is highly matching with the predefined qualities. Thus the quartz crystal microbalance is chosen as the research focus and further investigated more in order to customize it to match closely with the qualities.

The quartz crystal microbalance is a sensor device which works on the principle of inverse piezoelectric effect. It is designed with a AT cut quartz crystal sandwiched between two metallic electrodes. It undergoes thickness shear mode of oscillation at resonant frequency when electric current at alternation potentials are applied on the electrodes. Due to its mass sensitivity, when mass even up to nano gram comes into contact with the sensing top electrode, the resonant frequency of the device decreases which can be measured with high frequency oscilloscope. This is the basic working principle of the device. Furthermore, the Sauerbrey's equations are studied to analyze it concepts in the operation followed by their analysis of equivalent mechanical and electrical circuits.

By using the Sauerbrey's equation, the analytical modelling of the quartz crystal microbalance has been done which further stated the critical design parameters. The critical design parameters are then further investigated to obtain the results listed as follows,

- The thickness of the AT quartz crystal and the resonant frequency of the device are directly proportional to each other.
- The change in mass and change in frequency has a linear relationship between them.
- The mass sensitivity is high on a small electrode compared to a large electrode.

Then the finite element analysis of the critical design parameters has been carried out using the COMSOL Multiphysics modeling tool to model some of the critical design parameters by analyzing the resonant frequency characteristics. The finite element analysis has provided a better understanding of certain parameters that cannot be directly modeled analytically and the key results are follows.

- Meshing characteristics are investigated in which the finer mesh is chosen to ensure independency of the simulation results to the chosen meshing number and for its high accuracy with low processing times.

- Thickness of the quartz crystal and its resonant frequency relations are investigated with the analytically modeled results to estimate the accuracy level of the finite element modeling tool.

- The minimum dimension of the quartz required to undergo a constant thickness shear mode oscillation is obtained.

- The thickness and radius of the electrode and their corresponding displacement and resonant frequency relations are obtained.

Due to the greater influence of electrode dimensions and structure in the distribution profile, they are further invested to optimize the performance of the device to obtain an approximately uniform mass sensitivity across the active sensing top electrode. Displacement profiles can be directly correlated to the sensitivity at that particular part of the electrode. The conventional circular top electrode is found to be possessed with higher displacement only towards the centre portion of the electrode. Therefore alternate electrode structures such as the ring electrode and ring dot electrode are investigated for

their distribution profiles. The key significant investigations and results are listed as follows,

- A comprehensive comparison between the displacement profiles of the circular, ring, and ring dot electrodes has been done which has shown that the alternative electrode structures can indirectly counter the energy trapping effect of the quartz.

- Ring dot electrode is customized with multiple rings and the displacement profiles are analyzed which has given a comparatively better displacement compared to the latter electrode structures.

- The multiple electrode structure has been further customized with increasing ring width and decreasing ring gaps and they are shown to produce an even and approximately uniform displacement profile which is named as the concentric electrodes.

- The customized concentric electrodes are further compared with the conventional circular electrodes to showcase the higher efficiency of the modeling process.

Despite obtaining a comparatively better displacement profile across the electrode structure, single channel gas sensor cannot detect multiple targets. Therefore an array of highly sensitive and advanced quartz crystal microbalance sensors on a monolithic substrate has been designed and analyzed. The limitation of the monolithic array is that the channels are needed to be placed in such a way that the displacement of the native channel does not disturb the neighboring channel in order to avoid errors due to the crosstalk. The significant investigations in the array configuration and the accomplished results are listed as follows.

- The un-etched quartz array design with four channels has been designed and the frequency interference has been eliminated by analyzing its frequency profile on a 5MHz crystal.

- The un-etched quartz array design cannot handle frequencies above 5MHz as it takes wide center to center distance to attain zero frequency interference. Therefore an advanced dual inverted mesa quartz crystal microbalance array has been proposed to work with higher frequencies such as 10MHz and 33MHz.

- Frequency interference was later eliminated in the 10MHz and 33MHz design and the size of the array was customized to be smaller than the 5MHz design. In short, high performance and sensitivity with a small overall size of the sensor with robust construction,

Furthermore, in order to fabricate the designed dual inverted mesa quartz crystal microbalance sensor array, there are various fabrication techniques are available. The suitable fabrication techniques with high accuracy in the resulting device are chosen and the fabrication techniques are proposed.

8.2 Future Work

The major problem with most of the gas sensors is the process of designing them to be particularly sensitive with the target gas. Studies have suggested that there are three possible solutions to tackle this limitation which are,

- Designing a large array of sensors and using particular sections of these arrays with different sensing materials to target different gases.

- Implementing micro heater unit in the sensor and changing the temperature of the sensing materials and influencing the sensing material to be more sensitive to various gases at different temperature cycles.

- Implementing sensitive materials which are particularly more sensitive to the lung cancer specific volatile organic compounds.

The high sensitive array design has been already designed in this research. Thus the next two design factors can be implemented in to the customized dual inverted mesa quartz crystal microbalance array and the device can be fabricated.

REFERENCES

[1]   "Lung Cancer Fact Sheet," American Lung Association. [Online]. Available: https://www.lung.org/lung-health-and-diseases/lung-disease-lookup/lung-cancer/resource-library/lung-cancer-fact-sheet.html. [Accessed: 08-Nov-2019].

[2]   "Lung cancer statistics - Canadian Cancer Society," www.cancer.ca. [Online]. Available: https://www.cancer.ca/en/cancer-information/cancer-type/lung/statistics/?region=pe. [Accessed: 08-Nov-2019].

[3]   "Myths and Facts," Lung Cancer Canada. [Online]. Available: https://www.lungcancercanada.ca/Lung-Cancer/Myths-and-Facts.aspx. [Accessed: 08-Nov-2019].

[4]   R. Capuano, A. Catini, R. Paolesse, and C. D. Natale, "Sensors for Lung Cancer Diagnosis," Journal of Clinical Medicine, vol. 8, no. 2, p. 235, Nov. 2019.

[5]   "Cancer," World Health Organization. [Online]. Available: https://www.who.int/news-room/fact-sheets/detail/cancer. [Accessed: 08-Nov-2019].

[6]   C. Lauren, H. Christopher, P. Robert, E. Robert "Lung Cancer: Diagnosis and Management," Pharmacology & Therapeutics, vol. 198, pp. 189–205, 2019.

[7]   M. Alexander, J. Andrew, "Nanotechnology in the diagnosis and treatment of lung cancer," Pharmacology & Therapeutics, vol. 198, pp. 189–205, 2019.

[8]   S. Kort, M. Tiggeloven, M. Brusse-Keizer, J. Gerritsen, J. Schouwink, E. Citgez, F. D. Jongh, S. Samii, J. V. D. Maten, M. V. D. Bogart, and J. V. D. Palen, "Multi-centre prospective study on diagnosing subtypes of lung cancer by exhaled-breath analysis," Lung Cancer, vol. 125, pp. 223–229, 2018.

[9]   M. M. Jacobsen, S. C. Silverstein, M. Quinn, L. B. Waterston, C. A. Thomas, J. C. Benneyan, and P. K. Han, "Timeliness of access to lung cancer diagnosis and treatment: A scoping literature review," Lung Cancer, vol. 112, pp. 156–164, 2017.

[10] N. Shinagawa, "A review of existing and new methods of bronchoscopic diagnosis of lung cancer," Respiratory Investigation, vol. 57, no. 1, pp. 3–8, 2019.

[11] T. C. Kennedy and F. R. Hirsch, "Using molecular markers in sputum for the early detection of lung cancer: A review," Lung Cancer, vol. 45, 2004.

[12] Y. Saalberg and M. Wolff, "VOC breath biomarkers in lung cancer," Clinica Chimica Acta, vol. 459, pp. 5–9, 2016.

[13] J. Zhou, Z.-A. Huang, U. Kumar, and D. D. Chen, "Review of recent developments in determining volatile organic compounds in exhaled breath as biomarkers for lung cancer diagnosis," Analytica Chimica Acta, vol. 996, pp. 1–9, 2017.

[14] P. J. Mazzone, "Analysis of Volatile Organic Compounds in the Exhaled Breath for the Diagnosis of Lung Cancer," Journal of Thoracic Oncology, vol. 3, no. 7, pp. 774–780, 2008.

[15] A. Khanmohammadi, A. Aghaie, E. Vahedi, A. Qazvini, M. Ghanei, A. Afkhami, A. Hajian, and H. Bagheri, "Electrochemical biosensors for the detection of lung cancer biomarkers: A review," Talanta, vol. 206, p. 120251, 2020.

[16] W. Zhao, L. F. Al-Nasser, S. Shan, J. Li, Z. Skeete, N. Kang, J. Luo, S. Lu, C.-J. Zhong, C. J. Grausgruber, and R. Harris, "Detection of mixed volatile organic compounds and lung cancer breaths using chemiresistor arrays with crosslinked nanoparticle thin films," Sensors and Actuators B: Chemical, vol. 232, pp. 292–299, 2016.

[17] G. Song, T. Qin, H. Liu, G.-B. Xu, Y.-Y. Pan, F.-X. Xiong, K.-S. Gu, G.-P. Sun, and Z.-D. Chen, "Quantitative breath analysis of volatile organic compounds of lung cancer patients," Lung Cancer, vol. 67, no. 2, pp. 227–231, 2010.

[18] G. Rocco, G. Pennazza, M. Santonico, F. Longo, R. Rocco, P. Crucitti, and R. A. Incalzi, "Breathprinting and Early Diagnosis of Lung Cancer," Journal of Thoracic Oncology, vol. 13, no. 7, pp. 883–894, 2018.

[19] K. B. Biji, C. N. Ravishankar, C. O. Mohan, and T. K. Srinivasa Gopal, "Smart packaging systems for food applications: a review," Journal of food science and technology, Oct-2015. [Online]. Available: https://www.ncbi.nlm.nih.gov/pmc/articles/PMC4573137/. [Accessed: 08-Nov-2019].

[20] C. Wang, L. Yin, L. Zhang, D. Xiang, and R. Gao, "Metal oxide gas sensors: sensitivity and influencing factors," Sensors (Basel, Switzerland), 2010. [Online]. Available: https://www.ncbi.nlm.nih.gov/pmc/articles/PMC3264469/. [Accessed: 08-Nov-2019].

[21] A. Caron, N. Redon, P. Coddeville, and B. Hanoune, "Identification of indoor air quality events using a K-means clustering analysis of gas sensors data," Sensors and Actuators B: Chemical, 22-Jun-2019.

[22] K. C. Persaud, A. M. Pisanelli, S. Szyszko, M. Reichl, G. Horner, W. Rakow, H. J. Keding, and H. Wessels, "A smart gas sensor for monitoring environmental changes in closed systems: results from the MIR space station," Sensors and Actuators B: Chemical, 17-Jun-1999.

[23] P. Brinkman, A. H. Wagener, P.-P. Hekking, A. T. Bansal, A.-H. M.-van der Zee, Y. Wang, H. Weda, H. H. Knobel, T. J. Vink, N. J. Rattray, A. D'Amico, G. Pennazza, M. Santonico, D. Lefaudeux, B. D. Meulder, C. Auffray, P. S. Bakke, M. Caruso, and P. J. Sterk, "Identification and prospective stability of electronic nose (eNose)–derived inflammatory phenotypes in patients with severe asthma," Journal of Allergy and Clinical Immunology, 06-Dec-2018.

[24] A. Mirzaei, S. S. Kim, and H. W. Kim, "Resistance-based H2S gas sensors using metal oxide nanostructures: A review of recent advances," Journal of Hazardous Materials, 06-Jun-2018

[25] T. Ishihara, K. Kometani, Y. Mizuhara, and Y. Takita, "A new type of CO2 gas sensor based on capacitance changes," Sensors and Actuators B: Chemical, 31-Oct-2001.

[26] S. Park, I. Yoon, S. Lee, H. Kim, J.-W. Seo, Y. Chung, A. Unger, M. Kupnik, and H. J. Lee, "CMUT-based resonant gas sensor array for VOC detection with low operating voltage," Sensors and Actuators B: Chemical, 11-Jul-2018.

[27] A. Dey, "Semiconductor metal oxide gas sensors: A review," Materials Science and Engineering: B, 05-Jan-2018.

[28] A. Mirzaei, S. G. Leonardi, and G. Neri, "Detection of hazardous volatile organic compounds (VOCs) by metal oxide nanostructures-based gas sensors: A review," Ceramics International, 23-Jun-2016.

[29] S. Kumar, V. Pavelyev, P. Mishra, and N. Tripathi, "A review on chemiresistive gas sensors based on carbon nanotubes: Device and technology transformation," Sensors and Actuators A: Physical, 28-Sep-2018.

[30] S. Fanget, S. Hentz, P. Puget, J. Arcamone, M. Matheron, E. Colinet, P. Andreucci, L. Duraffourg, E. Myers, and M. L. Roukes, "Gas sensors based on gravimetric detection-A review," Sensors and Actuators B: Chemical, 02-Sep-2011.

[31] S. Pandey, "Highly sensitive and selective chemiresistor gas/vapor sensors based on polyaniline nanocomposite: A comprehensive review," Journal of Science: Advanced Materials and Devices, 18-Oct-2016.

[32] Y. Daskal, R. Dittrich, J. Walter, and Y. Joseph, "Chemiresistor Sensors Based on Gold Nanoparticle Composites," Procedia Engineering, 11-Sep-2015.

[33] W. Zhao, L. F. Al-Nasser, S. Shan, J. Li, Z. Skeete, N. Kang, J. Luo, S. Lu, C.-J. Zhong, C. J. Grausgruber, and R. Harris, "Detection of mixed volatile organic compounds and lung cancer breaths using chemiresistor arrays with crosslinked nanoparticle thin films," Sensors and Actuators B: Chemical, 24-Mar-2016.

[34] F. Rigoni, S. Tognolini, P. Borghetti, G. Drera, S. Pagliara, A. Goldoni, and L. Sangaletti, "Environmental Monitoring of Low-ppb Ammonia Concentrations Based on Single-wall Carbon Nanotube Chemiresistor Gas Sensors: Detection Limits, Response Dynamics, and Moisture Effects," Procedia Engineering, 31-Dec-2014.

[35] A. Mirzaei, S. S. Kim, and H. W. Kim, "Resistance-based H2S gas sensors using metal oxide nanostructures: A review of recent advances," Journal of Hazardous Materials, 06-Jun-2018.

[36] G. F. Fine, L. M. Cavanagh, A. Afonja, and R. Binions, "Metal oxide semi-conductor gas sensors in environmental monitoring," Sensors (Basel, Switzerland), 2010.

[37] D. Zappa, V. Galstyan, N. Kaur, H. M. M. M. Arachchige, O. Sisman, and E. Comini, "'Metal oxide -based heterostructures for gas sensors'- A review," Analytica Chimica Acta, 17-Sep-2018.

[38] S. Phanichphant, "Semiconductor Metal Oxides as Hydrogen Gas Sensors," Procedia Engineering, 31-Dec-2014.

[39] H. Nazemi, A. Joseph, J. Park, and A. Emadi, "Advanced Micro- and Nano-Gas Sensor Technology: A Review," MDPI, 14-Mar-2019.

[40] M. H. Naveen, N. G. Gurudatt, and Y.-B. Shim, "Applications of conducting polymer composites to electrochemical sensors: A review," Applied Materials Today, 21-Sep-2017.

[41] S. Cichosz, A. Masek, and M. Zaborski, "Polymer-based sensors: A review," Polymer Testing, 13-Mar-2018.

[42] Y. Cao, T. Feng, J. Xu, and C. Xue, "Recent advances of molecularly imprinted polymer-based sensors in the detection of food safety hazard factors," Biosensors and Bioelectronics, 19-Jun-2019.

[43] F. G. Zamani, H. Moulahoum, M. Ak, D. O. Demirkol, and S. Timur, "Current trends in the development of conducting polymers-based biosensors," TrAC Trends in Analytical Chemistry, 06-Jun-2019.

[44] J. Liu, Y. Wang, X. Liu, Q. Yuan, Y. Zhang, and Y. Li, "Novel molecularly imprinted polymer (MIP) multiple sensors for endogenous redox couples determination and their applications in lung cancer diagnosis," Talanta, 02-Mar-2019.

[45] A. M. Sanjuán, J. A. R. Ruiz, F. C. García, and J. M. García, "Recent developments in sensing devices based on polymeric systems," Reactive and Functional Polymers, 19-Oct-2018.

[46] N. Kumar, P. Sahatiya, and P. Dubey, "Fabrication of CNT based Gas Sensor Using Interdigitated Gold Electrodes," Procedia Materials Science, 09-Sep-2014.

[47] S. Kumar, V. Pavelyev, P. Mishra, and N. Tripathi, "A review on chemiresistive gas sensors based on carbon nanotubes: Device and technology transformation," Sensors and Actuators A: Physical, 28-Sep-2018.

[48] T. Han, A. Nag, S. C. Mukhopadhyay, and Y. Xu, "Carbon nanotubes and its gas-sensing applications: A review," Sensors and Actuators A: Physical, 02-Apr-2019.

[49] Z. Xiao, L. B. Kong, S. Ruan, X. Li, S. Yu, X. Li, Y. Jiang, Z. Yao, S. Ye, C. Wang, T. Zhang, K. Zhou, and S. Li, "Recent development in nanocarbon materials for gas sensor applications," Sensors and Actuators B: Chemical, 27-Jul-2018.

[50] H. Elhaes, A. Fakhry, and M. Ibrahim, "Carbon nano materials as gas sensors," Materials Today: Proceedings, vol. 3, no. 6, pp. 2483–2492, 2016.

[51] G. Sauerbrey, "Use of quartz vibrator for weighting thin films on a microbalance," Zeitschrift fur Physik , 155, 206–212, 1959.

[52] A. Alassi, M. Benammar, D. Brett, "Quartz Crystal Microbalance electronic interfacing systems: A Review," Sensors, 17, 2799, 2017.

[53] J. Zhang, J. Liang and T. Ueda, "Design and evaluation of a dual channel high frequency Quartz crystal Microbalance," 2016 10th International Conference on Sensing Technology (ICST), Nanjing, pp. 1-5, 2016.

[54] Su, Junwei, Wang, Pengtao, Sun, Hongwei, Dai, Wen, Cernigliaro, George, "Ultrasensitive quartz crystal microbalance enabled by micropillar structure," Applied Physics Letters, 104, 2014.

[55] J. Wang, L. Shen, J. Yang, "Effects of electrodes with continuously varying thickness on energy trapping in thickness-shear mode quartz resonators," Ultrasonics, Volume 48, Issue 2, Pages 150-154, 2008

[56] F. Dirri, E. Palomba, A. Longobardo, E. Zampetti, B. Saggin, and D. Scaccabarozzi, "A review of quartz crystal microbalances for space applications," Sensors and Actuators A: Physical, 21-Dec-2018.

[57] S. K. Vashist and P. Vashist, "Recent Advances in Quartz Crystal Microbalance-Based Sensors," Journal of Sensors, vol. 2011, pp. 1–13, 2011.

[58] W. Jakubik, P. Powroźnik, J. Wrotniak, M. Krzywiecki, and T. Hejczyk, "Theoretical Analysis of Acoustoelectrical Sensitivity in SAW Gas Sensors," Procedia Engineering, vol. 120, pp. 1261–1264, 2015.

[59] A. Mujahid, F.L. Dickert, "Surface Acoustic Wave (SAW) for Chemical Sensing Applications of Recognition layers," Sensors , 17, 2716, 2017

[60] M. Penza, P. Aversa, G. Cassano, W. Wlodarski, and K. Kalantarzadeh, "Layered SAW gas sensor with single-walled carbon nanotube-based nanocomposite coating," Sensors and Actuators B: Chemical, vol. 127, no. 1, pp. 168–178, 2007.

[61] M. Divagar, A. Gowri, S. John, and V. Sai, "Graphene oxide coated U-bent plastic optical fiber based chemical sensor for organic solvents," Sensors and Actuators B: Chemical, vol. 262, pp. 1006–1012, 2018.

[62] N. Paliwal and J. John, "Lossy Mode Resonance Based Fiber Optic Sensors," Smart Sensors, Measurement and Instrumentation Fiber Optic Sensors, pp. 31–50, Mar. 2016.

[63] Y.-nan Zhang, H. Peng, X. Qian, Y. Zhang, G. An, and Y. Zhao, "Recent advancements in optical fiber hydrogen sensors," Sensors and Actuators B: Chemical, 04-Jan-2017.

[64] M.-J. Yin, B. Gu, Q.-F. An, C. Yang, Y. L. Guan, and K.-T. Yong, "Recent development of fiber-optic chemical sensors and biosensors: Mechanisms, materials, micro/nano-fabrications and applications," Coordination Chemistry Reviews, vol. 376, pp. 348–392, 2018.

[65] H. Xiao-Wei, Z. Xiao-Bo, S. Ji-Yong, L. Zhi-Hua, and Z. Jie-Wen, "Colorimetric sensor arrays based on chemo-responsive dyes for food odor visualization," Trends in Food Science & Technology, vol. 81, pp. 90–107, 2018.

[66] X. Jin, Y. Huang, A. Mason, and X. Zeng, "Multichannel Monolithic Quartz Crystal Microbalance Gas Sensor Array," Analytical Chemistry, vol. 81, no. 2, pp. 595–603, 2009.

[67] Su, Junwei, Wang, Pengtao, Sun, Hongwei, Dai, Wen, Cernigliaro, George, "Ultrasensitive quartz crystal microbalance enabled by micropillar structure," Applied Physics Letters, 104, 2014.

[68] N. A. A. A. Rahman, A. H. Maradzi, and A. Zakaria, "Fabrication of quartz crystal microbalance with pegylated lipopolymer for detection of non-invasive lung cancer biomarker," Materials Today: Proceedings, vol. 7, pp. 632–637, 2019.

[69] H. Kanie, Y. Todo, Y. Hirota, M. Furukawa, T. Ueno and K. Tadamatsu, "Zero temperature coefficient characteristic of four-corner-truncated square quartz resonator supported at four nodal points in Lamé mode," 2010 IEEE International Frequency Control Symposium, Newport Beach, CA, pp. 52-55, 2010.

[70] V. M. Mecea, "Is quartz crystal microbalance really a mass sensor?," Sensors and Actuators A: Physical, Volume 128, Issue 2, Pages 270-277, ISSN 0924-4247, 2006.

[71] Hieda, Mitsunori, Garcia, Rafael, Dixon, Matthew, Daniel, Tad, Allara, David, Chan, Ming, "Ultrasensitive quartz crystal microbalance with porous gold electrodes," Applied Physics Letters. 84, 628-630, 2004.

[72] J. Rabe, V. Seidemann and S. Buettgenbach, "Monolithic fabrication of wireless miniaturized quartz crystal microbalance (QCM-R) array for biochemical sensing," Transducers '03. 12th International Conference on Solid-State Sensors, Actuators and Microsystems. Digest of Technical Papers, Boston, MA, USA, pp. 1875-1876 vol.2, 2003.

[73] A. Kakalis and C. Panayiotou, "The temperature effect of AT-cut input quartz parameters on QCM effective properties calculated with equivalent circuit models," Journal of Electroceramics, vol. 40, no. 1, pp. 23–35, Dec. 2017.

[74] X. Wang, B. Ding, J. Yu, M. Wang, and F. Pan, "A highly sensitive humidity sensor based on a nanofibrous membrane coated quartz crystal microbalance," Nanotechnology, vol. 21, no. 5, p. 055502, 2009.

[75] W. Sun, W. Song, X. Guo, and Z. Wang, "Ultrasensitive detection of nucleic acids and proteins using quartz crystal microbalance and surface plasmon resonance sensors based on target-triggering multiple signal amplification strategy," Analytica Chimica Acta, vol. 978, pp. 42–47, 2017.

[76] H. Jin, X. Tao, B. Feng, L. Yu, D. Wang, S. Dong, and J. Luo, "A humidity sensor based on quartz crystal microbalance using graphene oxide as a sensitive layer," Vacuum, vol. 140, pp. 101–105, 2017.

[77] F. Feng, J. Zheng, P. Qin, T. Han, and D. Zhao, "A novel quartz crystal microbalance sensor array based on molecular imprinted polymers for simultaneous detection of clenbuterol and its metabolites," Talanta, vol. 167, pp. 94–102, 2017.

[78] J. Hu, X. Huang, and H. Lin, "Study on QCM Mass Sensitivity for Different Electrode Structures," 2018 IEEE International Conference on Applied Superconductivity and Electromagnetic Devices (ASEMD), 2018.

[79] G. Sauerbrey, "Use of quartz vibrator for weighting thin films on a microbalance," Zeitschrift fur Physik , 155, 206–212, 1959.

[80] R. Zheng, X. Meng, S. Wang, and Y. Lv, "Computation of Equivalent Circuit Parameters of QCM and Evaluation of the Measurement Uncertainties," Proceedings of the 2nd International Conference on Electronic and Mechanical Engineering and Information Technology (2012), 2012.

[81] X. P. Liu and D. M. Zhao, "Study on the Equivalent Circuit of Quartz Crystal Microbalance (QCM) with Material Properties," Applied Mechanics and Materials, vol. 252, pp. 189–192, 2012.

[82] Y. Jiménez, M. Otero, and A. Arnau, "QCM Data Analysis and Interpretation," Piezoelectric Transducers and Applications, pp. 331–398, 2009.

[83] F. Temel and M. Tabakci, "Calix[4]arene coated QCM sensors for detection of VOC emissions: Methylene chloride sensing studies," Talanta, vol. 153, pp. 221–227, 2016.

[84] "A Practical Model of Quartz Crystal Microbalance in Actual Applications," Sensors, vol. 17, no. 8, p. 1785, Mar. 2017./

[85] C. Lu, "Theory and Practice of the Quartz Crystal Microbalance," Methods and Phenomena Applications of Piezoelectric Quartz Crystal Microbalances, pp. 19–61, 1984.

[86] H. Jiang, "Finite element analysis on electrode structure of QCM," 2009 Chinese Control and Decision Conference, 2009.

[87] "Product:MEMS Module," COMSOL. [Online]. Available: https://www.comsol.com/mems-module. [Accessed: 08-Nov-2019].

[88] J. Rabe, V. Seidemann, and S. Buettgenbach, "Monolithic fabrication of wireless miniaturized quartz crystal microbalance (QCM-R) array for biochemical sensing," TRANSDUCERS 03. 12th International Conference on Solid-State Sensors, Actuators and Microsystems. Digest of Technical Papers, 2010.

[89] F. Lu, H. Lee, and S. Lim, "Quartz crystal microbalance with rigid mass partially attached on electrode surfaces," Sensors and Actuators A: Physical, vol. 112, no. 2-3, pp. 203–210, 2004.

[90] I. Efimov, A. R. Hillman, and J. W. Schultze, "Sensitivity variation of the electrochemical quartz crystal microbalance in response to energy trapping," Electrochimica Acta, vol. 51, no. 12, pp. 2572–2577, 2006.

[91] F. Shen, K. Lee, P. Lu, and S. Oshea, "Energy trapping in mesa-shaped quartz crystal microbalance," Proceedings of IEEE Sensors.

[92] L. Yang and X. Huang, "Response of Quartz Crystal Microbalance Loaded with Single-drop Liquid in Gas Phase," The Open Electrical & Electronic Engineering Journal, vol. 8, no. 1, pp. 197–201, 2014.

[93] J. Shi, C. Fan, M. Zhao, J. Yang, "Energy trapping of thickness-shear modes in inverted-mesa AT-cut quartz piezoelectric resonators," Ferroelectrics, 494:1, 157-169, 2016.

[94] J. Hu and X. Huang, "QCM Mass Sensitivity Analysis Based on Finite Element Method," IEEE Transactions on Applied Superconductivity, vol. 29, no. 2, pp. 1–4, 2019.

[95] A. Richardson, V. R. Bhethanabotla, A. L. Smith, and F. Josse, "Patterned electrodes for thickness shear mode quartz resonators to achieve uniform mass sensitivity distribution," 2008 IEEE Sensors, 2008.

[96] L. A. C. Ahumada, N. P. Pérez, O. L. H. Sandoval, F. D. P. Guerrero, and J. J. S. Olmedo, "A new way to find dielectric properties of liquid sample using the quartz crystal resonator (QCR)," Sensors and Actuators A: Physical, vol. 239, pp. 153–160, 2016.

[97] X.-H. Huang, W. Pan, J.-G. Hu, and Q.-S. Bai, "The Exploration and Confirmation of the Maximum Mass Sensitivity of Quartz Crystal Microbalance," IEEE Transactions on Ultrasonics, Ferroelectrics, and Frequency Control, vol. 65, no. 10, pp. 1888–1892, 2018.

[98] T. Abe and M. Higuchi, "A Monolithic QCM Array Designed for Mounting on a Flow Cell," IEEE Sensors Journal, vol. 11, no. 1, pp. 86–90, 2011.

[99] A. A. Zainuddin et al., "Design and optimization of a MEMS quartz mass sensor array for biosensing," IEEE 4th International Conference on Smart Instrumentation, Measurement and Application (ICSIMA), pp. 1-5, Putrajaya, 2017.

[100] J. Rabe, S. Buttgenbach, J. Schroder, and P. Hauptmann, "Monolithic miniaturized quartz microbalance array and its application to chemical sensor systems for liquids," IEEE Sensors Journal, vol. 3, no. 4, pp. 361–368, 2003.

[101] T. Abe, V. Hung, and M. Esashi, "Inverted mesa-type quartz crystal resonators fabricated by deep-reactive ion etching," IEEE Transactions on Ultrasonics, Ferroelectrics and Frequency Control, vol. 53, no. 7, pp. 1234–1236, 2006.

[102] J. Zhang, J. Liang, and T. Ueda, "Design and evaluation of a dual channel high frequency Quartz crystal Microbalance," 2016 10th International Conference on Sensing Technology (ICST), 2016.

[103] F. Liu, F. Li, A. Nordin, and I. Voiculescu, "A Novel Cell-Based Hybrid Acoustic Wave Biosensor with Impedimetric Sensing Capabilities," Sensors, vol. 13, no. 3, pp. 3039–3055, Apr. 2013.

[104] P. Wang, J. Su, W. Dai, G. Cernigliaro, and H. Sun, "Ultrasensitive quartz crystal microbalance enabled by micropillar structure," Applied Physics Letters, vol. 104, no. 4, p. 043504, 2014.

[105] T. Abe and M. Esashi, "One-chip multichannel quartz crystal microbalance (QCM) fabricated by Deep RIE," Sensors and Actuators A: Physical, vol. 82, no. 1-3, pp. 139–143, 2000.

[106] L. Li, M. Esashi, and T. Abe, "A miniaturized biconvex quartz-crystal microbalance with large-radius spherical thickness distribution," Applied Physics Letters, vol. 85, no. 13, pp. 2652–2654, 2004.

[107] J. Liang, J. Zhang, W. Zhou, and T. Ueda, "Development of a Flow Injection Based High Frequency Dual Channel Quartz Crystal Microbalance," Sensors, vol. 17, no. 5, p. 1136, 2017.

[108] K. Jaruwongrungsee, T. Maturos, K. Wong-Ek, M. Sangworasil, C. Pintavirooj, A. Wisitsora-At, and A. Tuantranont, "Fabrication of QCM sensor array and PDMS micro chamber for biosensor applications," 2009 6th International Conference on Electrical Engineering/Electronics, Computer, Telecommunications and Information Technology, 2009.

APPENDIX A

PERMISSION FOR USING PUBLICATIONS

University
of Windsor

Aashish Joseph <josep11t@uwindsor.ca>

Fwd: Copyright permission
1 message

M.E. Brennan <me.brennan@ieee.org>   Wed, Nov 13, 2019 at 10:08 AM
To: josep11t@uwindsor.ca
Cc: M E Brennan <me.brennan@ieee.org>

Dear Aashish Joseph,

Your request has been forwarded to me for response. The IEEE does not require individuals working on a dissertation/thesis to obtain a formal reuse license however, you must follow the requirements listed below:

Textual Material

Using short quotes or referring to the work within these papers) users must give full credit to the original source (author, paper, publication) followed by the IEEE copyright line © [Year of publication] IEEE.

In the case of illustrations or tabular material, we require that the copyright line © [Year of original publication] IEEE appear prominently with each reprinted figure and/or table.

If a substantial portion of the original paper is to be used, and if you are not the senior author, also obtain the senior author's approval.

Full-Text Article

If you are using the entire IEEE copyright owned article, the following IEEE copyright/ credit notice should be placed prominently in the references: © [year of original publication] IEEE. Reprinted, with permission, from [author names, paper title, IEEE publication title, and month/year of publication]

Only the accepted version of an IEEE copyrighted paper can be used when posting the paper or your thesis on-line. You may not use the final published version

In placing the thesis on the author's university website, please display the following message in a prominent place on the website: In reference to IEEE copyrighted material which is used with permission in this thesis, the IEEE does not endorse any of [university/educational entity's name goes here]'s products or services. Internal or personal use of this material is permitted. If interested in reprinting/republishing IEEE copyrighted material for advertising or promotional purposes or for creating new collective works for resale or redistribution, please go to

http://www.ieee.org/publications_standards/publications/rights/rights_link.html

to learn how to obtain a License from RightsLink.

If applicable, University Microfilms and/or ProQuest Library, or the Archives of Canada may supply single copies of the dissertation.

Kind regards,
M.E. Brennan

Ms M.E. Brennan
IEEE
501 Hoes Lane
Piscataway, NJ 08854-4141 USA
me.brennan@ieee.org

+1 (732) 562-2660

University
of Windsor

Aashish Joseph <josep11t@uwindsor.ca>

Copyright Permission

2 messages

Aashish Joseph <josep11t@uwindsor.ca>   Wed, Nov 13, 2019 at 11:27 AM
To: annie.xie@mdpi.com

Dear Annie,

I would like to use the following published paper in my thesis and I need MDPI Sensors Copyright permission. Please let me know the procedure to obtain the permission.

Paper -"Advanced Micro-and Nano-Gas Sensor Technology: A Review"
Authors - Haleh Nazemi, **Aashish Joseph**, Jaewoo Park and Arezoo Emadi

Thank you,

Regards,
Aashish Joseph.

Research Assistant,
University of Windsor, Canada.
Phone - 5199911350.

Annie Xie <annie.xie@mdpi.com>   Wed, Nov 13, 2019 at 11:13 PM
Reply-To: annie.xie@mdpi.com
To: Aashish Joseph <josep11t@uwindsor.ca>
Cc: nazemih@uwindsor.ca, Sensors Editorial Office <sensors@mdpi.com>

Dear Mr. Joseph,

As I have replied to Mr. Nazemi.

Sensors is an open access journal. The authors themselves contains all copyright of paper published on Sensors. Thus no permission from us is needed for reusing materials from this paper "Advanced Micro-and Nano-Gas Sensor Technology: A Review".

Hope this could help.

Kind regards,

Ms. Annie Xie
Assistant Editor
E-Mail: annie.xie@mdpi.com

VITA AUCTORIS

NAME:	Aashish Joseph
PLACE OF BIRTH:	Tamil Nadu, India.
YEAR OF BIRTH:	1995
EDUCATION:	Kumaraguru College of Technology, B.Eng., Coimbatore, Tamil Nadu, India. 2017
	University of Windsor, M.A.Sc., Windsor, ON, Canada. 2019